Doc No: PO-TR-RAL-AT-0024
Issue: 1
Date: 26 May 1999

AATSR Infra-Red Radiometric Calibration Report

Prepared by: **D.L. Smith**

Checked by: **J. Delderfield**

Approved by: **T. Edwards**

Contents

1 Acronyms

ATSR	Along Track Scanning Radiometer
AATSR	Advanced Along Track Scanning Radiometer
ACTS	AATSR Calibration and Test System
BOL	Beginning of Life
CATSA	Calibration and Thermal Simulation Assembly
DEU	Digital Electronics Unit
EOL	End of Life
FPA	Focal Plane Assembly
FOV	Field of View
IEU	Instrument Electronics Unit
IFOV	Instantaneous Field of View
IVR	Infrared and Visible Radiometer
MDA	Measurement Data Adapter
RIRT	Rhodium Iron Resistance Thermometer
SMU	Scan Mechanism Unit
STC	Space Test Chamber
TCADS	Tank Control and Data System

1 Applicable Documents

AD 1	PO-RS-GAD-AT-0002	AATSR Instrument Performance Requirements - Issue 2
AD 2	PO-PL-RAL-AT-0014	AATSR Test and Calibration Plan - Issue 2
AD 3	PO-PR-RAL-AT-0027	AATSR Radiometric Checkout and Stray Light Test – Issue 1
AD 4	PO-PR-RAL-AT-0028	AATSR Radiometric Calibration Procedures – Issue 1
AD 5	PO-SW-BAE-AT-0002	Statement of Work for AATSR VISCAL and Cooler Subsystem, Instrument Calibration, Australian Shadowing and System Consultancy - Issue 1
AD 6	PO-PL-MMB-AT-0016	AATSR EM & FM Thermal Test Plan
AD 7	PO-NC-MMB-AT-0137	IR Channel Signal Noise MRB
AD 8	Mason, G. (1991)	'Test and calibration of the Along Track Scanning Radiometer, a satellite-borne infrared radiometer designed to measure sea surface temperature.' D.Phil. Thesis, University of Oxford.
AD 9	ER-RP-OXF-AT-2001	ATSR-2 Test and Calibration Report
AD 10	PO-TN-RAL-AT-0190	Calibration of External Blackbody Rhodium Iron Resistance Thermometers
AD 11	ER-TN-MSL-AT-2011	Blackbody Subsystem configuration and calibration coefficients – Issue 4
AD 12	PO-TR-MSL-AT-0002	Emissivity measurements on AATSR FM blackbodies.

2 Scope of Document

This document describes the AATSR infrared radiometric calibration defined in the calibration plan, AD 2, as required by AD 1. This fulfils the tasks defined in section 8.1.2 of RAL's statement of work, AD 5.

3 Test Requirements

The main purpose of the pre-launch radiometric calibration is to verify that AATSR meets the performance requirements specified in AD 1. As an absolute minimum performance, AATSR should be able to measure brightness temperatures to an accuracy of ±0.1K between 265 K and 310 K [R02/079]. The radiometric noise at 270 K must be less than 0.08K, 0.05K and 0.05K for 3.7µm, 11µm and 12µm channels [R01/32 in AD 1]. For a constant scene, there must be no specific signal present on the signal channel outputs [R02/059]. The requirements for the pre-launch radiometric calibration of AATSR, defined in the AATSR test and calibration plan AD 2, are:

- Verify the 'on-board' radiometric calibration for a range of target temperatures between 210K and 310 K.
- Measure any detector non-linearity and make appropriate corrections.
- Verify that the different channels produce self-consistent results.
- Measure the radiometric noise.
- Measure the effect on the radiometric calibration with the detectors operating at an increased temperature.
- Verify the calibration with the on-board blackbodies set at different power levels.
- Investigate the radiometric performance under different thermal conditions.
- Determine and measure any scan dependent variation in the radiometric performance.
- Determine and measure radiometric leaks.
- Verify the calibration under simulated orbital transient thermal conditions.

4 Calibration Algorithms

The calibration algorithms for the infrared channels are identical to those used for ATSR-1 and 2 (AD 8 and AD 9). They have been reproduced here for completeness.

The photon flux, Φ_λ, incident on an AATSR detector with peak response at wavelength λ, from a scene brightness temperature T_{scene} is given by

$$\begin{aligned}\Phi_\lambda = \tau_{FPA,\lambda}\ \xi_\lambda\ A\Omega\Big[r_{Rh,\lambda}^2 \int R_\lambda(\lambda)L(\lambda,T_{scene})d\lambda \\ + \left(1-r_{Rh,\lambda}\right)r_{Rh,\lambda}\int R_\lambda(\lambda)L(\lambda,T_{scan})d\lambda \\ + \left(1-r_{Rh,\lambda}\right)\int R_\lambda(\lambda)L(\lambda,T_{parab})d\lambda\Big] \\ + \tau_{FPA,\lambda}(1-\xi_\lambda)A\Omega\int R_\lambda(\lambda)L(\lambda,T_{surr})d\lambda \\ + \pi\, l^2\int R_\lambda(\lambda)L(\lambda,T_{FPA})d\lambda,\end{aligned} \qquad 4.1$$

where $L(\lambda,T) = 2hc^2/\left(\exp\left(hc/k_b T\right)-1\right)$, is the spectral radiance at wavelength λ emitted by a black-body at temperature T, per unit area, per steradian, per second, per unit wavelength, where

h is Plank's constant = 6.6260755x10^{-34} Js,

c is the velocity of light = 299792458 ms^{-1},

k_b is Boltzmann's constant = 1.380658x10^{-23} JK^{-1},

$R_\lambda(\lambda)$ is the measured spectral response of each channel as a function of wavelength,

$\tau_{FPA,\lambda}$ is the transmission of the FPA at the wavelength of peak response for each spectral channel,

$A\ \Omega$ is the total instrument throughput for radiation falling onto the detectors for each spectral channel = 1.5742x10^{-4} cm^{2}sr,

ξ_λ is the fraction of the total throughput from the scene radiation (see AD 8).

$r_{Rh,\lambda}$ is the reflectivity of the rhodium coating of the instrument fore optics

T_{scan} is the temperature of the scan mirror,

T_{parab} is the temperature of the paraboloid mirror,

T_{surr} is the temperature of the paraboloid surround (assumed to be the same as the temperature of the FPA baffle and to have an emissivity of 1.0),

T_{FPA} is the temperature of the FPA,

l is the size of the (square) detectors.

Since the detectors are cooled to ~ 80K, the contribution from the cold FPA to the total signal is negligible. Assuming that $T_{scan} = T_{parab} = T_{surr} = T_{inst}$, where T_{inst} is the temperature of the instrument fore-optics, equation 5.1 reduces to

$$\Phi_\lambda = \tau_{FPA,\lambda,}A\Omega\Big[r_{Rh,\lambda}^2\xi_\lambda\int R_\lambda(\lambda)L\left(\lambda,T_{scene}\right)d\lambda + (1-{}^{2}_{Rh,\lambda}\ \xi_\lambda)\int R_\lambda(\lambda)L\left(\lambda,T_{INST}\right)d\lambda\Big] \qquad 4.2$$

$$= \Phi_{scene,\lambda} + \Phi_{inst,\lambda} \qquad 4.3$$

where $\Phi_{scene,\lambda}$ is the scene signal in each channel,
$\Phi_{inst,\lambda}$ is the signal in each channel from the instrument fore-optics.

The signal measured by each channel is converted to a voltage and then digitised to counts, C_λ (in the range 0 to 4095) such that

$$C_\lambda = A_{g,\lambda}\left(\Phi_{scene,\lambda} + \Phi_{inst,\lambda}\right) + V_{off,\lambda} \qquad 4.4$$

where $A_{g,\lambda}$ is the gain of the detectors / electronics in each channel and $V_{off,\lambda}$ is the voltage offset in the detectors / electronics. If $\Phi_{inst,\lambda}$ remains constant around the scan then the signal from each channel may be expressed as

$$\boxed{\Phi_\lambda = A_{0,\lambda} + A_{1,\lambda} C_\lambda} \qquad 4.5$$

where $A_{0,\lambda}$ and $A_{1,\lambda}$ are constants provided there is no drift in the response of the detector electronics (or change in the fore-optics temperature in the case of $A_{0,\lambda}$). With the two on-board blackbodies at temperatures T_1 and T_2 producing radiances $\Phi_{1,\lambda}$ and $\Phi_{2,\lambda}$ hence counts $C_{1,\lambda}$ and $C_{2,\lambda}$, the coefficients can be calculated using

$$A_{1,\lambda} = \frac{(\Phi_{1,\lambda} - \Phi_{2,\lambda})}{(C_{1,\lambda} - C_{2,\lambda})} \qquad 4.6$$

and

$$A_{0,\lambda} = \frac{(C_{2,\lambda}\Phi_{1,\lambda} - C_{1,\lambda}\Phi_{2,\lambda})}{(C_{1,\lambda} - C_{2,\lambda})} \qquad 4.7$$

The signals from the on-board targets are given by

$$\boxed{\Phi_{i,\lambda} = \varepsilon_{i,\lambda}\int_\lambda R_\lambda(\lambda) L(\lambda, T_i) d\lambda + (1 - \varepsilon_{i,\lambda})\int_\lambda R_\lambda(\lambda) L(\lambda, T_{inst}) d\lambda} \qquad 4.8$$

where $\varepsilon_{i,\lambda}$ is the emissivity of the black-body.

In practice, a lookup table is used for the conversion from temperature to radiance and vice versa (see Appendix C).

After calculating the coefficients, $A_{0,\lambda}$ and $A_{1,\lambda}$, the average pixel counts for an external black-body temperature are converted to a radiance, Φ_λ. This will contain a background term such that the radiance from an external black-body, $\Phi_{bb,\lambda}$, is given by

$$\boxed{\Phi_{bb,\lambda}(T_{bb}) = \frac{\Phi_\lambda - (1 - \varepsilon_{bb,\lambda})\Phi_\lambda(T_{back})}{\varepsilon_{bb,\lambda}}} \qquad 4.9$$

where $\varepsilon_{bb,\lambda}$ is the emissivity of the external black-body and T_{bb} is its temperature. T_{back} is the background temperature taken as a weighted average of the earth shine plate and the instrument fore optics enclosure temperatures (the weighting factors will be determined

from a thermal mathematical model). After calculating the radiance, the brightness temperature may be obtained using the radiance/ temperature look-up-tables.

The instrument noise is expressed as the noise equivalent brightness temperature difference, NEΔT, and is given by

$$NE\Delta T_\lambda = A_{1,\lambda}\,\Delta C_\lambda \left(\left. \frac{\partial \Phi_\lambda}{\partial T} \right|_T \right)^{-1} \qquad 4.10$$

where ΔC_λ is the signal channel noise taken to be the standard deviation of the blackbody pixel counts.

Because of slight differences between the two signal integrators on each channel, the brightness temperatures and noise for odd and even pixels are calculated separately. Thus the overall noise and NEΔT in each channel will be

$$\Delta C_\lambda = \sqrt{\frac{1}{2}\left((\Delta C_\lambda)^2_{odd} + (\Delta C_\lambda)^2_{even} \right)} \qquad 4.11$$

and

$$NE\Delta T_\lambda = \sqrt{\frac{1}{2}\left(NE\Delta T^2_{odd} + NE\Delta T^2_{even} \right)}. \qquad 4.12$$

5 Test Equipment

5.1 Thermal Environment

The infrared radiometric calibration was performed in the Space Test Chamber (STC) at RAL, Figure 5.1. This is a 3m diameter, 5.5m long vacuum chamber situated in a class 10000 clean room, with class 100 enclosures around the entrances to the chamber. Two rails inside the chamber supported the CATSA, which in turn supported the AATSR instrument and the calibration targets. Within the chamber, the AATSR instrument was surrounded by temperature controlled panels to simulate the expected orbital thermal environment.

An earth-shine-plate (ESP) was used to simulate the radiation from the Earth. The temperature of the ESP was controlled by passing a cooled refrigerant (Galden 70) through pipes attached to its reverse. The refrigerant temperature was controlled by a Huber U390 refrigerator. The surface of the ESP facing the instrument was painted with Chemglaze Z306 black paint, having an emissivity of ~0.95. The calibration blackbodies were positioned on the instrument's scan cone behind two elliptical apertures in the plate. A drum baffle at the same temperature of the ESP was used to minimise the temperature gradients across the plate. In addition, the two ends of the chamber were thermally isolated by means of an MLI curtain.

The ESP and blackbody targets were supported on a 1.6m diameter wheel machined from aluminium alloy. The structure could be rotated about the axis of the instrument's scan cone to allow the calibration measurements to be made at all positions in the nadir and along-track view. The rotation was controlled by means of a 216 tooth, 1296mm pitch ring gear. This was driven by a smaller 20 tooth, 120mm pitch spur gear, which in turn was driven by a McLennan STD835 250-75 stepper motor (400 steps per revolution) with a 87:1 gearbox. This gave 1044 stepper motor steps to 1^{o} of ESP rotation. The ACTS was used to drive the motor and log the ESP position via a McLennan TM164C stepper motor drive.

A cooled shroud simulated the instrument's view to space. This was separated into 12 zones independently controlled by the TCADS with a combination of resistive heaters and LN_2 cooling. For AATSR, only the 5 zones having a direct view of the IVR were used.

A platform simulator (PSM) represented the interface with the spacecraft. This was an aluminium honeycomb panel with a carbon fibre/epoxy skin. Aluminium inserts were used to attach the instrument to the panel. The temperature at this interface was controlled by a cooled fluid loop beneath the panel, attached to these inserts via flexible copper braids. The fluid temperature was controlled by a Huber CC40 refrigerator.

Although the CATSA structure was designed so that the effect of temperature gradients were small, further precautions were taken by insulating the 'cold' end with an MLI blanket and using heaters to maintain a constant, uniform temperature (~20^{o}C). This was done to minimise any mechanical distortions that may arise from large temperature gradients.

The temperatures of the thermal panels were measured by 180 100Ω PRTs. The temperature of the instrument was monitored by 51 Type-T thermocouples attached by MMS for the thermal tests. These were in addition to the flight temperature sensors. The facility PRTs and test thermocouples were logged by the TCADS.

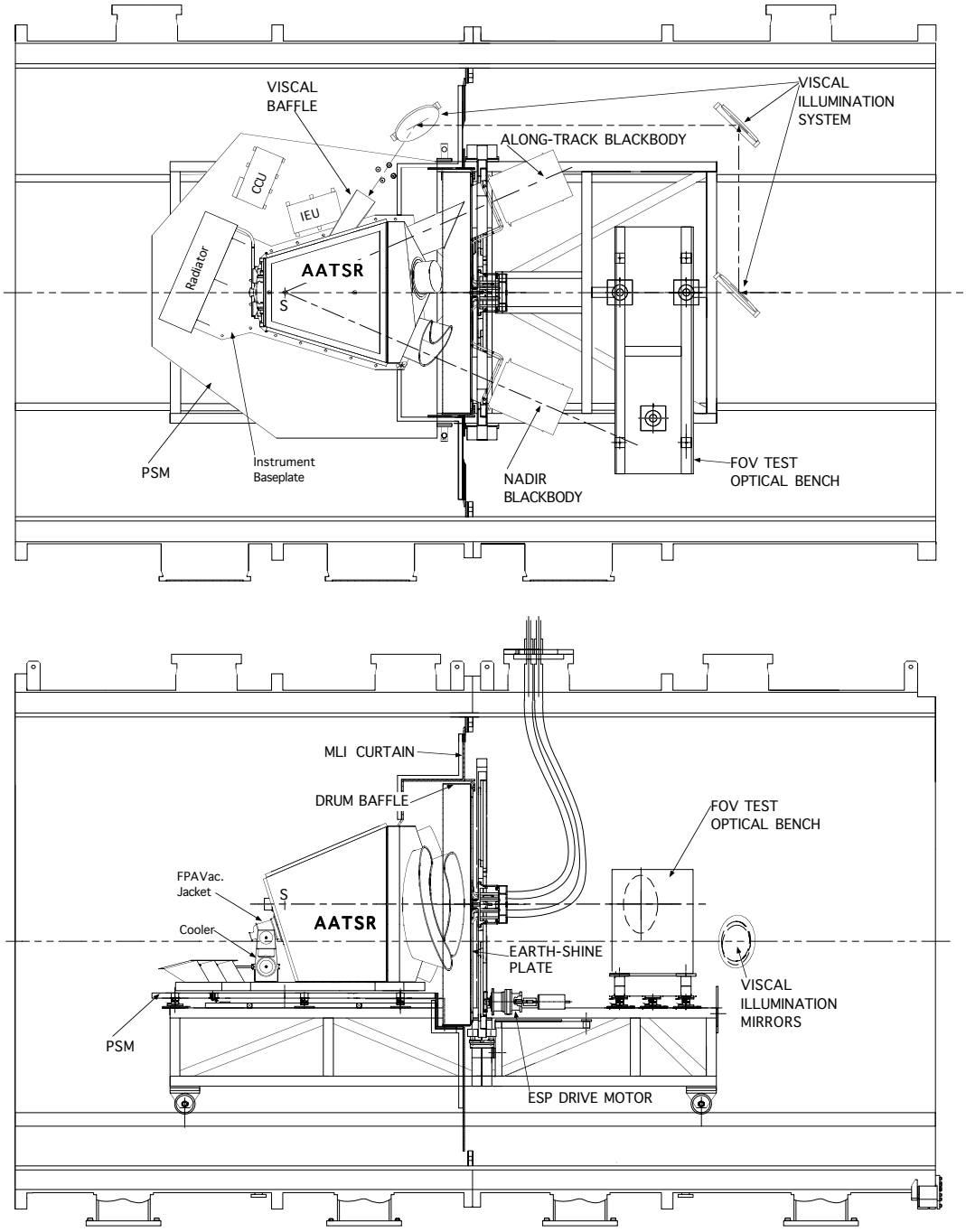

Figure 5.1: Layout of AATSR calibration equipment in the RAL Space Test Chamber.

5.2 Black-Body Targets

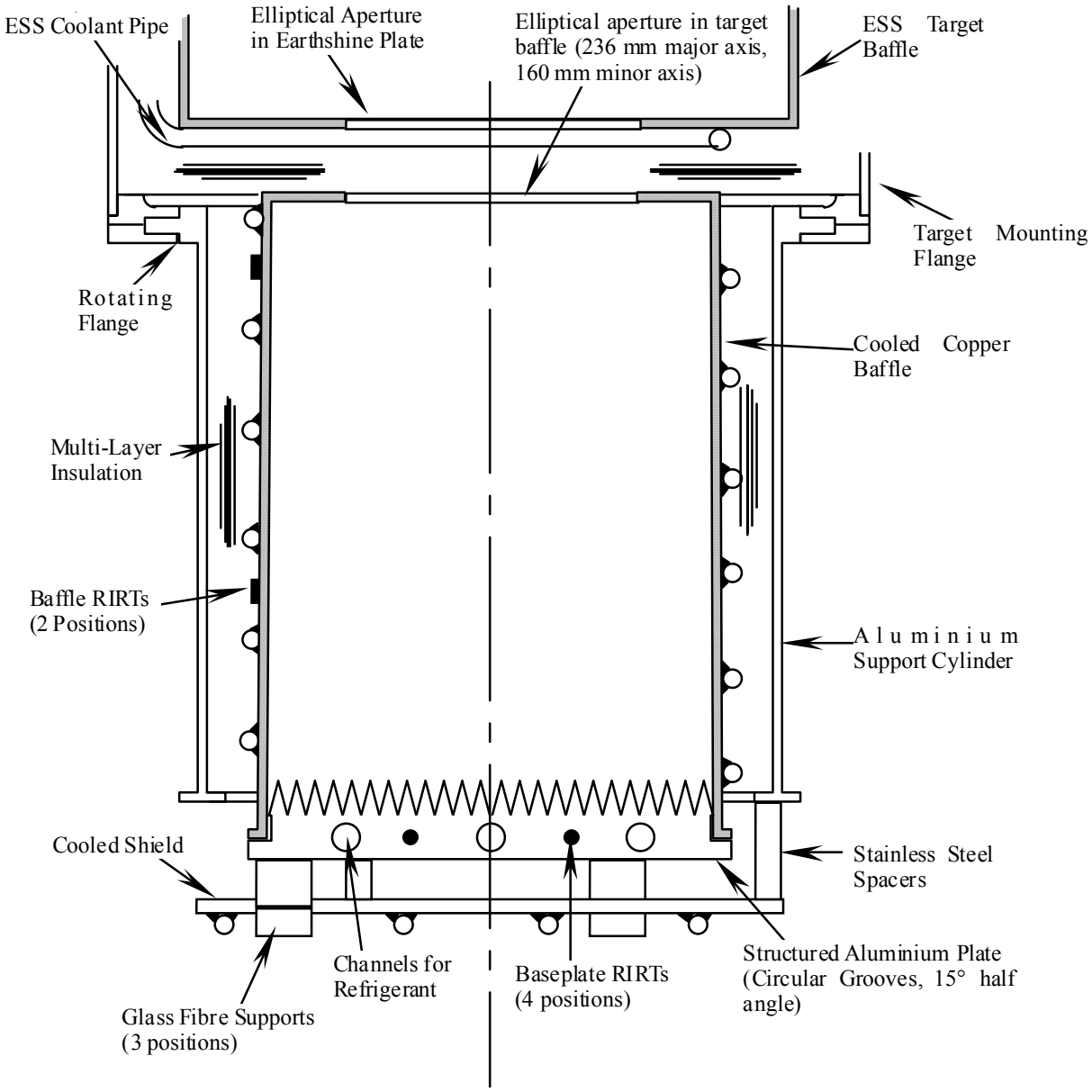

The two blackbody targets for the radiometric calibration were those used for the ATSR & ATSR-2 calibrations at Oxford University. These were designed and built by the U.K. Meteorological Office to provide a scene radiance corresponding to an accurately known temperature. For AATSR to meet its scientific objectives, the on-board calibration must be better that ±0.1K. To ensure that the calibration was verified to at least this level, the external targets had to meet the following requirements:

1) The temperature gradients across the target are less than 0.02 K
2) The temperature fluctuations over 5 minutes must be less than 0.02 K
3) The temperature of the target must be known to better than 0.02 K
4) The errors caused by the emissivity not being unity must be less than 0.035 K.
5) The target aperture must completely overfill the AATSR scan beam.

The targets consisted of 350mm high copper cylinders with a 250mm diameter, structured aluminium alloy base and an elliptical entrance baffle plate (236mm major axis and 160 mm minor axis). The baffles were slightly tapered having a diameter of 252 mm at the base and 240 mm at the entrance plate. The inside face of the base plates were machined with circularly symmetric groves (10mm wide, 15° half angle). All of the inside surfaces of the targets were coated with Nextel 101 - C10 black paint. The target temperatures were controlled by circulating a refrigerant through the structured base plate and around the baffles. The along-track target had a second fluid loop around the baffle to allow it to be cooled to lower temperatures using liquid nitrogen. The targets were insulated with MLI and supported by aluminium cans.

The emissivities of the target were calculated by Graeme Mason from the geometry of the target and the spectral emissivity of the paint, Table 5-1. An estimation of the target emissivities was obtained from the ATSR-2 test data and presented alongside the calculated values. The estimated values agree with the calculated emissivities within the allowed error budget and show that the black-paint had not suffered any deterioration between the manufacture of the targets and ATSR-2 testing.

	Emissivities	
	Calculated	Estimated
3.7 μm	0.99899 ± 0.00035	0.99911 ± 0.00055
11 μm	0.99847 ± 0.00036	0.99870 ± 0.00040
12 μm	0.99871 ± 0.00037	0.99871 ± 0.00032

Table 5-1: Calculated and estimated emissivities of external blackbodies.

The largest temperature error resulting from the uncertainty in the emissivity will be when T_{BB} = 320 K and T_{back} = 250 K. Using the calculated emmisivities in Table 5-1 gives the values in

Table 5-2

	ΔT
3.7 μm	10mK
11 μm	19mK
12 μm	21mK

Table 5-2: Worst case brightness temperature error due to uncertainty in emissivity.

The temperatures of each target were measured by six rhodium-iron resistance thermometers (RIRTs) supplied by Oxford Instruments. These sensors were accurate to ± 0.01 K and had self-heating of less than 0.001K. They were recalibrated against standards traceable to ITS90 by Oxford Instruments in July 1997 before the arrival of AATSR at RAL (AD 10).

The resistances of the RIRTs were measured by a 'Tinsley Consort' AC resistance bridge having an accuracy of ±10 ppm. The calibration of the bridge was compared against a Wilkins 25Ω standard resistor.

Two Huber closed cycle bath refrigerators were used to control the refrigerant temperature. A CC-90 unit having 600W cooling power at 200K and ±0.1K stability was used to control the nadir view target, and an HS-80 unit with 250W cooling at 200K and ±0.05K stability was used for the forward view target. The CC-90 was the more modern unit having a digital control unit. Initially, this unit was unable to maintain the blackbody to required level of stability of 0.02K over five minutes. This was improved by updating the control software with a later version supplied by Huber, to allow the control constants to be adjusted.

6 Experimental

The radiometric calibration was performed by measuring the radiometric response of the infrared channels over a range of external target temperatures. In practice, only one of the targets was changed during a calibration run (usually nadir) while the other (along-track target) was maintained at a fixed temperature for reference. For the initial calibration at the centre of nadir view (RAD03), the nadir target was set at 5K intervals between 210K to 315K. The rest of the calibration tests were performed with a reduced set of target temperatures at 10K intervals between 240K to 310K. Measurements were also taken at approximately the same temperature of the on-board targets. The fixed target was usually set to 280K, being approximately mid-way between the two on-board targets. Data were recorded only when all four of the base plate RIRTs had been stable to within 20mK over the previous five minutes, with temperature gradients across the base plate of less than 20mK. The ACTS software tracked these criteria and indicated if the sensors were meeting the steady state condition.

Each test was executed with the AATSR IVR and environment under thermal equilibrium. The temperatures of the thermal panels for each test case (see Table 6-1) were defined by MMS in the thermal test plan, AD 6.

Test No.	Condition	Shroud	ESP	PSM
RAD01-10, 12,15-17	BOL	-62.0°C	-17.0°C	-12.0°C
RAD11	EOL	-58.0°C	+12.0°C	+14.0°C
RAD13	BOL + Warm Shrouds	-50.0°C	-17.0°C	-12.0°C
RAD14	BOL + Warm ESP	-62.0°C	-3.0°C	-12.0°C

Table 6-1: Temperatures of thermal panels during radiometric calibration.

Science data packets from the DEU were acquired by the Measurement Data Adapter (MDA) of the EGSE. These were merged with the contemporaneous blackbody and thermal environment data recorded by the ACTS and TCADS. When the steady state criteria for a calibration measurement was met, the routine GET_IR was run to acquire 10 contiguous packets from the measurement data stream. After an initial check for missing or duplicate packets, CRC errors, scan mirror jitters, packet write errors and instrument telemetry out of limits, the data were processed to give the following parameters

- Average on-board and blackbody temperatures
- Standard deviation of blackbody temperatures
- Average on-board and external blackbody pixel counts (12μm, 11μm, 3.7μm)
- Standard deviation of pixel counts (12μm, 11μm, 3.7μm)
- Number of samples for each average.
- Paraboloid-stop temperatures
- Detector temperatures
- Average temperatures for each thermal zone
- Instrument time stamp
- EGSE time stamp
- ACTS time stamp

A further check was then made to see if the pixel noise in each channel was less than 10 counts. If the noise was greater than this then it was an indication of SMU jitters, or excessive breakthrough of vibration induced noise. If the data had passed all the checks, the above parameters were written to a text output file. This was appended to each time the routine was run (the output file name included the test number and date of the test). A new output file was created for each test. The raw data were also saved to a separate binary file for reprocessing where necessary.

At the end of each test, the data in the output files were processed using the algorithms described in §4 to produce brightness temperatures, NEΔTs and radiances for each channel.

To measure any scan-dependent variations, the calibration was verified at $\pm 46^o$, $\pm 40^o$, $\pm 33^o$, $\pm 29^o$, $\pm 22.5^o$, $\pm 15^o$, $\pm 7.5^o$ and 0^o to cover all nadir pixels, and $\pm 29^o$, $\pm 22.5^o$, $\pm 15^o$, $\pm 7^o$ and 0^o to cover all along-track pixels.

Any out-of-field radiometric strays were investigated by holding both targets at a constant temperature of 240K and taking measurements while cycling the earth shine plate about the BOL temperature. This was repeated at the centres and the edges of both swaths.

The orbital simulations were performed with the nadir target at 240K, 275K and 310K for two orbits each, and the along-track target at 280K for all orbits.

The low radiance measurements were performed by cooling the along-track target with liquid nitrogen. When the target temperature had reached 96K, the LN_2 supply was disconnected and the blackbody was allowed to warm up slowly, and measurements taken at 1K intervals. Before this data could be used, a correction to the base-plate temperature was required. This was because of the time delay between the RIRT resistance measurements and the actual time when the science data were recorded, during which time the temperature had increased by as much as 0.4K. This was not so essential at the lowest temperatures when the target was stable and the radiance errors are small in relation to the temperature variations. To do this the individual base-plate temperatures were plotted against the true measurement time given by the ACTS. Figure 6.1 shows a 30-minute extract from this. A smooth line was fitted through the data to produce a look-up table of temperature vs. time. This was then used to derive the true target temperature at the time when science data were recorded.

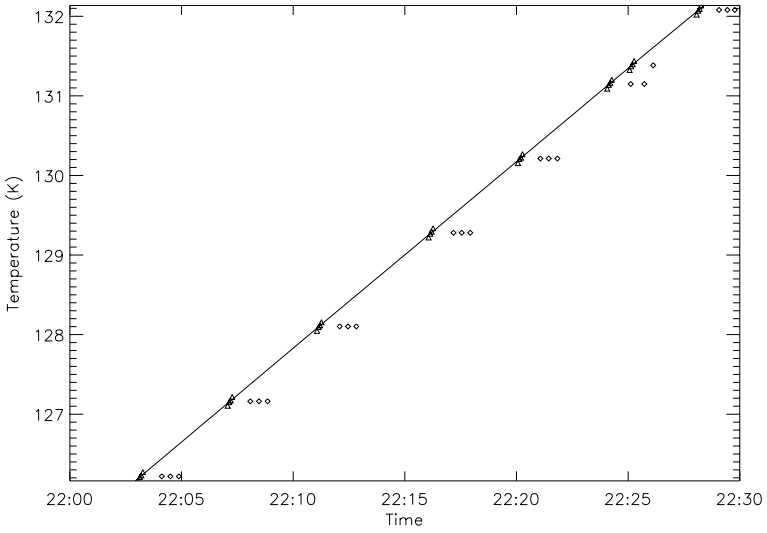

Figure 6.1: Blackbody temperatures vs. time during low-radiance calibration. The RIRT temperatures at the actual measurement time are shown as Δ. The average base-plate temperatures recorded at the time when science data were recorded for calibration are ◇.

7 Results and Analysis

7.1 Radiometric Checkout

Before starting the calibration in earnest, it was necessary to optimise the pixel-map, measure the uniformity of the blackbodies, and ensure that external calibration targets were aligned with the instrument.

7.1.1 Pixel Map

The pixel map on AATSR defines which of the 2000 pixels in the scan will be transmitted in the measurement data packets. The default map consists of 16 VISCAL pixels, 555 nadir swath pixels, 16 +XBB pixels, 371 along-track swath pixels, and 16 –XBB pixels, Figure 7.1. The number and position of the pixels can be modified by macrocommand, provided the total number of pixels in each packet is 974, and there are five views each separated by at least one pixel. Unlike ATSR-2 the pixel map is not used to define the content of each transmitted pixel since, for AATSR, all the channels are telemeterd at full 12 bit digitisation. The design of the fore-optics enclosure should ensure that there is sufficient clearance to enable the detectors to view each swath for the required number of pixels, without any obstruction from the baffles.

To locate the actual edges of each swath, the external targets were first set to 280K to ensure good radiometric contrast with the instrument. With the ESS at the home position, the centres of the nadir and along-track blackbodies were located at pixels 501±1 and 1496±1 respectively, Figure 7.1. The central plateaux correspond to those pixels for which the detectors have a clear view of the target base-plates. Then, starting with the nadir view, the ESS was rotated until one of the targets was partially obscured by the instrument baffle. The pixel map was adjusted to extend the swath by a further ±100 pixels so that the instrument baffles were clearly in view. The edge of the swath was defined by the position of the last pixel where the instrument had a clear view to the external target. The process was repeated for both sides of each entrance baffle and the on-board blackbodies. The VISCAL pixels were located during the visible calibration. The results in Table 7-1 show that there are at least two clear pixels at each end of the nadir and along track views and the on-board targets cover the required range of 16 pixels. Because there was sufficient clearance for each view, it was decided to use the nominal pixel map for the calibration.

	Range of Good Pixels	**Used Pixels**
VISCAL	75-90	75-90
Nadir Swath	219-780	224-778
+XBB	1066-1096	1074-1089
Along-Track Swath	1311-1690	1316-1686
-XBB	1902-1935	1913-1928

Table 7-1: Range of pixels giving a clear view through the entrance baffles, or on-board calibration targets. The used pixels are those selected in the AATSR nominal pixel map.

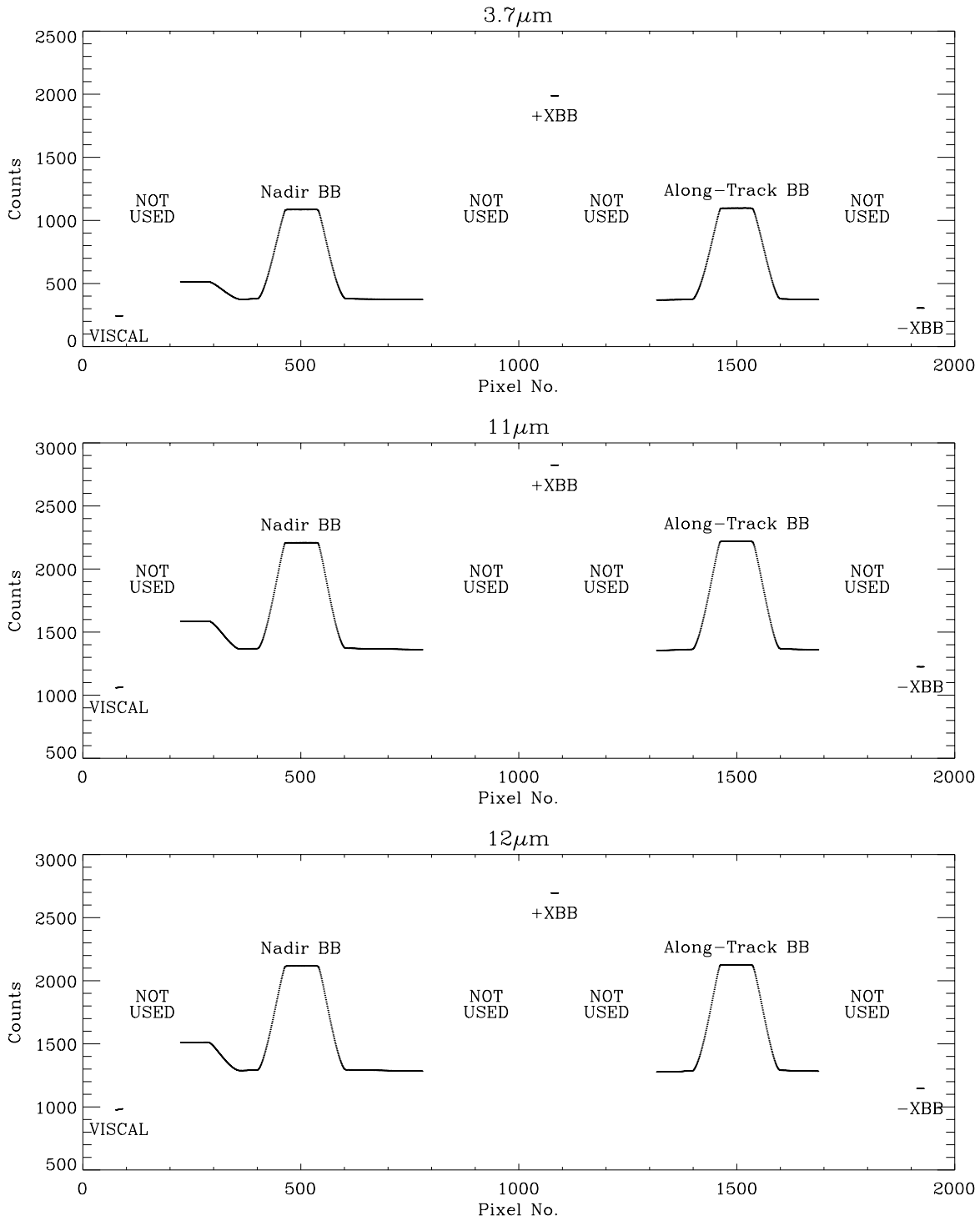

Figure 7.1: Pixel counts for 3.7µm, 11µm and 12µm channels showing from left to right the positions of the VISCAL, nadir swath, +XBB, along-track swath and –XBB. The nadir and along-track targets are at 280K and the ESS at 256 K. The plateau at the start of the nadir swath is the FOV aperture door, which is at a higher temperature to the ESP.

7.1.2 Blackbody alignment and uniformity

The calibration facility had been designed and set up so that when the instrument was mounted on the PSM, the external targets were correctly aligned to the scan cone. Once mounted there was no way of adjusting the alignment. It was therefore necessary to perform a series of measurements to provide a measure of confidence that the external blackbodies were aligned correctly with the instrument. If the alignment was good then the instrument should be able to get a clear view of the external target base-plates at all points around the scan cone. Any misalignment would mean that the view of the blackbodies would include a component from the ESP. This would mean that the measured radiance from the blackbody would have a significant component from the ESP. To investigate this the external targets were maintained at a fixed temperature and the ESP temperature was cycled by ±5°C. Ideally the range should have been ±10°C but the ESP did not respond to the change of fluid temperature as expected (see §7.8). If the targets were well aligned then there should be no variation in the measured brightness temperatures. The results with both external targets at 240K and the ESP at the home position, Figure 7.2 show no trace of any variations. The same result was also found for each end of the nadir and along-track swaths. This was a good indication that the ESP and blackbodies were well aligned.

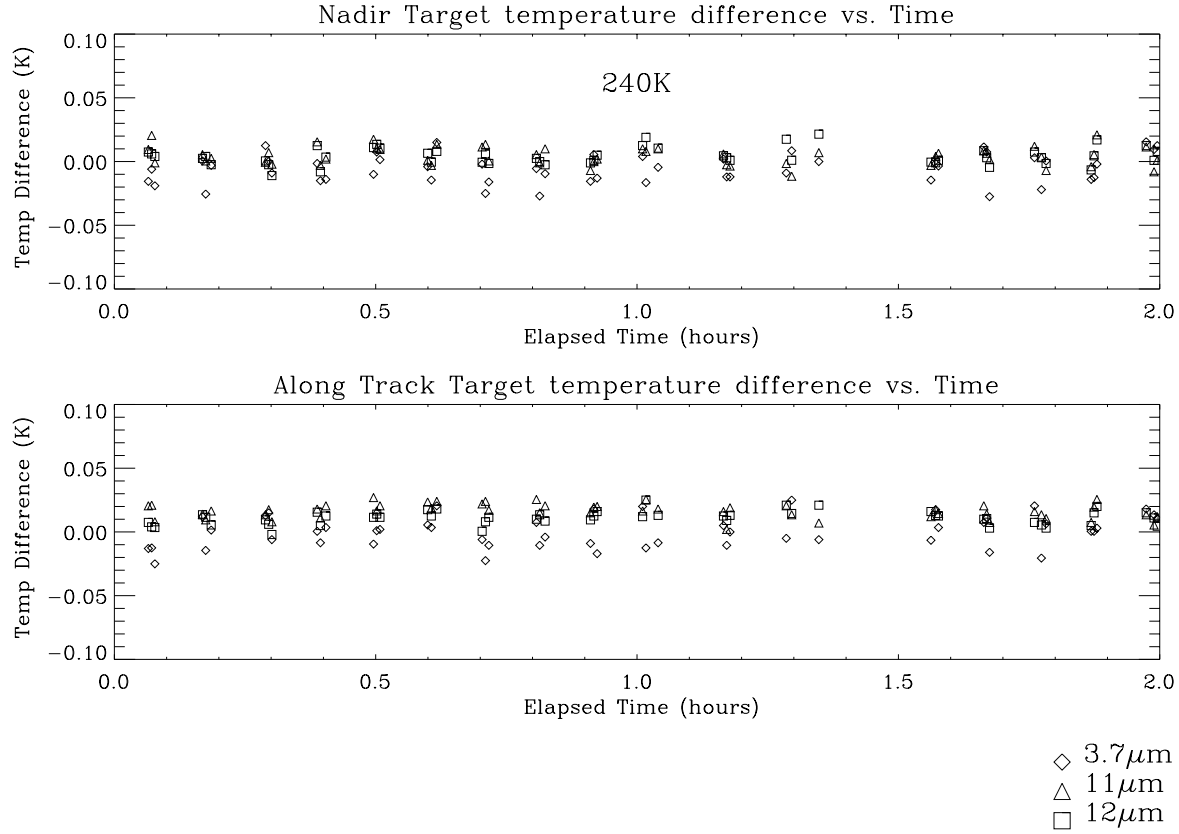

Figure 7.2: Difference between brightness temperatures and actual target temperatures as the ESP temperature was cycled. Both targets were maintained at 240K throughout the cycle.

Alternatively, if the ESP axis were not coincident with the scan axis, the pixels across the blackbody plateaux would not be a uniform radiance. However, as seen in Figure 7.3 for the

nadir target, the scene radiance is constant across the expected 70 pixels. Any variations are within the radiometric noise levels. The same was also observed for the along-track target.

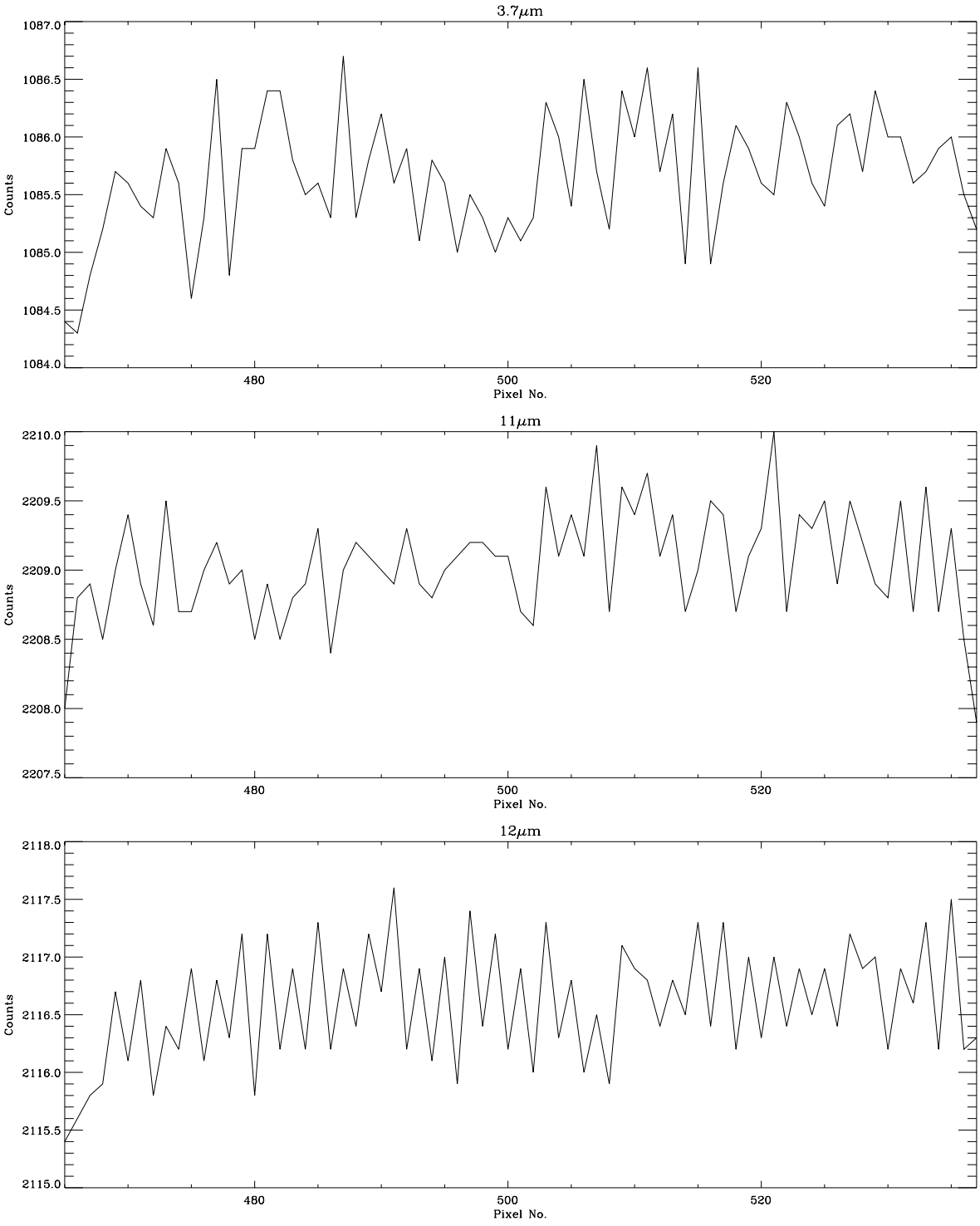

Figure 7.3: Variation in 3.7μm, 11μm and 12μm pixel counts (radiances) across the central pixels of the nadir blackbody at 280K. The pixel counts were averaged over 10 consecutive scans.

7.1.3 Alternate Pixel Integrators

The signals from the detector pre-amplifiers are integrated over 75μs using two integrators for alternate pixels. Because of slight mismatches in the gains and offsets of the two integrators, it is necessary to calibrate the odd and even pixels separately. The odd/even numbering corresponds to the original 2000 pixels. The numbering of the 974 transmitted pixels is derived from the pixel map telemetry, IDF19-IDF29. The effect of the odd/even integrators can be seen in Figure 7.3, which shows the pixel counts for the nadir blackbody at each channel averaged over 10 scans. The 12μm channel appears to show the strongest odd/even integrator difference. The magnitudes of the average differences for >250 pixels plotted against blackbody temperature are shown in Figure 7.4 below. At 3.7μm, the difference is ~0.2 counts and appears to be independent of target temperature. At 11μm and 12μm, the odd/even differences are dependent on scene temperature, confirming that the differences between a channels integrators can be a combination of offset and/or gain.

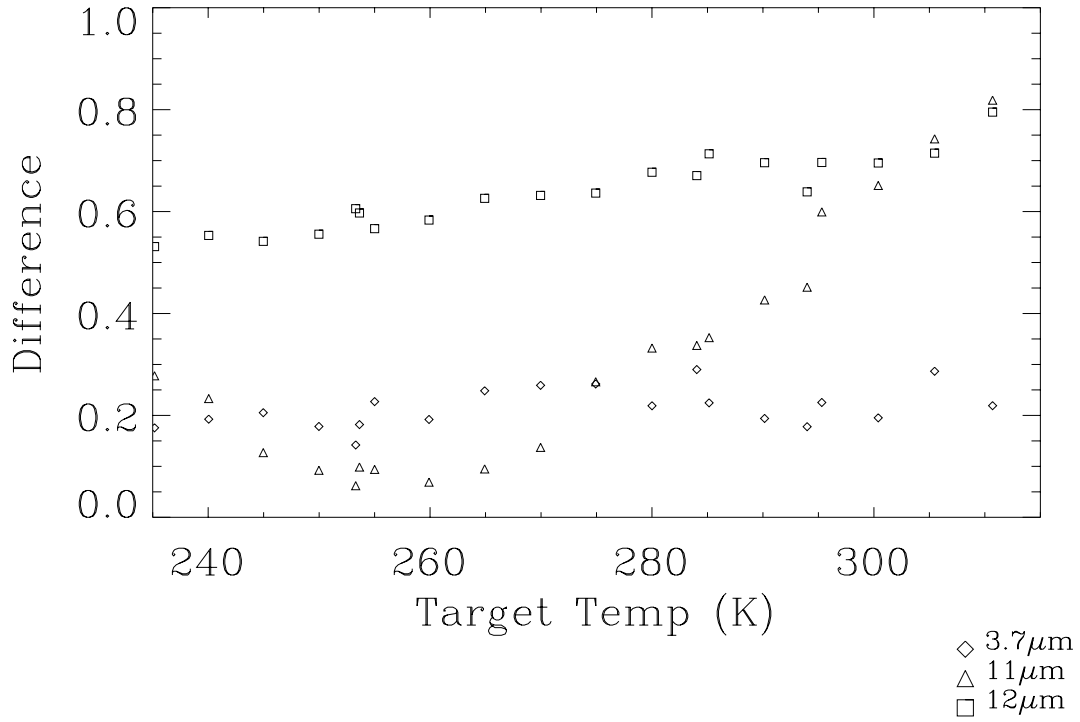

Figure 7.4: Magnitude of the differences between odd and even pixel counts for the nadir blackbody as a function of target temperature.

Once a correspondence between odd/even integrator and pixel number has been established for a scan, it continues as a fixed pattern. The integration periods are essentially a pure 75μs timing sequence, but which of the two possible pixel number to integrator alignments is used depends on the arrival of a scan reference pulse derived from the mechanical scan mirror. This is inevitably subject to mechanical noise. As long as the intervals between scan reference pulses remain very close to 2000 pixels, the alignment is maintained from scan to scan. Checks were applied to the instrument data to look out for

>2001 pixel scan jitters, and any instance of this caused the data block of 10 scans to be discarded. The alignment of the pixel numbers to integrator can be determined from 10 consecutive scans if test results require this information.

7.2 Radiometric Accuracy

7.2.1 Initial Calibration Measurements

Figure 7.5 shows the results from the main calibration run at BOL thermal balance conditions. This consists of measurements of the nadir-view target at 5K intervals between 210K to 315K. The upper plot shows the brightness temperature at 3.7µm, 11µm and 12µm as a function of the actual target temperature. This is taken to be the average of the four RIRTs mounted in the target base-plate. The non-linear behaviour of the channels is shown in the lower plot of the difference between the brightness and actual target temperature. Figure 7.6 shows the same data plotted over a reduced temperature range.

The form of the non-linearity is the same as for ATSR-2, Figure 7.7, although there are some differences in magnitude. The result for the 3.7µm channel is almost identical with a deviation of ~90mK for a target temperature of 275K. At 11µm the non-linearity is slightly less with a deviation of 145mK for the same target temperature compared with 180mK for ATSR-2. The 12µm channel is noticeably more non-linear with a deviation of 290mK compared with 180mK for ATSR-2. The differences should not be of great concern since it is possible to correct for the non-linearity, therefore reducing the 11µm and 12µm differences.

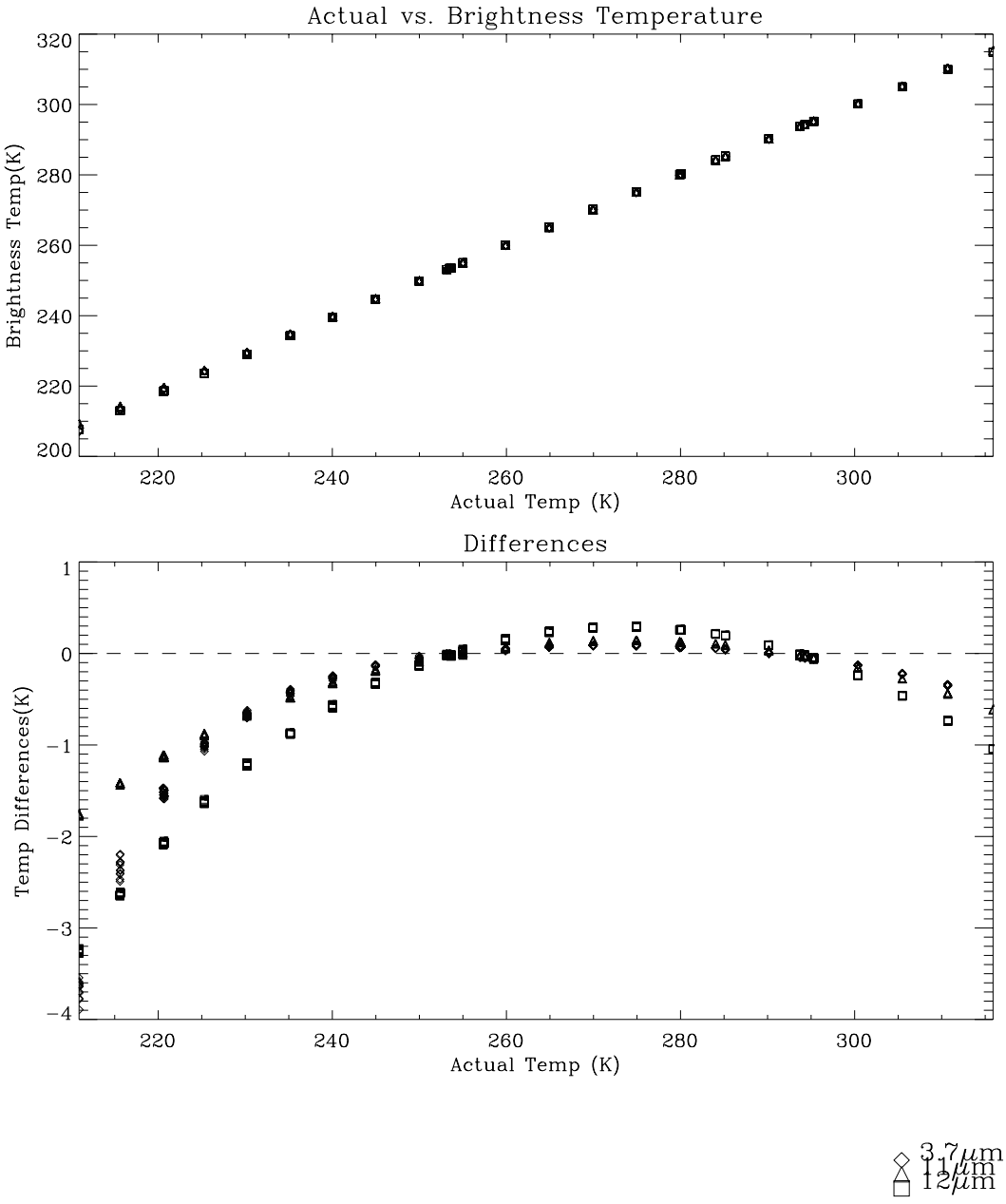

Figure 7.5: Results from radiometric calibration at the centre of nadir-view for BOL thermal balance conditions. The upper plot shows the brightness temperature of the external calibration target as measured by AATSR against the actual target temperature measured by the rhodium iron resistance thermometers. The lower plot shows the brightness temperature minus actual target temperature. No correction for non-linearity has been made at this stage.

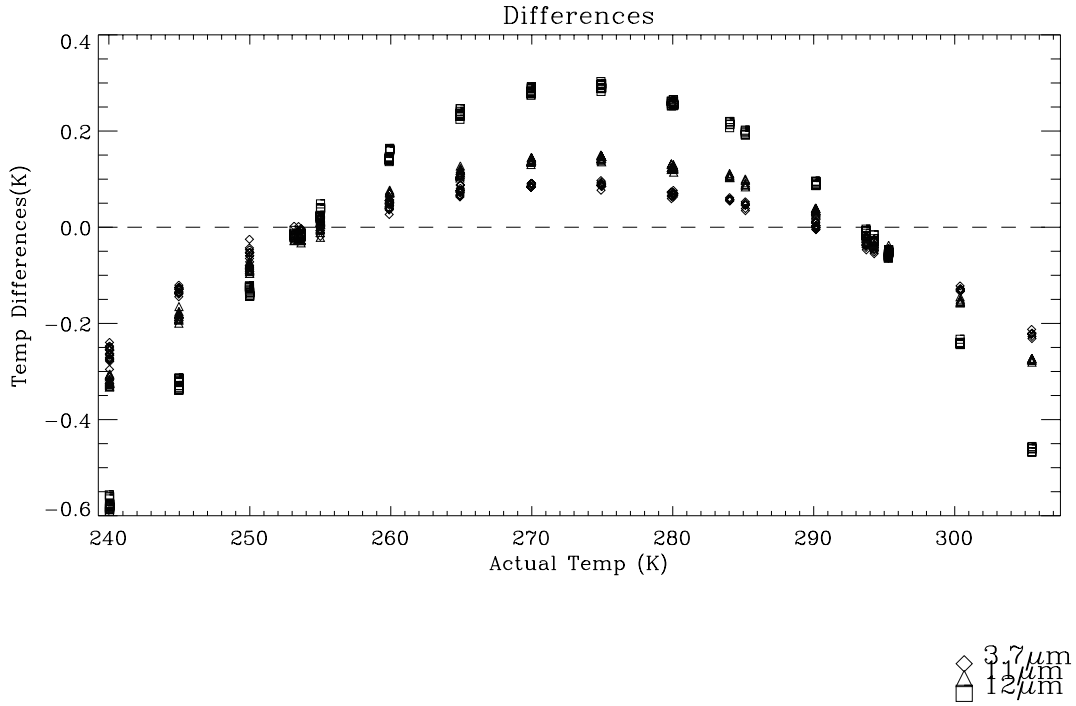

Figure 7.6: Initial results from the radiometric calibration at centre of nadir view plotted over a reduced target temperature range.

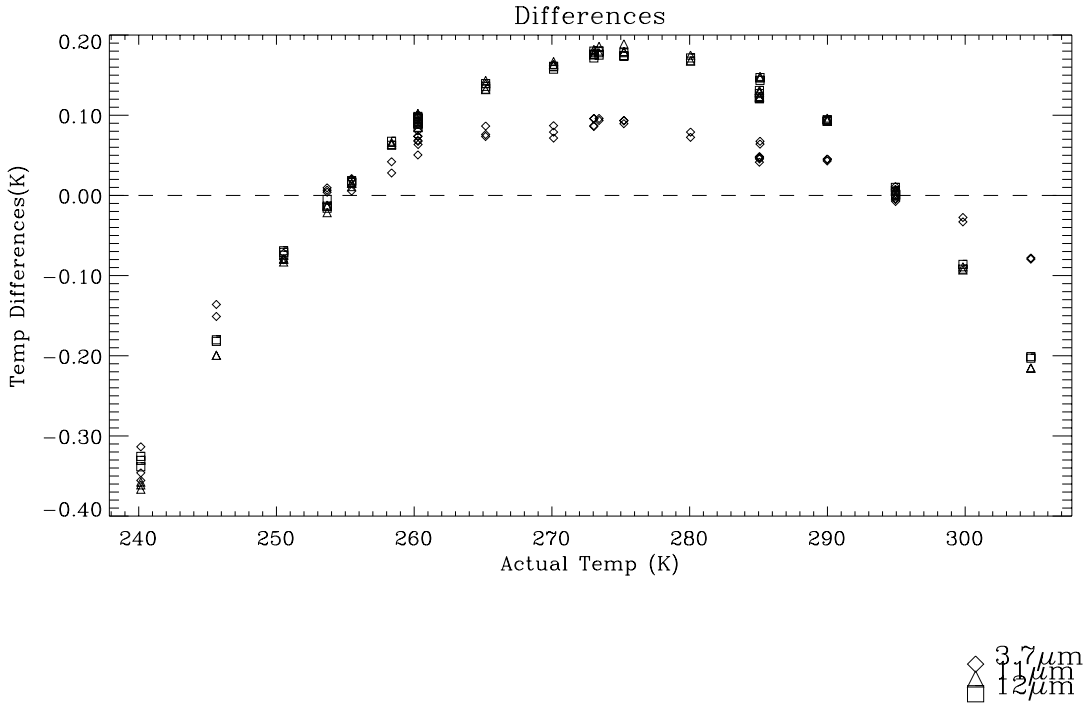

Figure 7.7: Equivalent measurements from ATSR-2 radiometric calibration.

7.2.2 Non-Linearity of 11μm and 12μm Channels

The non-linearity observed in the 11μm and 12μm channels is a known characteristic of the CdHgTe detectors, AD 8. Essentially the electron-hole recombination rate increases as the number of carriers (electrons and holes). The result is a fall-off in the detector's response as the photon-flux increases. This process is described in some detail in the ATSR-1 calibration report, AD 8.

The method for correcting the non-linearity is based on the approach used for ATSR and ATSR-2. Data was used from the low-radiance experiment (RAD15), the centre of nadir calibration (RAD03) and the repeat along-track calibration (RAD16). Data for target temperatures between 130K and 200K were not used because of further uncertainties in the target temperature, not resolved by the initial correction. The measured 11μm and 12μm radiances were normalised between 0.0 and 1.0 (where 0.1 and 1.0 corresponds to Φ_λ(0K) and Φ_λ(320K) respectively. These were plotted against the expected blackbody radiances, Figure 7.9 and Figure 7.10.

For ATSR and ATSR-2, the linear response functions were obtained by fitting a straight line through the low temperature data. However, this failed to produce a satisfactory result for this calibration. It was found that the slope was very dependent on the range of target temperatures used. A more stable result was obtained by fitting a 2nd order polynomial to all the data and using this to obtain the linear function $\Phi_{Lin} = a_0 + a_1\Phi_{bb}$. The slope and offsets for the linear function are given in Table 7-2.

	11μm	12μm
a_0	0.08944	0.07550
a_1	1.04616	1.10257

Table 7-2: Coefficients for linear response function of 11μm and 12μm channels.

The fall-off in response is the ratio of the measured response divided by the linear response function, centre plots in Figure 7.9 and Figure 7.10. The fractional fall off at 310K are given in Table 7-3 and compared with the corresponding values for ATSR and ATSR-2. The fall off in the 11μm channel is comparable to the previous instruments whereas the 12μm is significantly more non-linear.

	12μm	11μm
AATSR	7.2%	3.5%
ATSR-2	3.9%	4.2%
ATSR	4.2%	3.0%

Table 7-3: Percentage fall-off at 310K of 11μm and 12μm channels for all ATSR instruments.

The differences between the instruments may be due to variations in the detector properties. This is probably not surprising given the different manufacturers used. However, a detailed explanation is not essential and will not be discussed in this report.

A least squares polynomial fit was applied to the fractional fall off to enable the fall off to be calculated as a function of the signal radiance, Φ_λ using

$$f_\lambda(T) = z_{0,\lambda} + z_{1,\lambda}\frac{\Phi_\lambda(T)}{\Phi_\lambda(320K)} + z_{2,\lambda}\left(\frac{\Phi_\lambda(T)}{\Phi_\lambda(320K)}\right)^2 \qquad 7.1$$

It should be noted that the best result was obtained by not including in this part of the analysis, data for scene temperatures below 200K. The coefficients $z_{0,\lambda}$, $z_{1,\lambda}$ and $z_{2,\lambda}$ produced by the least-squares fitting are given in Table 7-4.

Coefficient	11µm	12µm
z_0	1.00110	1.00327
z_1	-3.42823×10^{-2}	-8.43871×10^{-2}
z_2	-8.17089×10^{-3}	7.1095×10^{-4}

Table 7-4: Coefficients for calculating fractional fall-off.

The next step was to apply this correction to the radiances such that

$$\Phi'_\lambda = f_\lambda(T)\Phi_\lambda(T) \qquad 7.2$$

For ATSR-1 and ATSR-2 this was applied directly to the temperature-radiance look up tables. However, this approach was not strictly correct because the fall off is a function of the detector signal and is derived from the actual blackbody radiances. This includes a reflected term allowing for the non-unity emissivity of the blackbodies (see equation 4.8). The result may be a small calibration error of a few mK over the normal range of sea surface temperatures. Although the effect may be insignificant, nevertheless, a slightly different method has been adopted for the AATSR calibration.

In addition to the temperature-to-radiance look-up-tables, tables of radiance-to-corrected-radiance have been generated using equation 7.2. The correction is applied to the calibration as illustrated in Figure 7.8. When converting from temperature to radiance, the non-linearity correction is applied after allowing for emissivity. Likewise, when converting from radiance to temperature, the non-linearity correction is applied before correcting for emissivity. Figure 7.11 shows the BOL calibration results for the 11µm and 12µm channel after applying the non-linearity correction.

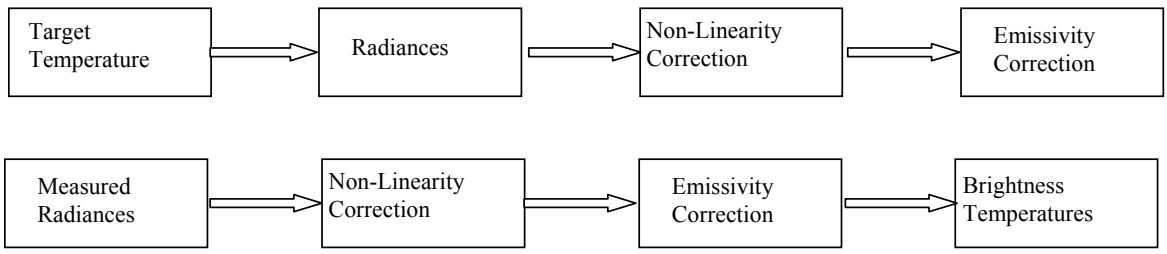

Figure 7.8: Method for applying non-linearity correction to AATSR radiances.

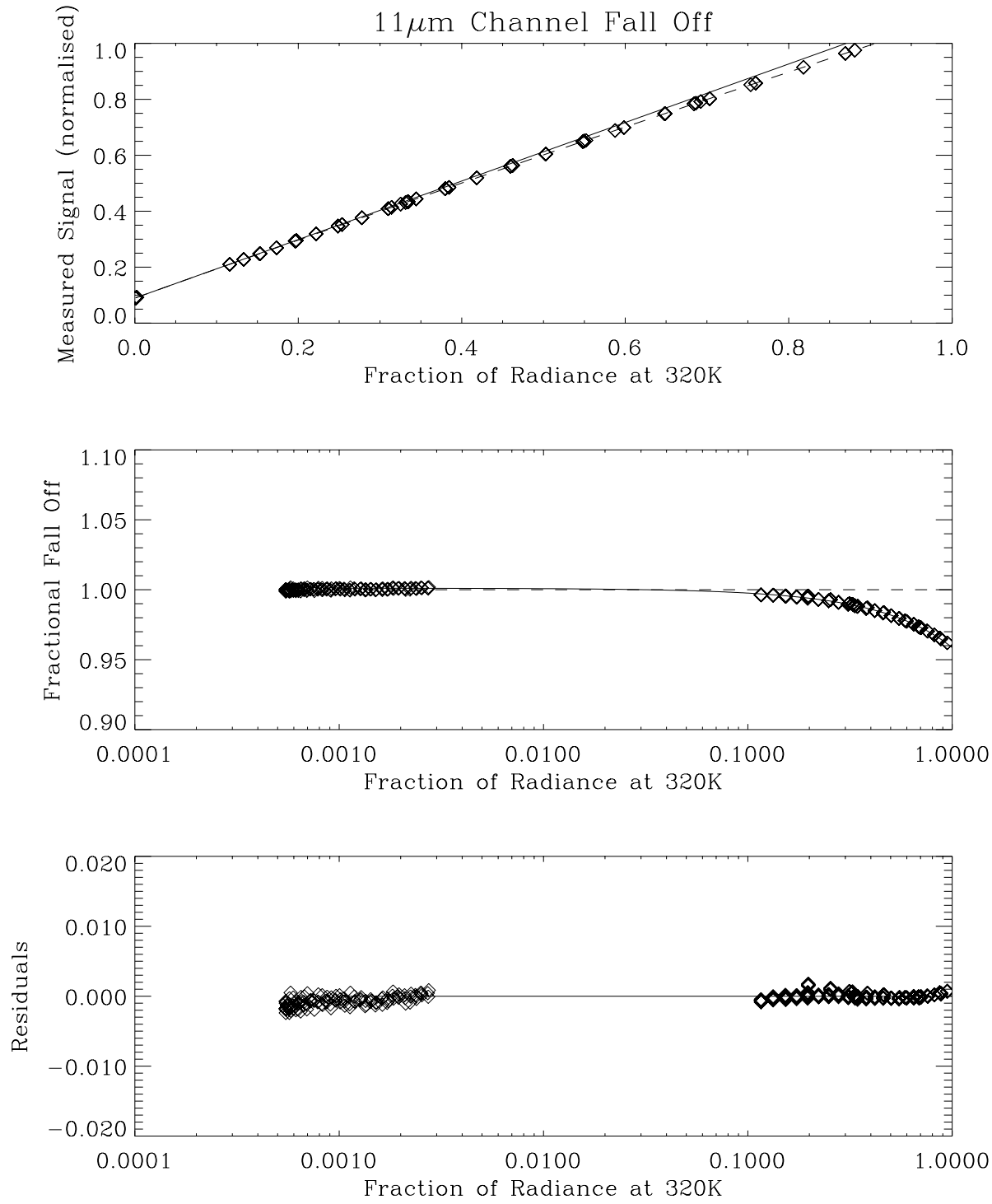

Figure 7.9: (Top) Measured 11μm radiance (normalised) as a function of the expected radiance at 320K. The dashed line is the result of least squares fitting a polynomial through the data. The solid line shows the linear response function. (Centre) Fractional fall-off in the 11μm detector response plotted against the expected radiance. The data was fitted with a 2nd order polynomial (solid line) and the result used to correct for the detector non-linearity. (Bottom) Residuals from least squares fitting process.

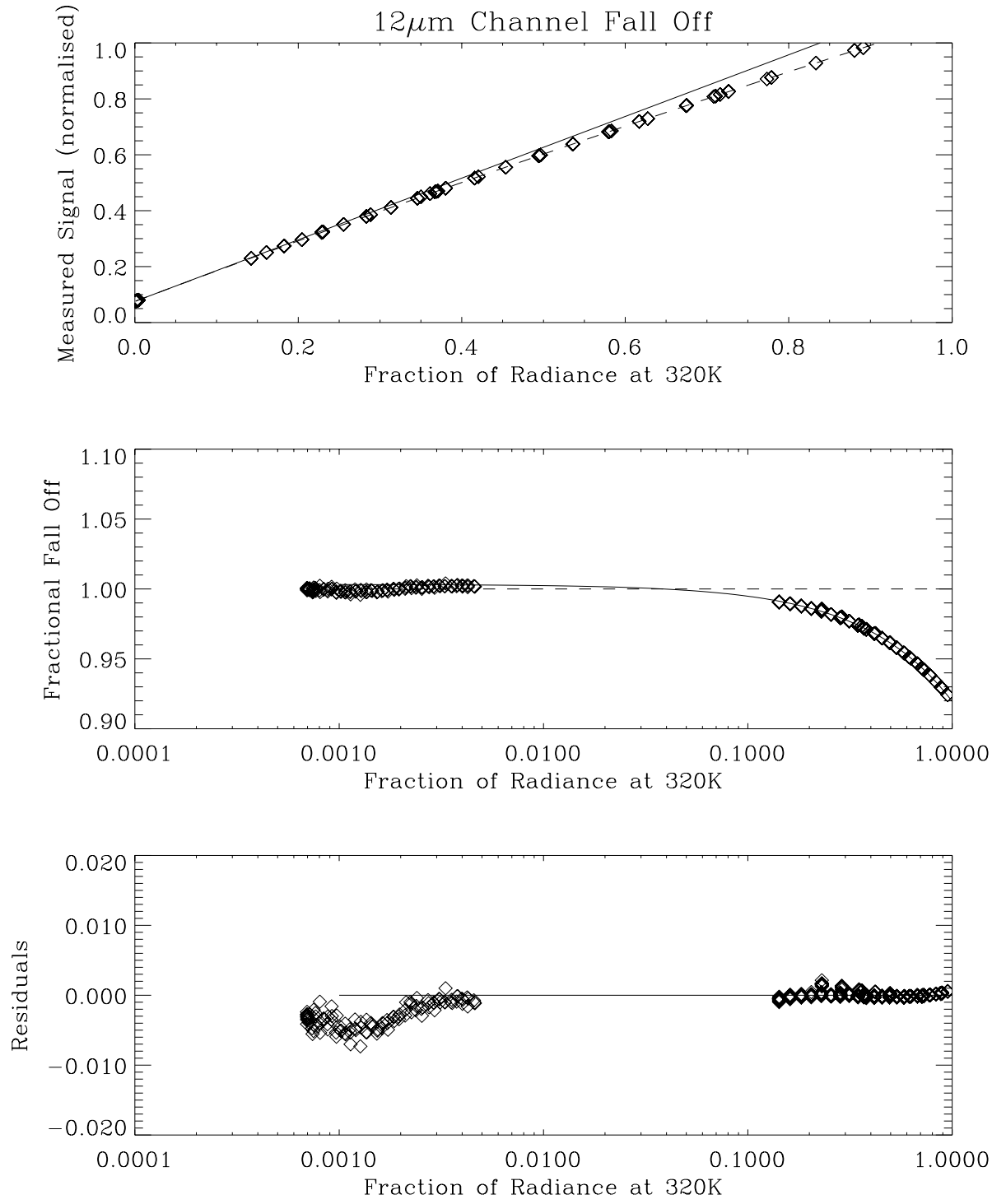

Figure 7.10: As Figure 7.9 but for 12μm channel.

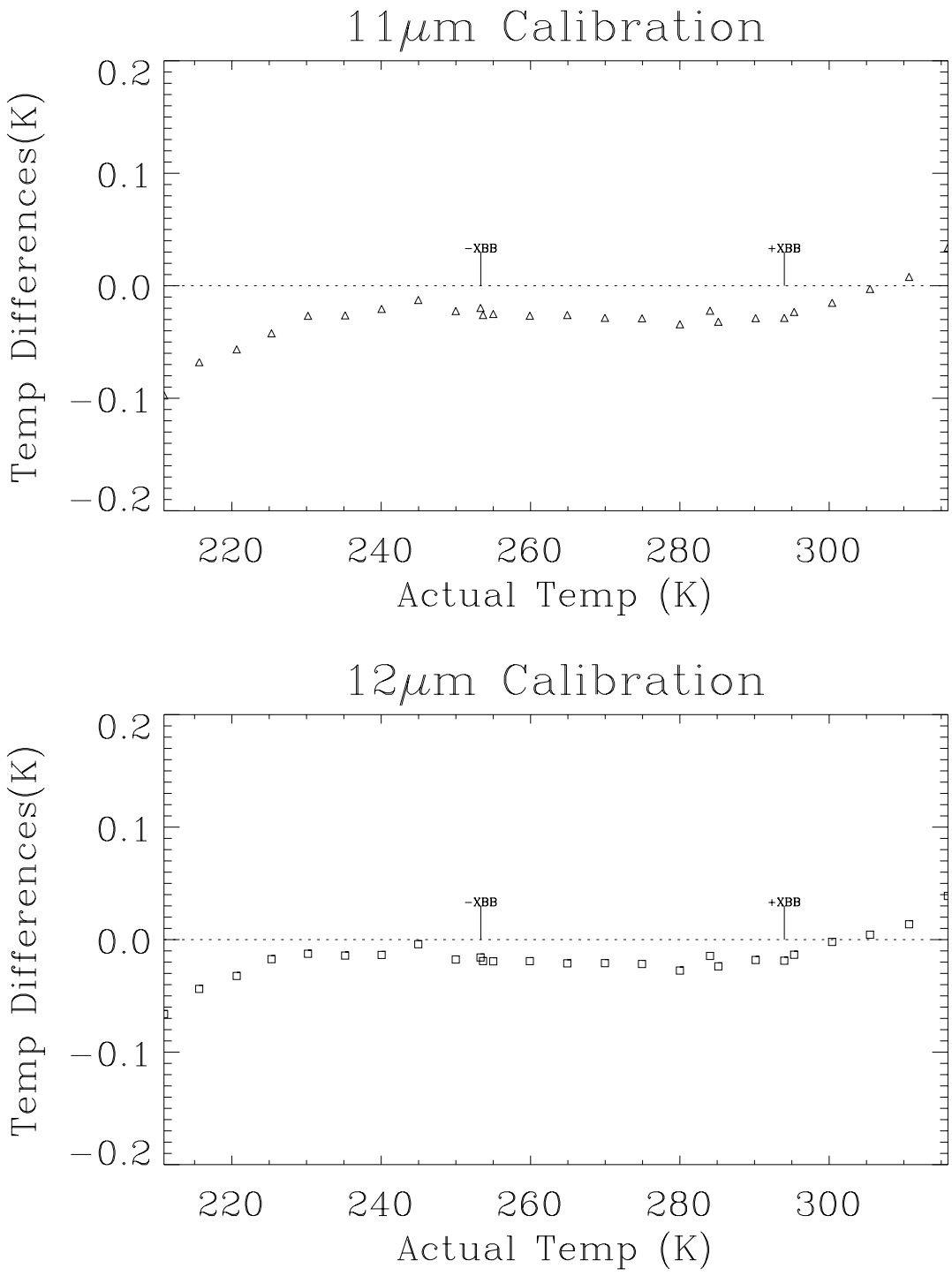

Figure 7.11: The 11μm and 12μm calibration results after correcting for non-linearity. The differences between the measured brightness temperatures and the actual target temperatures are within ±0.05K over the range 240K to 315K. Below 240K, the differences increase.

7.2.3 Non-Linearity of 3.7µm Channel

Non-linear responses have previously been observed in the 3.7µm channels on ATSR and ATSR-2. For ATSR-2 and AATSR, the origin is likely to be a dR/dV coefficient in the hybrid's high valued feedback resistor, though this has not been fully investigated. Previously, correction for the non-linearity has been made by shifting the spectral response of the channel. Although this produced the desired result, there was no scientific basis for the spectral shift. For the AATSR 3.7µm channel, a different approach was taken, based on the correction for the 11µm and 12µm channels.

The radiances for scene temperatures between 180 and 310K were normalised between 0.0 and 1.0 (corresponding to $\Phi_\lambda(0K)$ and $\Phi_\lambda(320K)$ respectively), Figure 7.12 (top). Data below 180K were not used because the measured radiances were not used because of digitisation effects. A 2nd order polynomial was fitted through all the data to produce the linear function with coefficients $a_0 = -5.879 \times 10^{-4}$ and $a_1 = 1.015720$. The measured radiances were then divided by the linear function to give the fractional fall off as shown in the centre plot of Figure 7.12. A least squares polynomial was fitted to these data to enable the fall off to be calculated as a function of the signal radiance, Φ_λ using equation 7.1. The best result was obtained by using only data above 240K, giving the coefficients in Table 7-5.

Coefficient	3.7µm
z_0	1.00020
z_1	-4.90471×10^{-2}
z_2	1.40402×10^{-2}

Table 7-5: Coefficients for calculating fractional fall-off of the 3.7µm channel.

The correction to the radiance to temperature look-up-tables was applied in the same was as the 11µm and 12µm channels. The resulting temperature differences from the BOL calibration are given in Figure 7.13. The differences between 250K and 310K are less than 50mK, through the form of the curve suggests there is a residual error in the target emissivity or background temperatures. This is investigated further in §7.2.4.

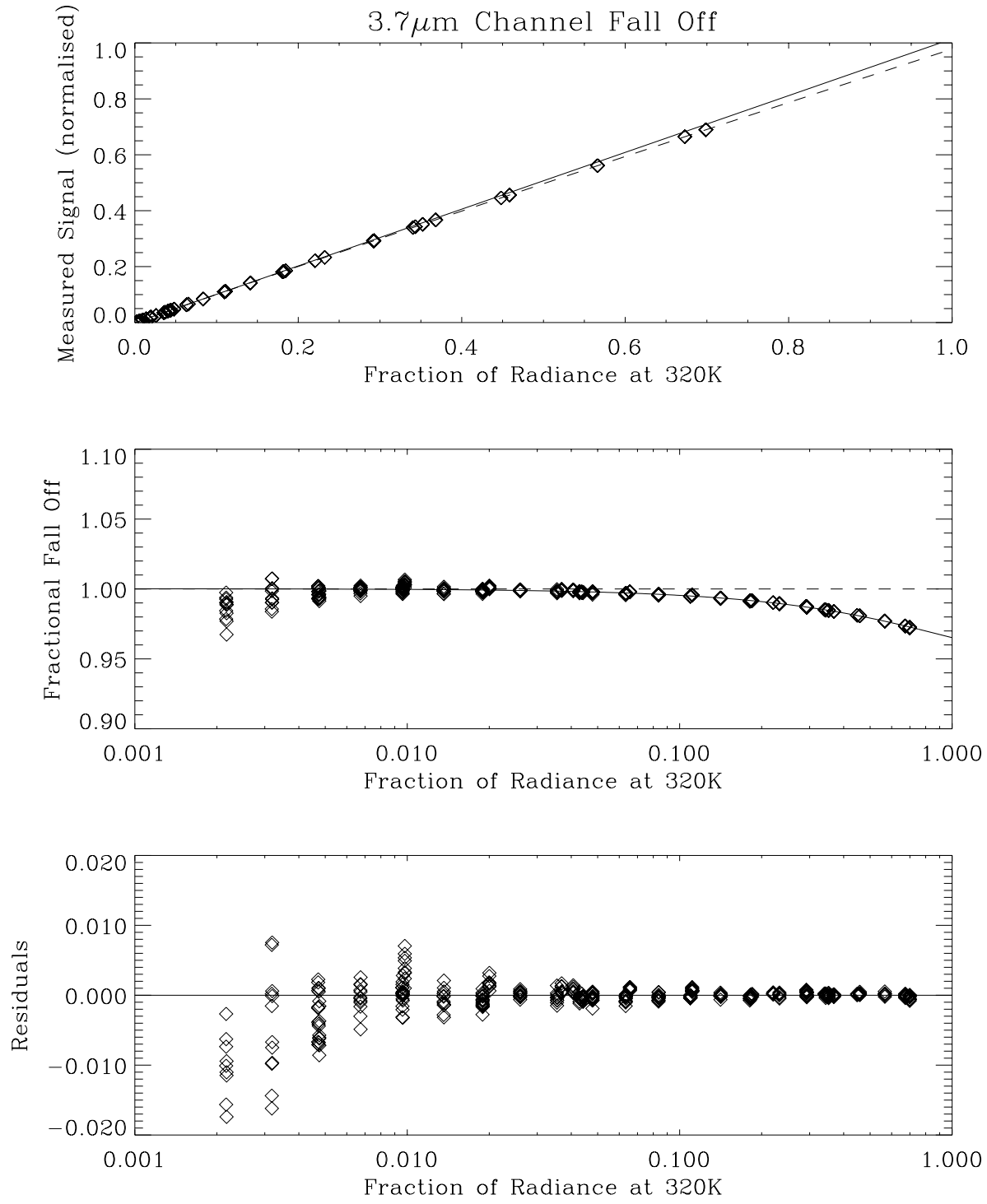

Figure 7.12: As Figure 7.9 but for the 3.7μm channel.

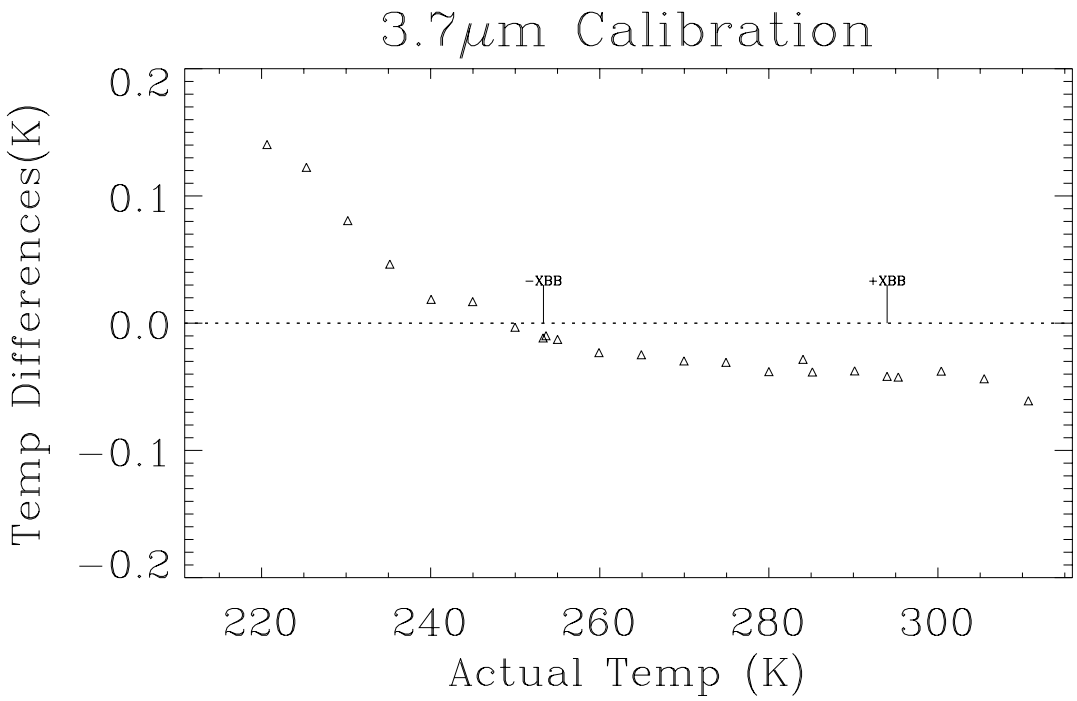

Figure 7.13: The 3.7μm calibration results after correcting for non-linearity. The differences between the measured brightness temperatures and the actual target temperatures are within ±0.05K over the range 240K to 310K. Below 240K, the differences increase suggesting an error in the target emissivity or background temperatures.

7.2.4 Emissivity and Thermometry Errors

For each of the calibration runs, measurements were taken with the external blackbody temperature matched to the on-board target temperatures. These provided direct comparisons between the two sets of targets without the need to correct for detector non-linearity. The differences between the brightness temperatures and actual target temperatures, for all tests at BOL thermal environment, are given in Table 7-6. These data can be used to reveal thermometry and emissivity errors.

Test Number	+XBB Temperature (K)	Brightness Temperature Difference (K)		
		3.7µm	11µm	12µm
RAD03	293.990	-0.042	-0.029	-0.019
RAD07	255.407	-0.009	0.002	-0.002
RAD08	256.819	-0.013	-0.001	-0.005
RAD09	301.635	-0.041	-0.028	-0.025
RAD10	278.509	-0.037	-0.023	-0.019
RAD12	293.865	-0.033	-0.023	-0.014
RAD16	293.506	-0.032	-0.011	-0.006

Test Number	-XBB Temperature (K)	Brightness Temperature Difference (K)		
		3.7µm	11µm	12µm
RAD03	253.340	-0.012	-0.020	-0.016
RAD07	292.697	-0.028	-0.011	-0.008
RAD08	301.370	-0.041	-0.023	-0.018
RAD09	253.510	-0.011	-0.026	-0.020
RAD10	252.261	-0.009	-0.016	-0.014
RAD12	253.129	-0.009	-0.017	-0.014
RAD16	252.422	-0.004	0.001	0.000

Table 7-6: Differences between the brightness temperatures and actual target temperatures, for all tests at BOL thermal environment. Tests RAD03 to RAD12 were done using the nadir view blackbody as the varying target, and RAD16 used the along-track blackbody.

The 'cold' instrument black body is nominally at the same temperature as the rest of the instrument's optical enclosure. Here, the differences between the brightness-temperatures and the actual target temperature, due to $\varepsilon < 1.0$, should be negligible. For the external blackbody, the reflected component of the target radiance is largely dependent on the ESP temperature. At BOL conditions this was ~256K (-17°C). Assuming an emissivity of 0.998 then the maximum temperature error will be < 10mK for all channels. Taking the results from all the nadir target measurements, we obtain an average difference of -15±5mK for the –XBB, and -5±5mK for the +XBB. This does suggest that a thermometry drift in the –XBB. A similar offset was found in the ATSR-2 calibration, and was traced to a shift in the instrument PRT calibrations occurring during the thermal vacuum tests, AD 11. However, the tests using the along-track target show a smaller difference of –2mK, suggesting a possible error in the calibration of the external targets. It will not be possible to completely resolve this until the external target thermometers are recalibrated (expected at the end May 1999). However, the result does put an upper limit on the calibration errors due to thermometry.

Plotting the differences as a function of target temperature, Figure 7.14, reveals a trend in the 3.7μm that may be due to $\varepsilon < 1.0$. The average difference at 293K is -33mK, assuming a 15mK offset error in the thermometry, the difference due to emissivity error is equivalent to –18mK. The effect is not so pronounced in the 11μm and 12μm channels, where the average differences are -18mK and -11mK respectively (-3mK and +4mK after removing 15mK offset). This could explain the result of the 3.7μm calibration, after non-linearity correction, seen in Figure 7.12.

The equivalent data for ATSR-2, Figure 7.15 shows much better agreement over the whole temperature range. This suggests that there is an error in the value of the on-board target emissivity used for the AATSR calibration.

The emissivities used up to this point in the calibration analysis are the values obtained from the measurements made at the MSSL facility, AD 12. The measured values were within 2σ of the calculated emissivities based on measurements of witness samples, Table 7-7. Direct calibration of the blackbody emissivity is a very difficult measurement to make and requires a full understanding of the background sources. The measurement errors are large (60mK at 3.7μm) compared to the required accuracy of the emissivity (35mK). In addition, the measurements, which covered a wider spectral band (3 to 6.5μm) than the 3.7μm channel, were intended as a confirmation of the calculated value rather than an absolute measurement. It is therefore most likely that the calculated values are a better representation of the true target emissivity.

	FM01 (-XBB)		FM02 (+XBB)	
	Calculated	Measured	Calculated	Measured
3.7μm	0.99745	0.99697±0.0025	0.99745	0.99614±0.0025
11μm	0.99898	0.99960±0.0005	0.99898	0.99909±0.0005
12μm	0.99892	0.99937±0.0005	0.99892	0.99883±0.0005

Table 7-7: Calculated and measured emissivities of the AATSR FM blackbodies.

Substituting the calculated emissivities into the calibration algorithm gives a much better agreement between the brightness temperatures and the actual target temperatures, Figure 7.16.

Please note that the conclusions do not completely explain the cause of the observed temperature differences. It has been assumed that the temperatures measured by the thermometers are the same as the radiating surface of the blackbody. This is true if the thermometers are in good thermal contact and are completely isolated from the external environment (i.e. electronics). However, there may a significant thermal resistance between the thermometers in the base-plate to the radiating surface, and increased coupling to the environment via the thermometer wires. The overall effect would be a temperature difference between the thermometer and radiating surface. This would not only be a function of the blackbodies own temperature but also that of its surroundings. This caveat does not affect the data analysis because even if the effect includes non-radiative components, provided it can be numerically modelled as an ‘effective emissivity’, the parameterisation of the calibration is applicable to processing in-flight data.

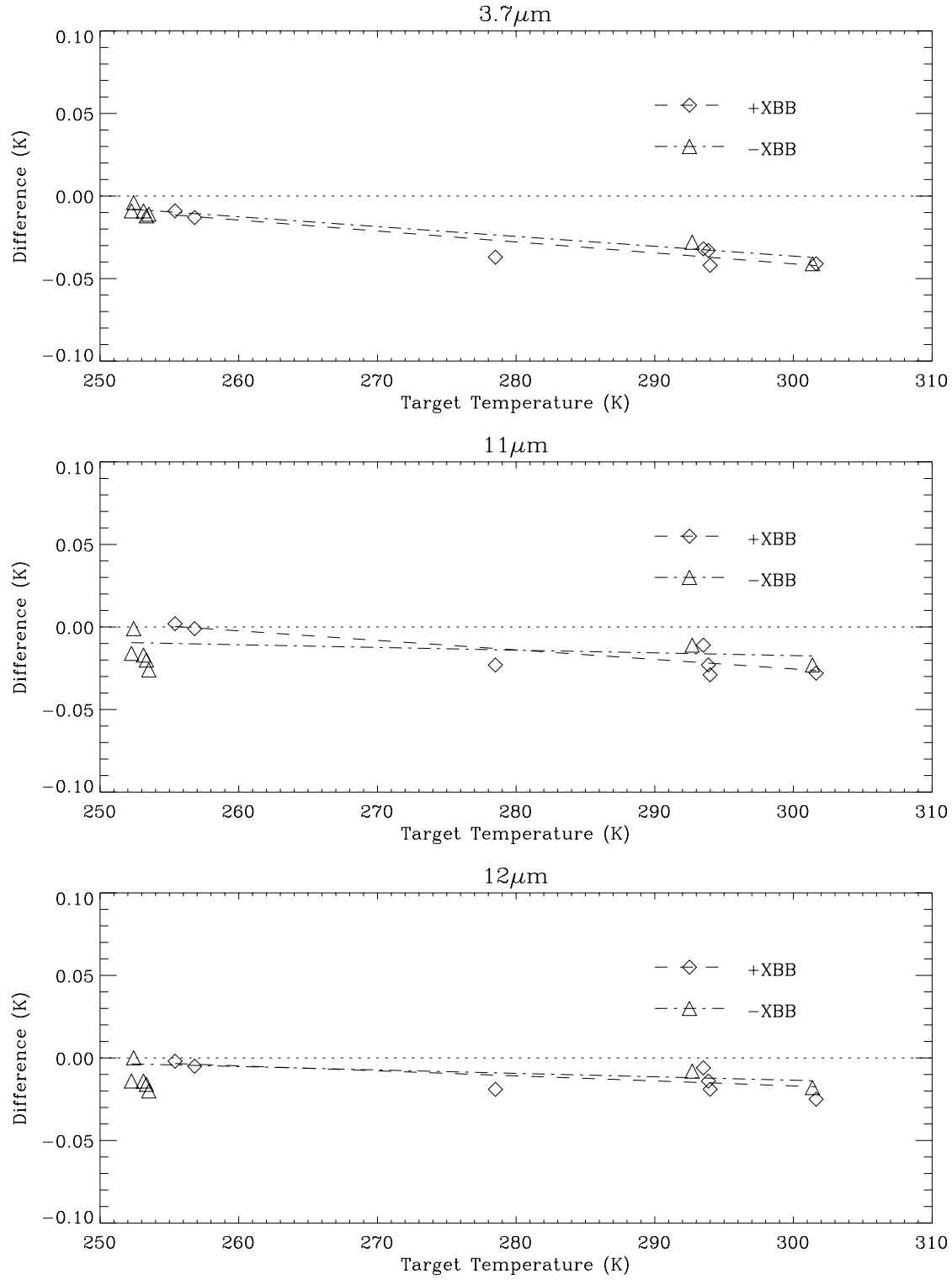

Figure 7.14: Differences between the brightness temperatures and actual target temperatures, for all tests at BOL thermal environment, using measured on-board emissivities supplied with units.

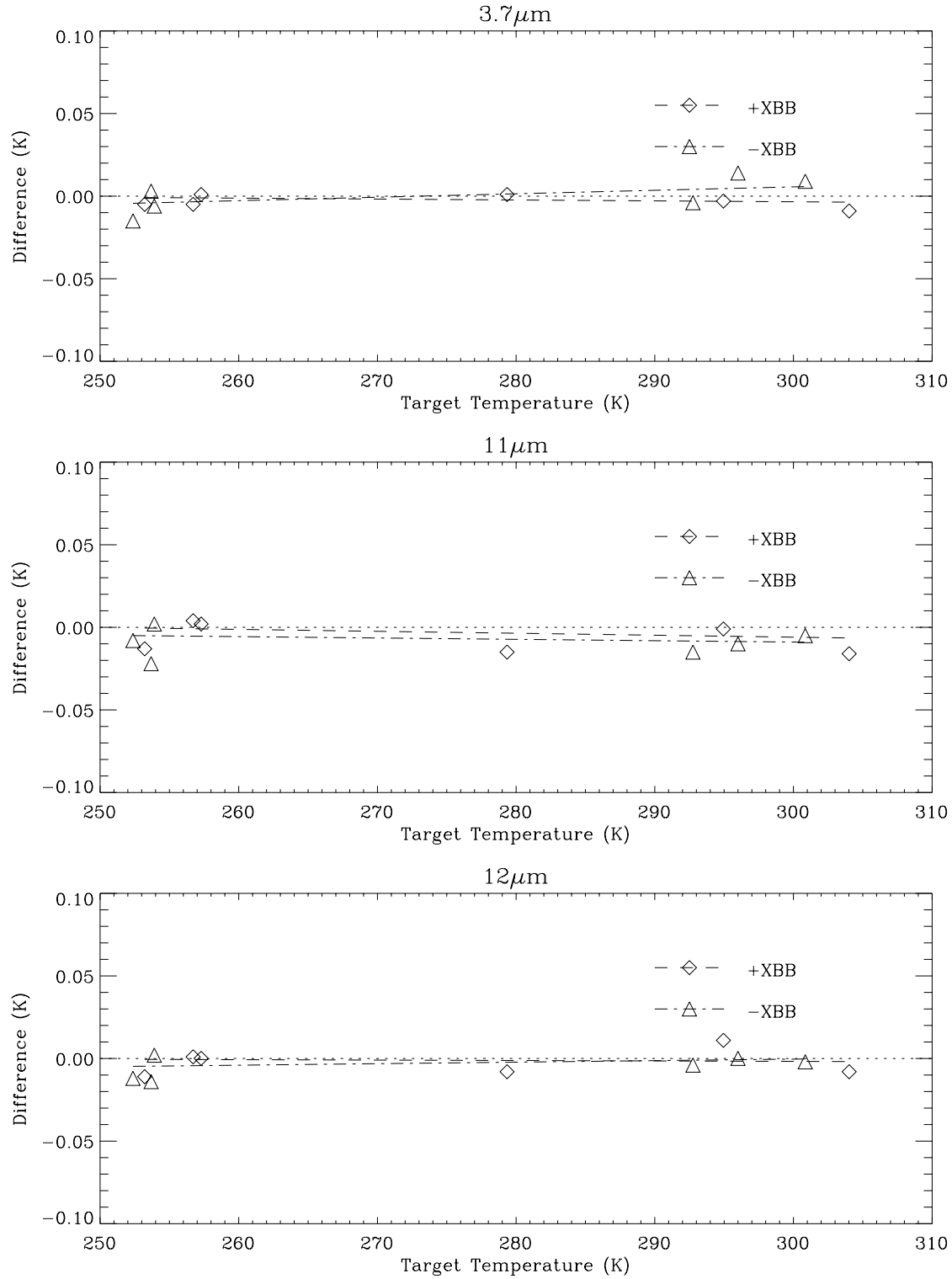

Figure 7.15: As Figure 7.14 but for ATSR-2.

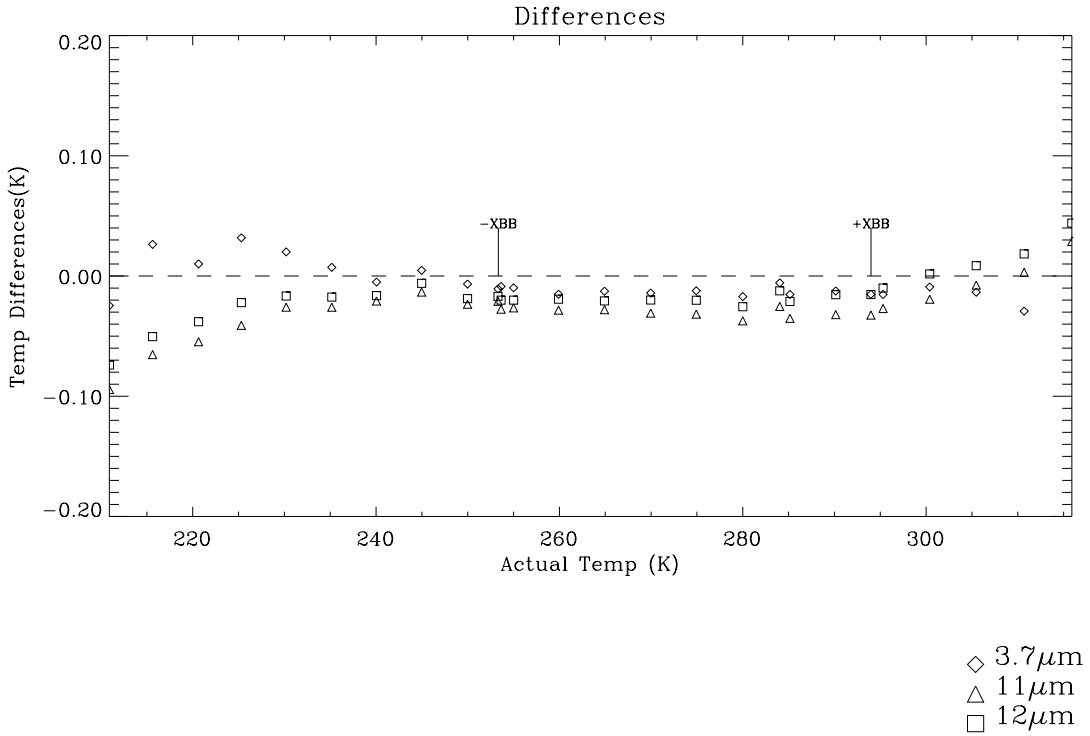

Figure 7.16: Results from calibration at the centre of nadir view at beginning-of-life, recalculated using the computed on-board blackbody emissivities. This shows much better agreement between the brightness temperature at 3.7μm and the actual target temperature.

7.3 Radiometric Noise

For each radiometric measurement, the value of the NEΔT for each channel was calculated using equation 4.10. Figure 7.17 shows the NEΔTs plotted as a function of target temperature for the BOL calibration at the centre-of-nadir view. At 270K the NEΔTs at 3.7μm, 11μm and 12μm are 37mK, 25mK and 23mK respectively. The rise in NEΔT as the target temperature decreases is purely related to $\partial\Phi/\partial T$ as a function of scene temperature. Plotting the radiometric noise as counts, Figure 7.18, we see that the 11μm and 12μm noise remains constant over all scene temperatures. For these channels, the dominant noise sources are digitisation and Johnson noise. This is also the case at 3.7μm for low photon fluxes (T_{scene} < 250K). At higher photon fluxes, the 3.7μm noise becomes dominated by statistical photon signal noise.

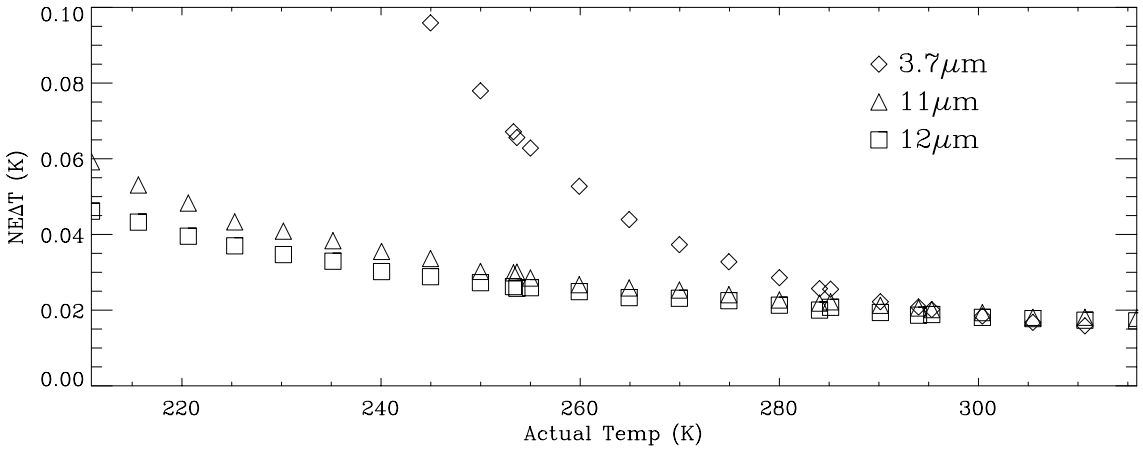

Figure 7.17: NEΔT as a function of target temperature for AATSR at BOL thermal conditions.

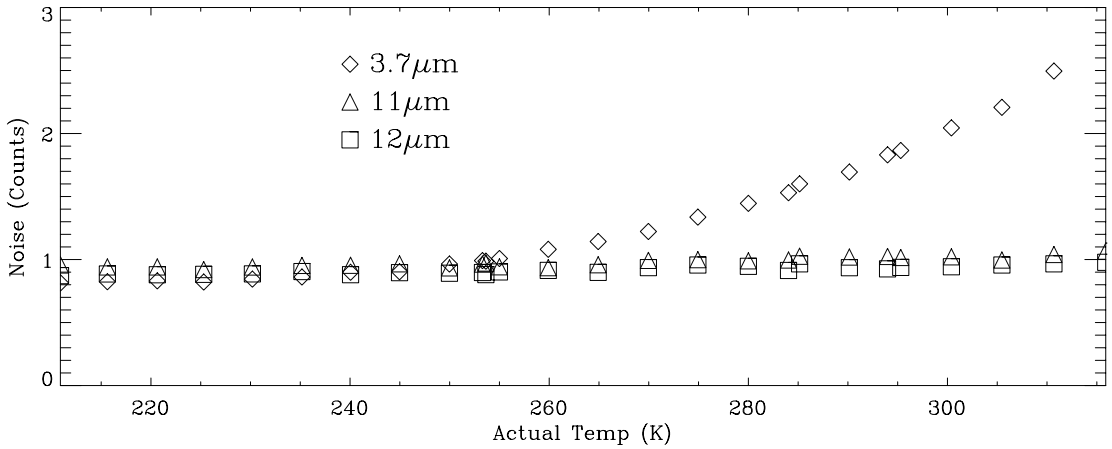

Figure 7.18: Signal channel counts noise as a function of target temperature for AATSR at BOL thermal conditions.

The noise levels compare well with the ATSR-2 measurements, Figure 7.19. They are considerably better than those observed during the first AATSR calibration in February 1998, Figure 7.20 which included noise from a significant breakthrough of a component at 260Hz. This extra noise caused typical peak-to-peak amplitudes at 290K to be 0.05K and

0.1K at 11µm and 12µm respectively, although higher levels were detected. This effect was not observed during the ATSR-2 caibration, Figure 7.19. The noise was traced to microvibration of the FPA baseplate causing the area viewed by the detector to oscillate on the field-stop. The microvibration was induced by vibrations from the rotation of the scan mechanism transmitted through the structure and FPA mount. A study of the scan mechanism vibration and transmission was performed by MMS, but no quantitative conclusion could be drawn as to how the level of vibration at source related to the observed radiometric noise. Analysis of the results of measurements and optical modelling carried out by RAL showed that the magnitude of the noise levels was partly related to the level of misalignment of the detectors. Using data from the field-of-view tests, and further measurements by AUSPACE, it was found that the 11µm detector was misaligned by 10µm and the 12µm detector by 40µm. The latest results show that realignment and stiffening of the cooler braid, have reduced the microvibration-induced noise to below the thermal noise level as long as the scan mirror run well. Full details of the noise investigations are given in the MRB documentation, AD 7.

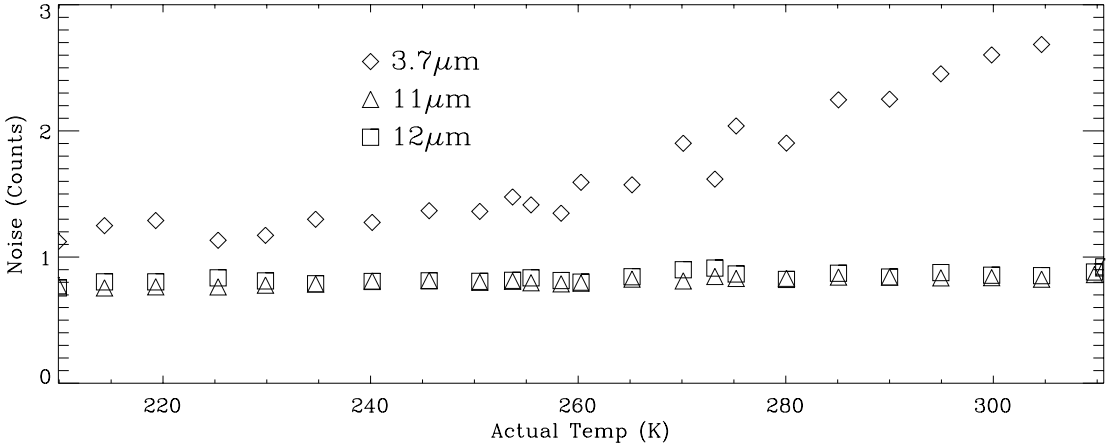

Figure 7.19: Signal channel counts noise from ATSR-2 calibration at BOL thermal conditions.

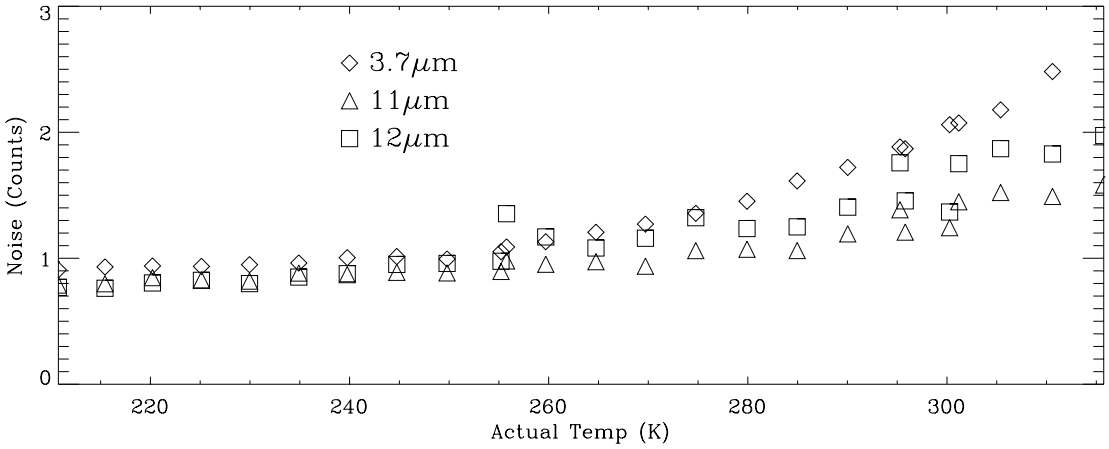

Figure 7.20: Signal channel counts noise from AATSR calibration tests performed in February 1998. The increase in the 11µm and 12µm noise level at higher scene temperatures is due to the breakthrough of a 260Hz component.

Although the 260Hz noise had been reduced to background levels, further episodes of microvibration induced noise began to manifest itself during the calibration. This was first observed during the EOL thermal balance test on the EGSE scan display workstation, Figure 7.21. Radiometric measurements showed that the 12µm NEΔT had increased to >50mK for a scene temperature of 285K.

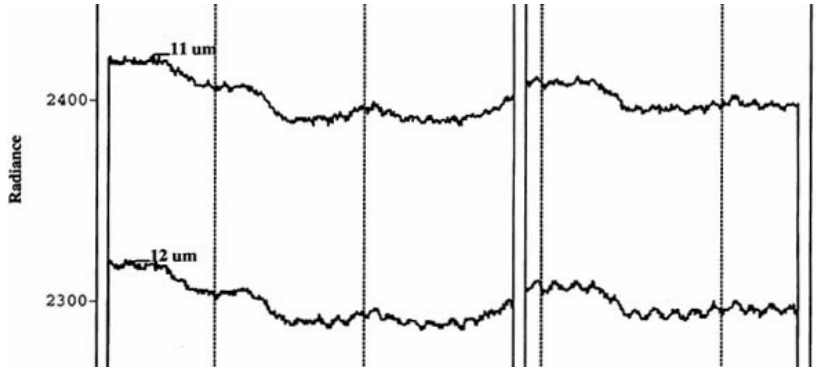

Figure 7.21: Extract from screen dump of EGSE scan display showing the 11µm and 12µm pixel counts for the nadir and along track views. In the test, the ESP and blackbodies were at the same temperature so the instrument is effectively viewing a uniform scene. The ripples in the signal are the microvibration induced noise, while the larger variations are due to temperature gradients in the ESP.

A Fourier analysis of this noise showed that the main frequency was now at ~500Hz. This was entirely consistent with the optical modelling, which showed that if the detectors were well aligned then the chopping would apply to both edges, giving a noise frequency double the FPA baseplate fundamental frequency. However, although the optical modelling could predict the frequency, it could not explain why the noise had increased beyond the background levels.

In response to the MRB's investigation of FPA noise problem, an accelerometer had been mounted onto the instrument structure, next to the FPA mounting ring, so that the vibration levels could be monitored during the in-vacuo tests. A spectrum of accelerometer signal, taken when the 500Hz noise was visible, showed that the vibration levels had significantly increased since the start of the calibration, Figure 7.22. The impact of such 500Hz noise on the science data has yet to be investigated.

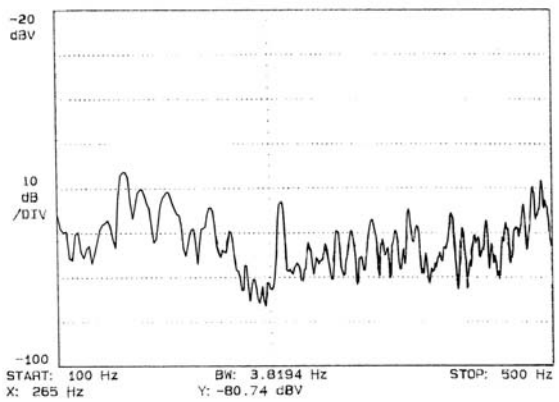

(a)

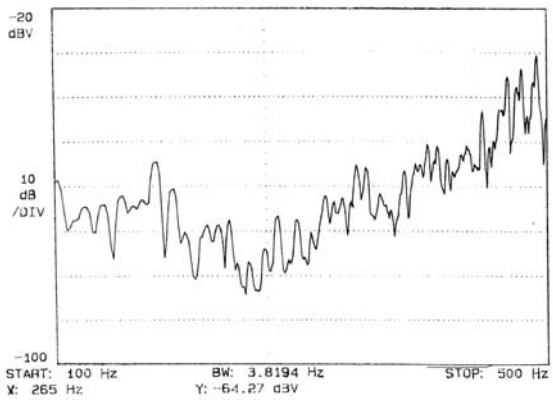

(b)

Figure 7.22: Accelerometer plots taken at (a) the start of calibration at BOL conditions and (b) EOL thermal balance tests when microvibration noise was present. The second trace clearly shows an increase in noise level higher frequencies.

The accelerometer data were the first real evidence linking the scan mechanism behaviour with the microvibration noise. Further observations showed that the noise returned to background levels as the vibration reduced.

The increase in vibration was connected with a transition from 'cold' BOL thermal balance conditions to 'hot' EOL conditions, during which the SMU temperature had increased by approximately 10°C. This would have affected the lead lubrication of the mechanism bearings. Before the EOL case, the instrument had been operating at BOL conditions for about 2.5 weeks and the bearings would have been running on an established lubricant track. As the temperature increased, a new lead lubricant track would have to be laid down, resulting in increased torque noise. It was believed that as the temperatures stabilised, and the new track became established, the vibration levels would reduce. This was observed after a few hours, with an accompanying decrease in radiometric noise. Yet, there were periodic bursts of rough running and higher radiometric noise. It was also hoped that as the instrument returned to BOL conditions, the vibration levels would recover significantly. This did not happen. Although the noise levels were generally acceptable, there were several periods throughout the remainder of the calibration tests where there was an increased level of vibration. This affected the duration of the calibration because the test procedures and calibration software had to wait and reject any long periods of data in order to select periods with the required low noise levels for the measurements.

Because the behaviour did not match expectations, concern grew that the mechanism was showing signs of deterioration. However, the considered view of ESTL and MMS was that the increased level of vibration was caused by bearing cage hang-up result from running the mechanism horizontally in 1g for extended periods. By the end of the calibration, the SMU had been run for approximately 22million revolutions (not counting the previous calibration). Similar behaviour had been experienced during testing on other space-projects, but smooth running had always recovered after running vertically. Likewise, it was anticipated that the AATSR mechanism would show a similar recovery. The view was reinforced after an inspection of the mechanism showed that the cage was in good condition after the calibration, and confirmed when running the mechanism vertically for a few days significantly reduced the bearing torque as predicted.

It is therefore hoped that the radiometric noise will be at nominal levels with no significant breakthrough of vibration induced noise. This will depend entirely on the eventual performance of the scan mechanism.

7.4 Calibration with FPA at 90K

To investigate the sensitivity of the radiometric response to changes in detector temperature, the calibration was repeated with the FPA at 90K. The differences between the brightness temperatures and actual target temperature are presented in Figure 7.23. The conversion from counts to radiance was performed using the non-linearity correction for 80K detectors. The results show that the 3.7µm channel is only slightly affected by the increase in scene temperature. As with ATSR-1 and –2, the 11µm and 12µm channel responses are more strongly dependent on detector temperature. With the 11µm channel, the result shows that it would be possible to get away without changing the non-linearity correction and still measure brightness temperatures to ±0.1K. A much stronger variation is seen in the 12µm channel. The non-linearity for this channel would clearly need to be treated as a function of detector temperature. Additional work would be necessary to derive correction parameters for 90K detectors if so required. However, it should not actually be needed for flight because it is hoped that the detectors will not be run at 90K.

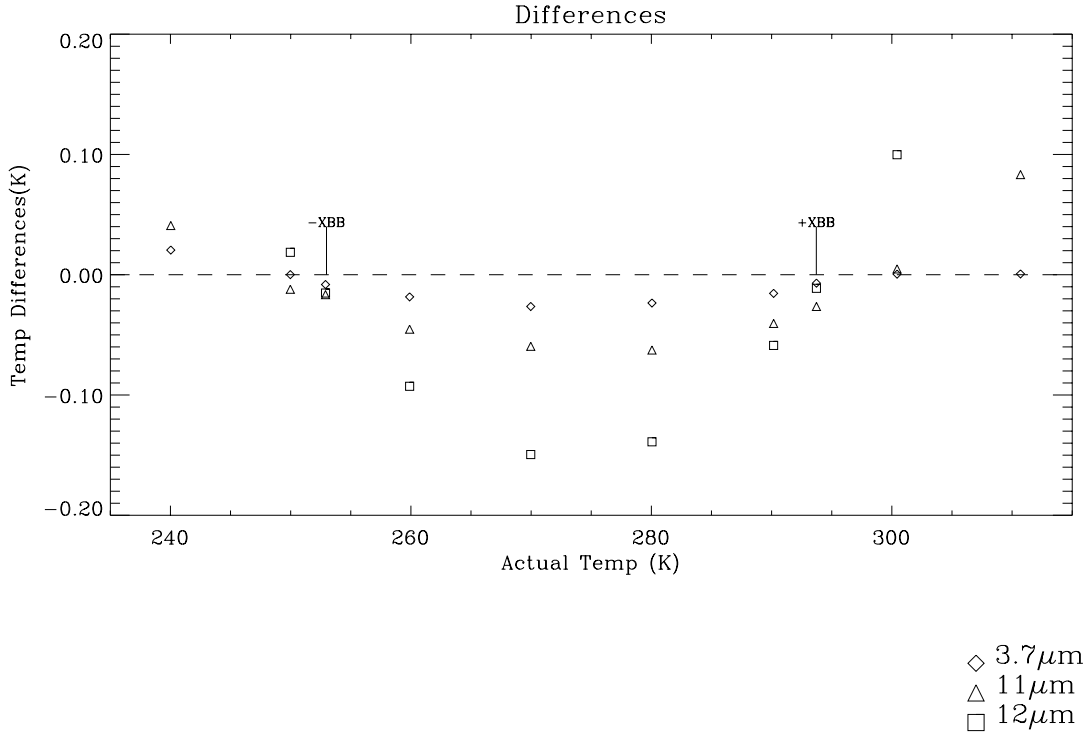

Figure 7.23: Radiometric calibration result for detectors operating at 90K.

Comparing the pixel noise and NEΔTs for the two detector temperatures, Figure 7.24, show a clear increase in the 11µm and 12µm noise in the warmer case. The NEΔTs for a blackbody at 270K are given in Table 7-8. This result is as expected, and is in good agreement with ATSR-1 and –2, and clearly shows the baseline is to run the FPA at 80K and not 90K.

	FPA at 80K	FPA at 90K
3.7µm	37mK	37mK
11µm	25mK	39mK
12µm	23mK	37mK

Table 7-8: NEΔTs for 270K scene temperature with FPA at 80K and 90K.

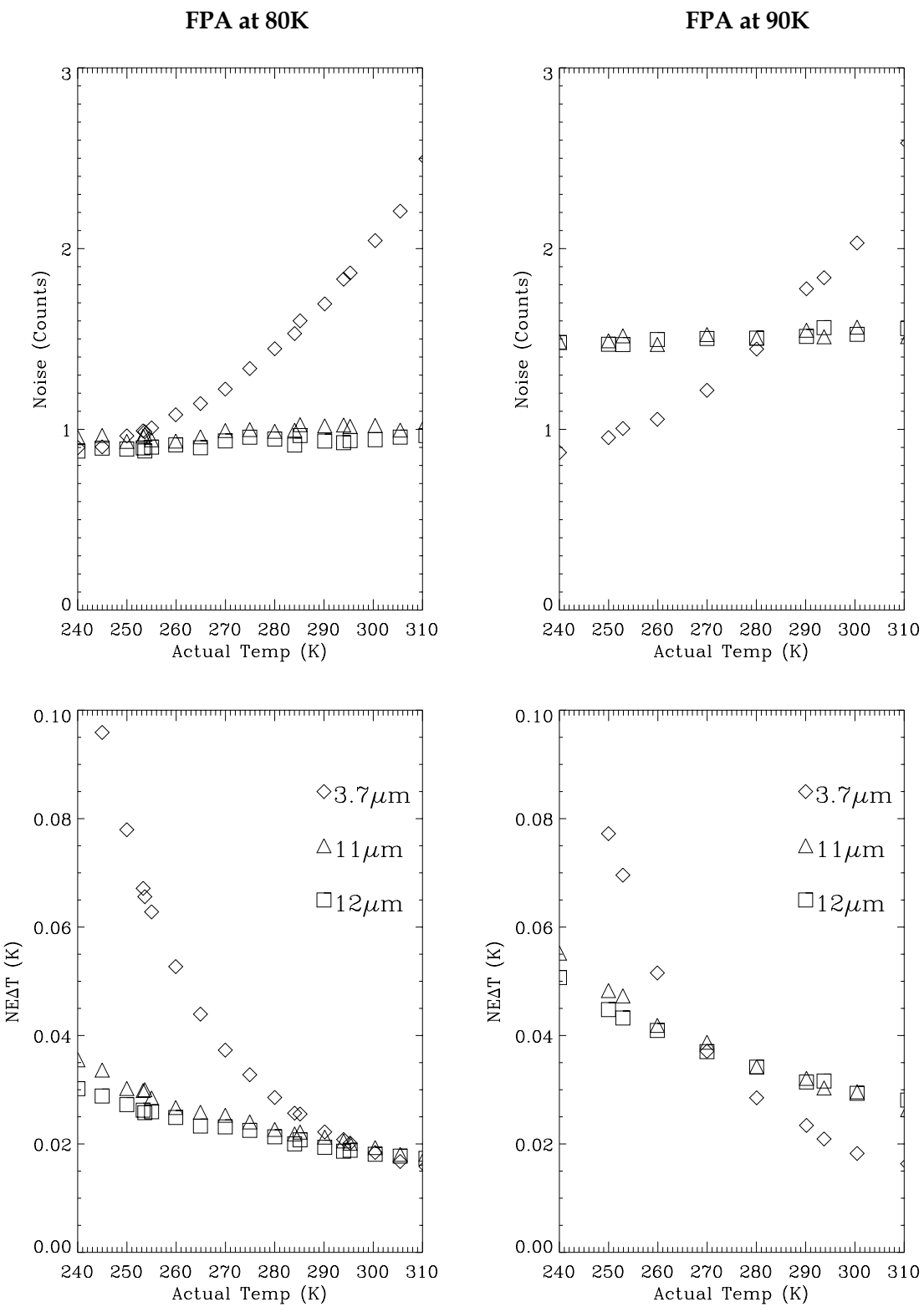

Figure 7.24: Pixel noise and NEΔTs for detectors operating at 80K and 90K respectively.

7.5 Scan Dependent Effects

To investigate any scan-dependent effects the calibration was verified at all points around the scan cone (RAD05 and RAD06). The tests were performed at BOL thermal conditions with the targets at 240K, 270K, 280K, 310K and the temperatures of the on-board blackbodies (253K and 294K). To ensure that all nadir and along track pixels were covered, calibration points were taken with the blackbodies positioned at ±46°, ±40°, ±33°, ±30°, ±22.5°, ±15°, ±7° and 0°. The blackbody temperatures were allowed to stabilise before taking the measurements.

Figure 7.25 and Figure 7.26 show the results of these measurements corrected for the non-linear responses of the detectors. A summary of the range of temperature differences for each target temperature is given in Table 7-9. The results show no significant scan-dependent effects. Any variations that are seen are within acceptable limits and may be due to slight drifts in the target temperature over the course of the test.

Temperature	Channel	Nadir	Along
240K	3.7µm	0.021K	0.013K
	11µm	0.027K	0.022K
	12µm	0.018K	0.016K
253K	3.7µm	0.017K	0.015K
	11µm	0.021K	0.021K
	12µm	0.013K	0.016K
270K	3.7µm	0.015K	0.006K
	11µm	0.020K	0.020K
	12µm	0.019K	0.014K
280K	3.7µm	0.013K	0.010K
	11µm	0.022K	0.022K
	12µm	0.015K	0.016K
294K	3.7µm	0.010K	0.019K
	11µm	0.016K	0.020K
	12µm	0.012K	0.018K
310K	3.7µm	0.013K	0.005K
	11µm	0.021K	0.014K
	12µm	0.019K	0.006K

Table 7-9: Range of temperature differences at each target temperature, for the calibrations around nadir and along-track views.

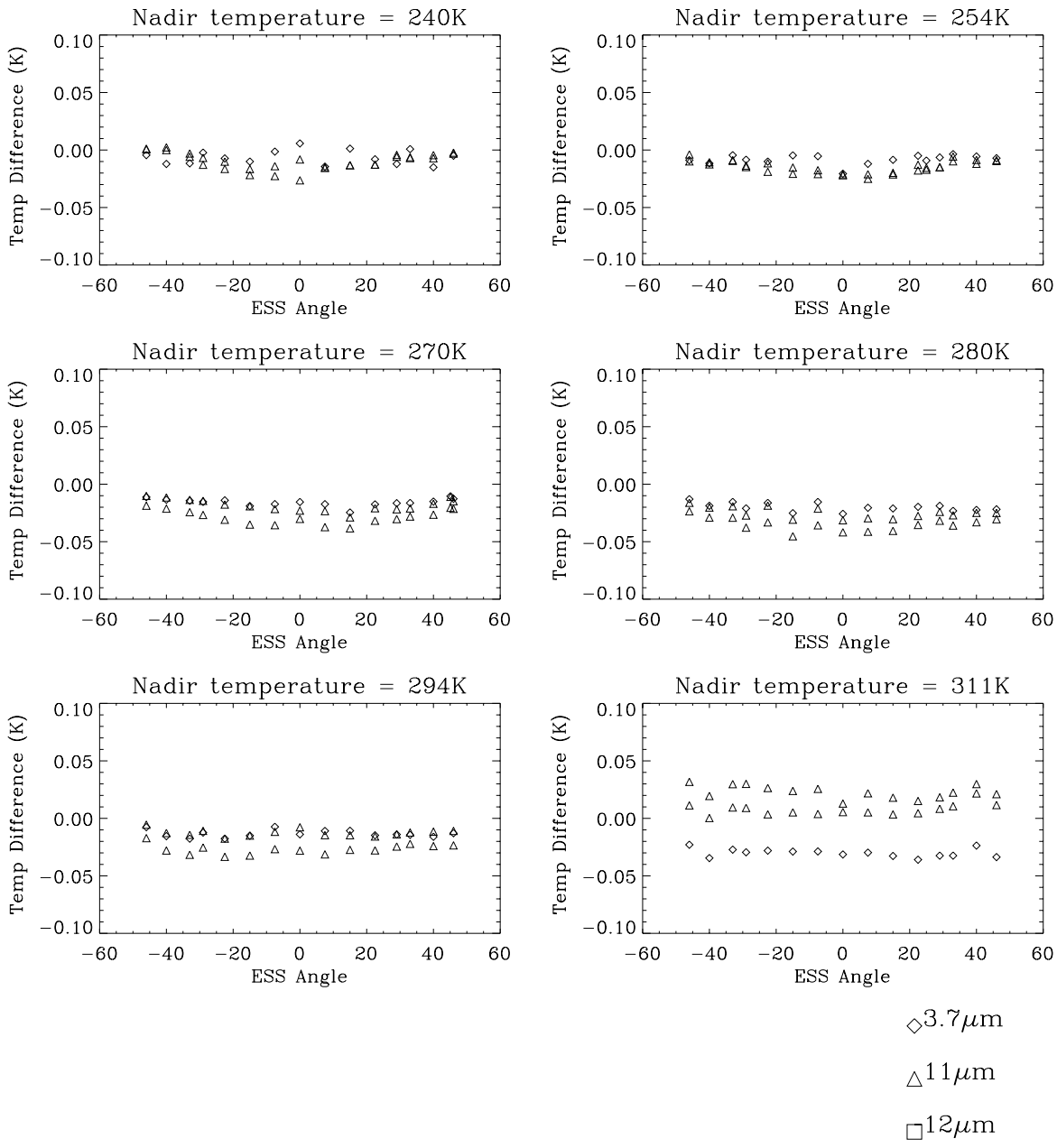

Figure 7.25: Results of radiometric calibration around nadir view at BOL conditions.

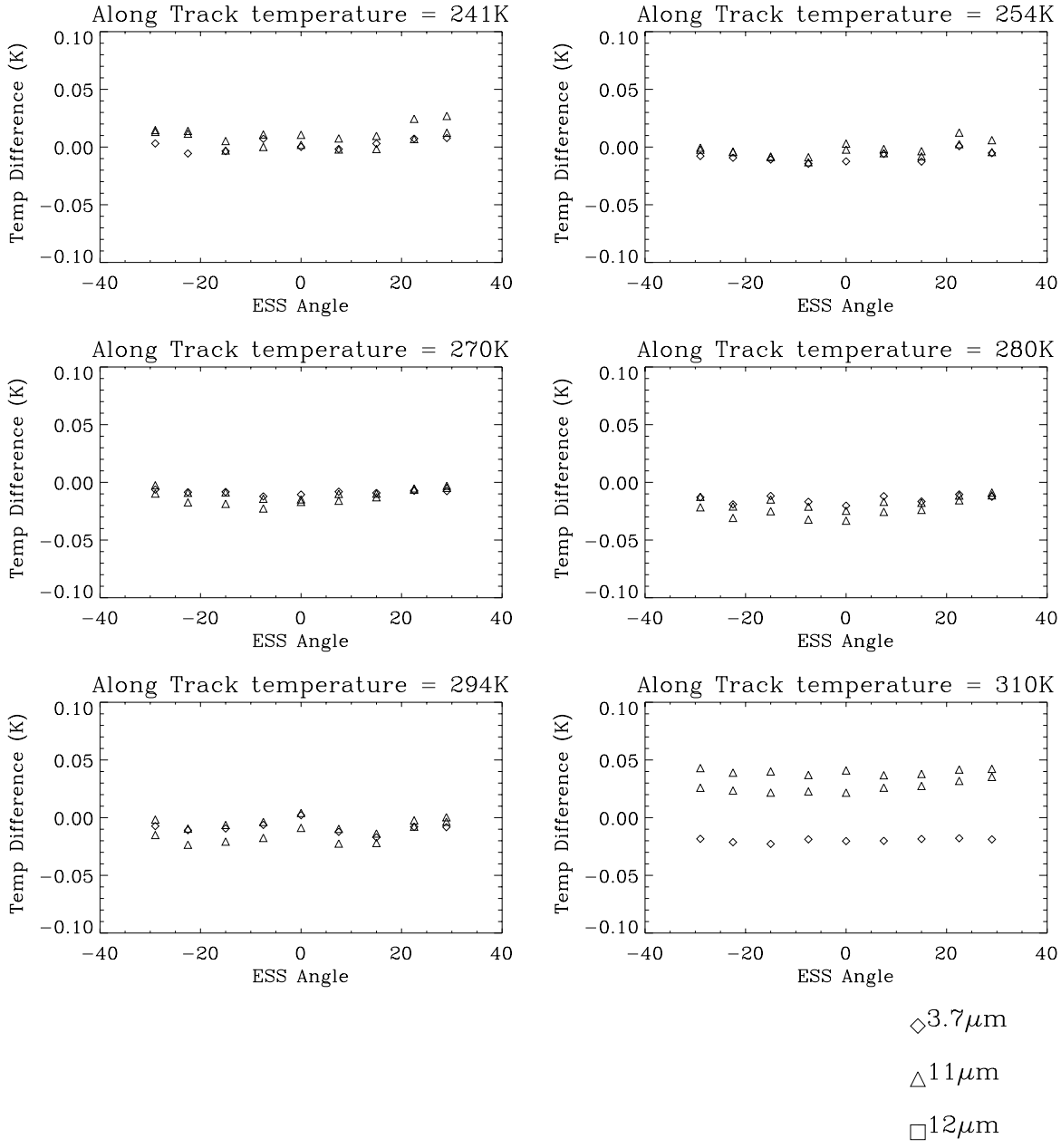

Figure 7.26: Results of radiometric calibration around along-track view at BOL conditions.

7.6 Calibration with Different Black-Body Power Settings

The calibration was verified at BOL conditions with the on-board black bodies at different power levels, in addition to the nominal setting. These were +XBB at low power (Figure 7.30) and high power (Figure 7.29) with the –XBB off, and –XBB at medium (Figure 7.27) and high power (Figure 7.28) with the +XBB off. The results show that the non-linearity correction holds for most blackbody power settings with differences within ±0.05K over the whole temperature range. The differences were not so good at high scene temperatures (>300K) for the case where the +XBB was at low power (T = 278.5). The equivalent tests on ATSR-1 and 2 produced similar results.

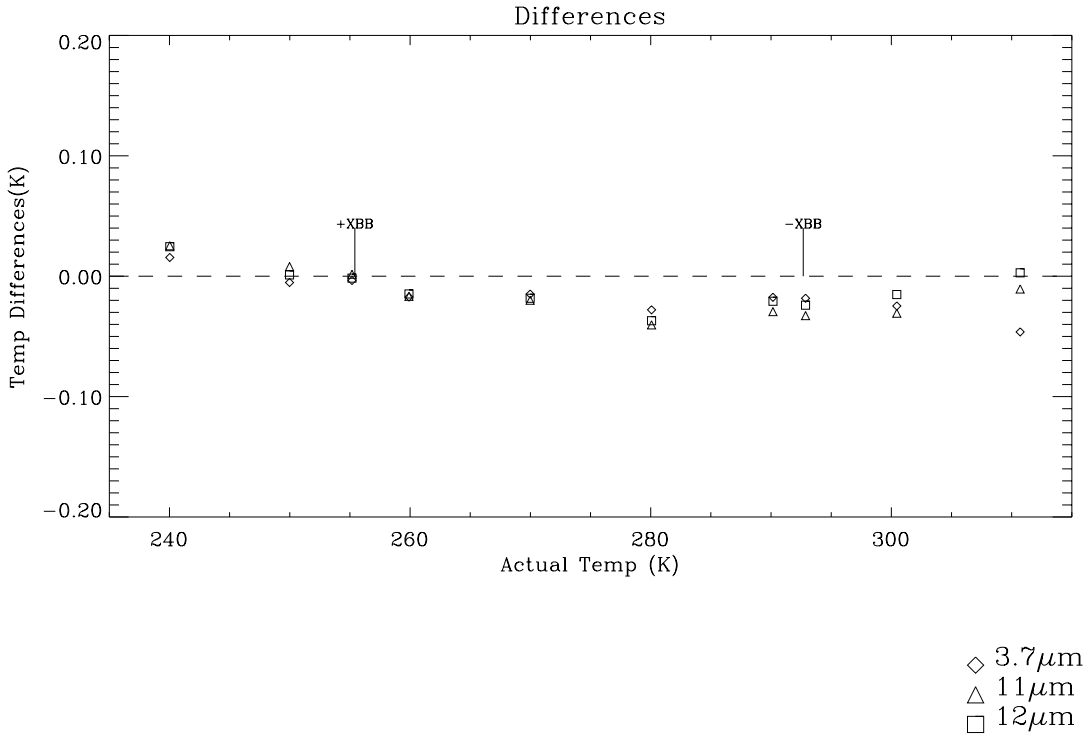

Figure 7.27: Calibration results with the –X black body at medium power (RAD07)

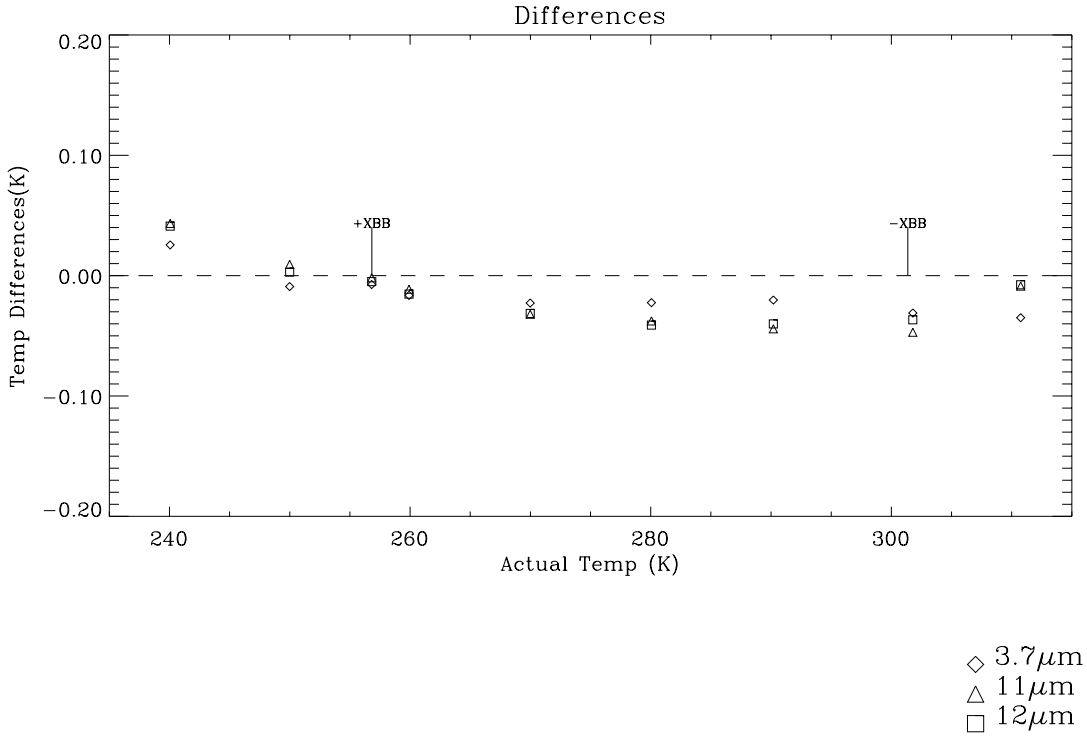

Figure 7.28: Calibration results with the –X black body at high power (RAD08)

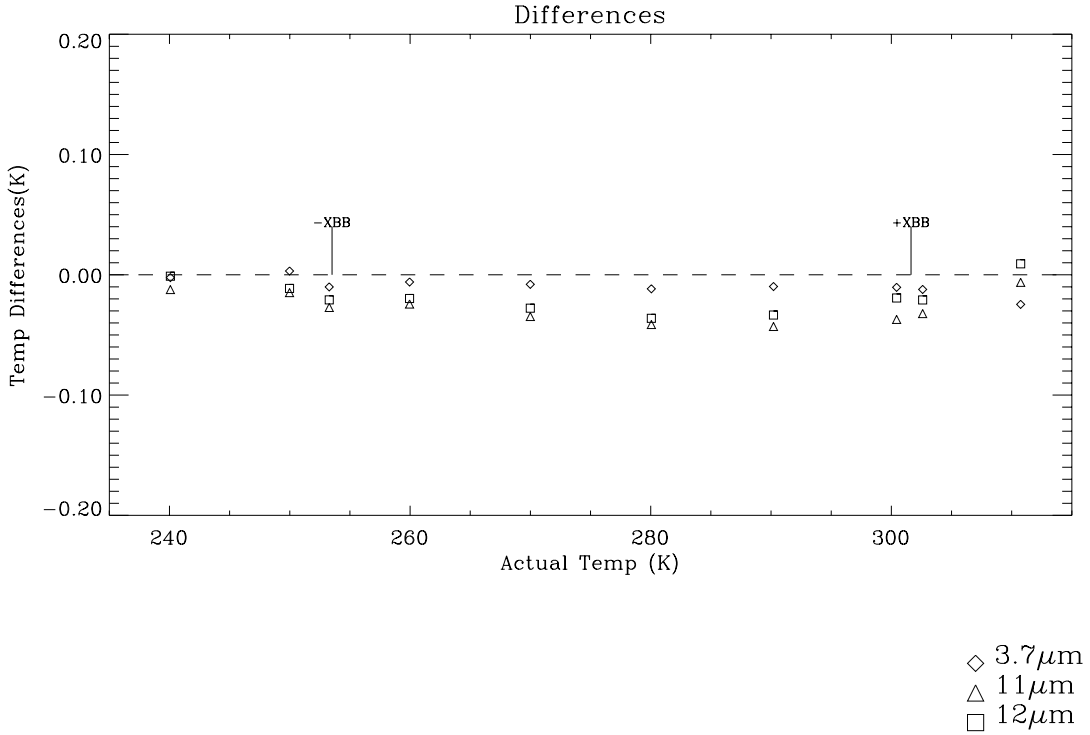

Figure 7.29: Calibration results with the +X black body at high power (RAD09)

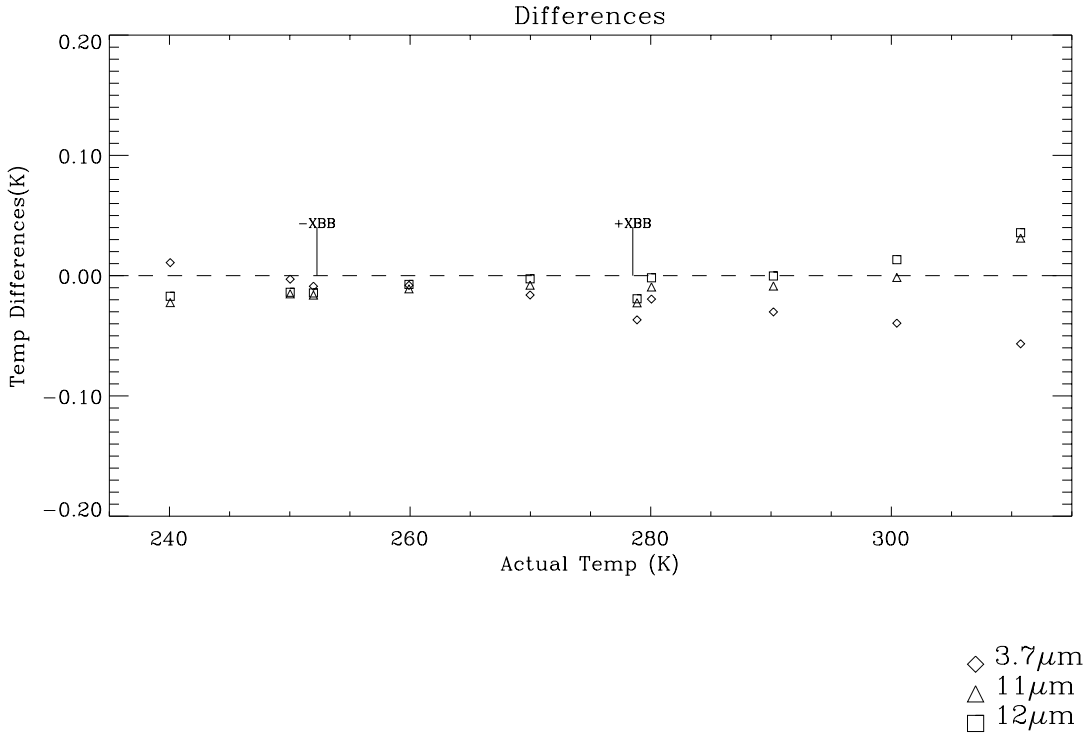

Figure 7.30: Calibration results with the +X black body at low power (RAD10)

7.7 Effect of Thermal Environment

All the calibration measurements described so far have been performed at beginning-of-life thermal conditions, with the FPA at 80K. The non-linearity correction and emissivity corrections have been applied for this particular case. The calculation of the calibration coefficients, a_0 and a_1 depend on the accuracy of the radiance from on-board blackbody, equation 4.8. The reflected component of the scene radiance is related to the paraboloid stop temperature as measured by three precision PRTs. It is assumed that these temperatures are representative of the whole instrument structure. However, the true background radiance may have a significant stray light component that is not related to the paraboloid stop temperature. This is most likely to be earth radiation entering the baffles being reflected off the internal walls of the structure.

To investigate possible radiometric leaks, the calibration was repeated with this instrument under different thermal environments; end-of-life (EOL), BOL conditions with heat loading from ESP raised to 125% of BOL, and heat loading from shroud raised to 125% of BOL. The temperatures of the zones are given in Table 6-1.

The results for each test case FiguresFigure 7.31 to Figure 7.33 do not show any significant differences from the nominal BOL calibration. It can be concluded that the in-flight calibration will not be affected by long-term changes in the environment or instrument temperatures. However, these tests do not cover any long-term deterioration of the surface finishes, which may lead to an increase in radiometric strays.

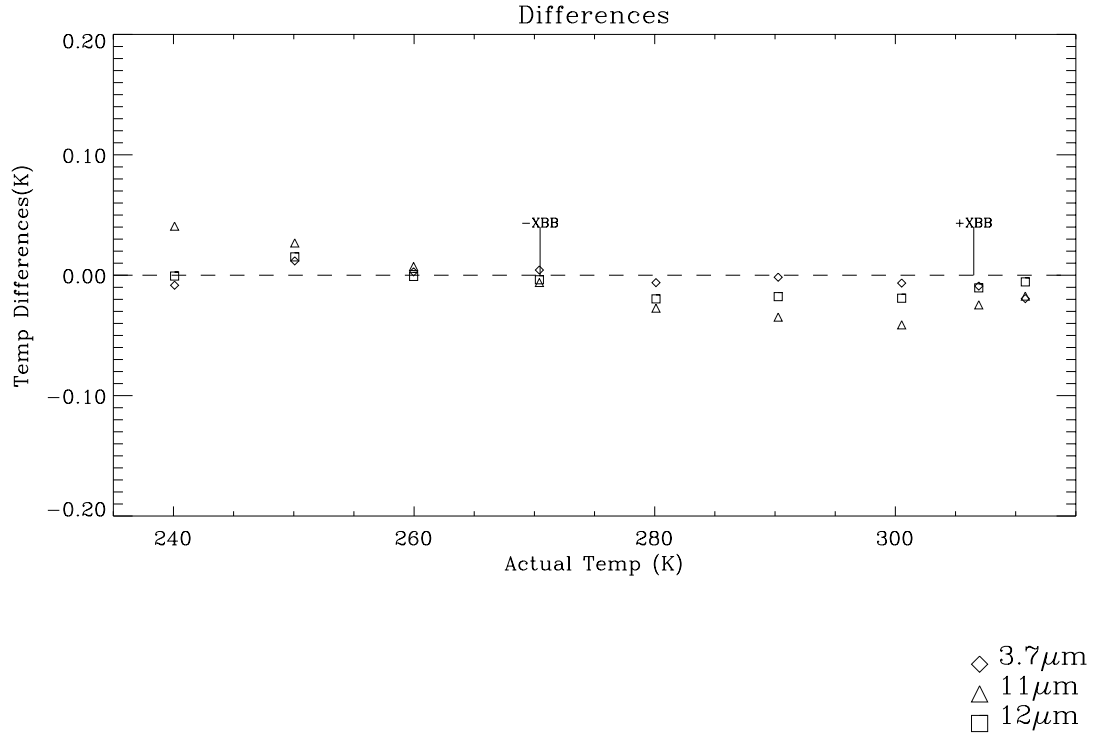

Figure 7.31: Results of radiometric calibration at EOL thermal conditions (RAD11)

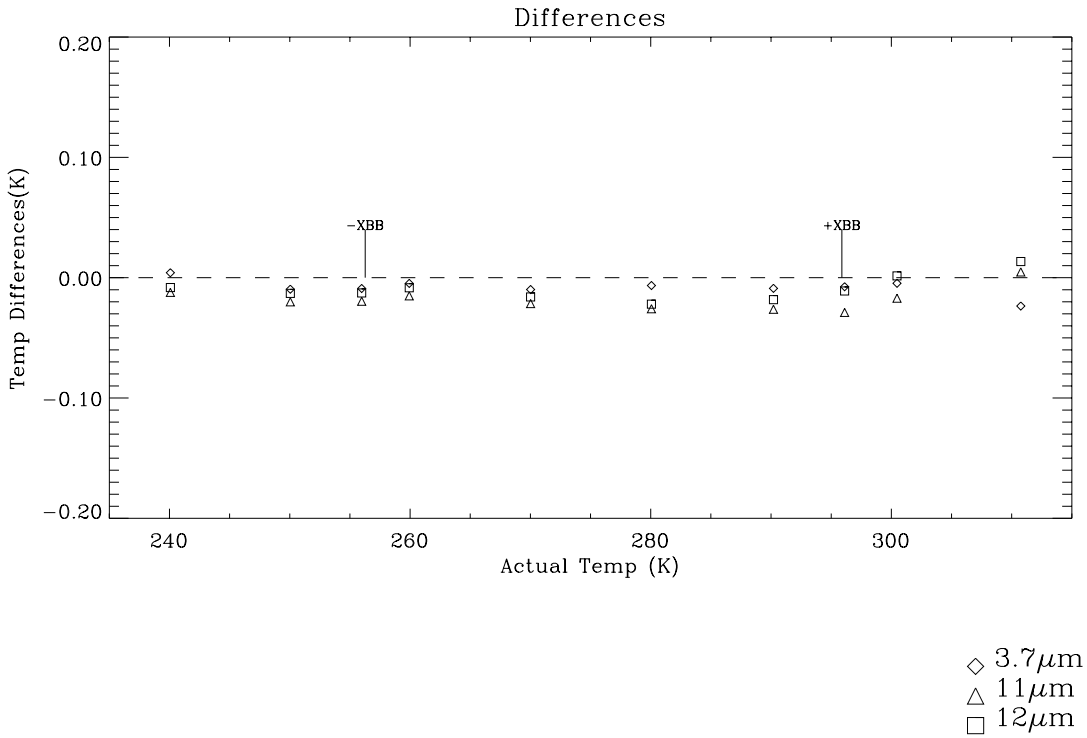

Figure 7.32: Results of calibration with heat loading from shroud increased to 125 % of BOL level (RAD13).

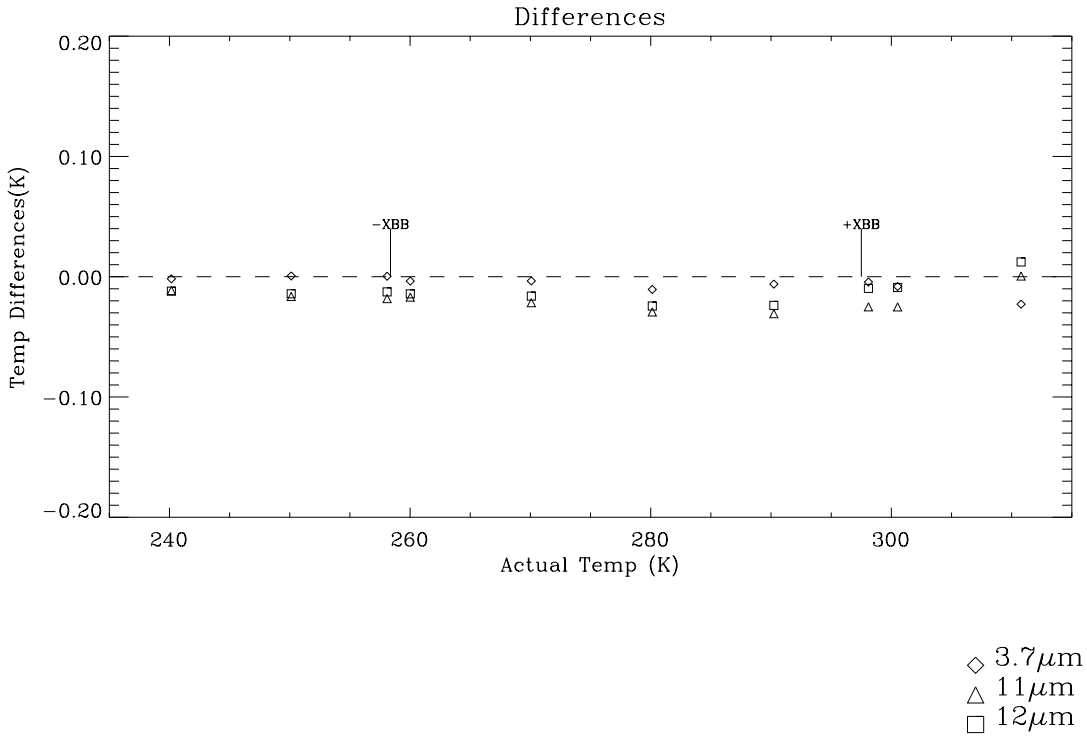

Figure 7.33: Results of calibration with heat loading from ESP increased to 125% of BOL level.

7.8 Orbital Simulations

The primary aim of the orbital simulations was to demonstrate that the radiometric calibration was not affected by the transient thermal fluxes encountered in orbit. Figure 7.34 shows the required temperature profiles of the shrouds and ESP as specified by MMS in AD 6. The ESP was to move from 227K to 293K at a maximum rate of 3.5Kmin^{-1}, and the shrouds from 184K to 284K at a rate of 1Kmin^{-1}. The PSM was maintained at the BOL temperature throughout. The orbital simulation was the last to be performed during the calibration since it presented the greatest risk to the facility.

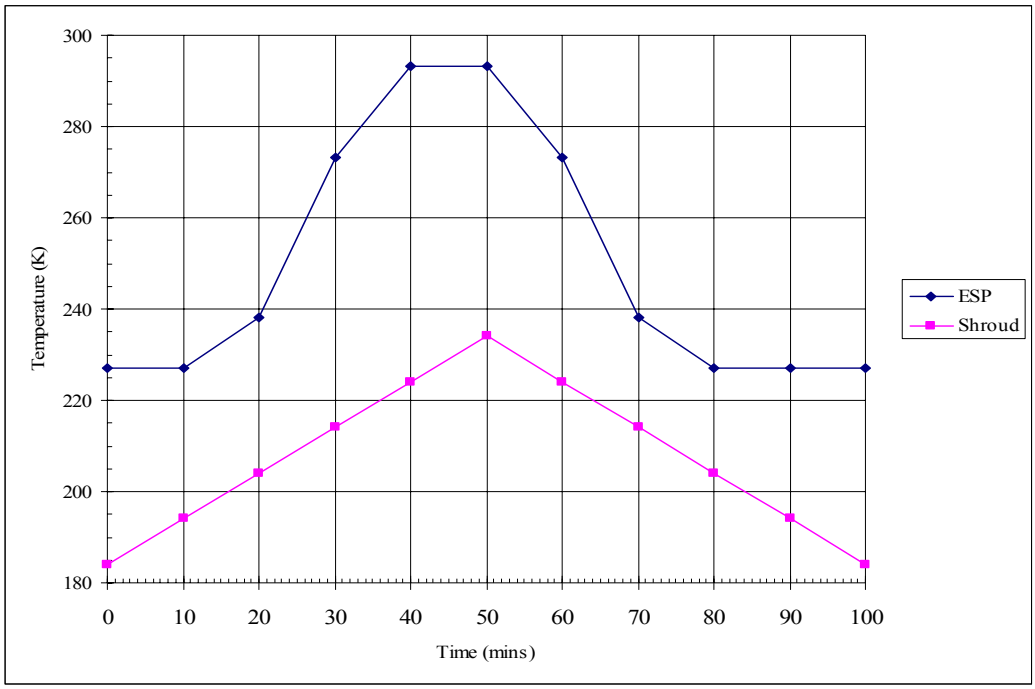

Figure 7.34: Required shroud and ESP temperature profiles for orbital simulation test.

In practice, the planned temperature profile was not achieved, see Figure 7.35, the main problem being the ESP performance. The ESP was controlled by a Huber U390 refrigerator that could be programmed to follow a given temperature profile. Earlier trials with this unit and the ESP had demonstrated that the required temperature profile could be followed. Even during the actual orbital-simulations, the U390 could control the fluid temperature with no difficulty. However, the ESP did not respond as expected to the changes in fluid temperature. Initially it was believed that the problem was caused by an air lock in the system, and several attempts to remove this were tried but with limited success. Given the pressure to complete the test programme (a combination of schedule and very tired team members) the decision was taken to make a best effort attempt at the orbital simulation. The program on the U390 was modified to attempt to get the desired ESP temperature range. The profile in Figure 7.35 shows that the quadrants of the ESP responded differently with large temperature gradients across the whole. Only the along-track baffle tube followed something resembling the required temperature profile. A possible explanation of this behaviour may be an inadequate pump for the fluid circuit, or that water absorbed into the Galden over time affected its pumping properties.

The shroud profiles were somewhat better. Although the temperature gradients on the shrouds were larger than desired, the temperatures at the boundary plates on the instrument followed close to the required profile.

Because of the poor performance of the ESP, the temperature variations in the instrument were not as large as planned.

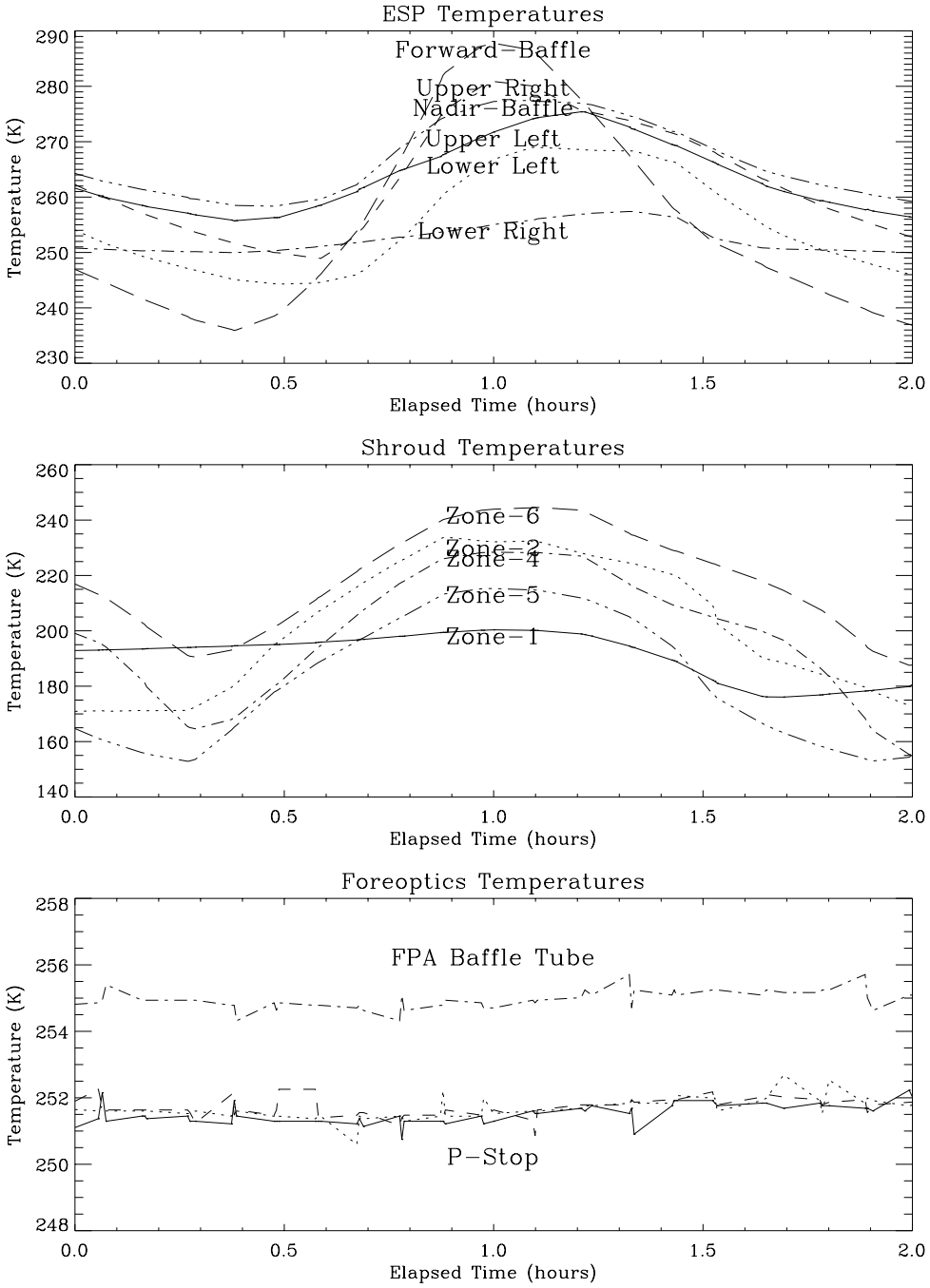

Figure 7.35: Measured ESP, shroud and instrument fore-optics temperatures during the final orbit of orbital simulation test. The temperatures shown for the ESP are the averages for the upper left, upper

right, lower left and lower right quarters, and the nadir and along track baffles. The shroud temperatures are the averages for each zone.

Despite the poor performance of the ESP, the tests proceeded as planned. The along-track black body was maintained at 280K throughout the tests as a reference, and the nadir target set at 240K, 275K and 310K for two orbits at each temperature. When the temperatures of both targets were stable (20mK/5 minutes) radiometric measurements were made. Figure 7.36 shows the differences between the brightness temperatures and actual temperatures of both nadir and along track targets plotted against time. For target temperatures at 275K, 280K and 310K, there are no observable effects on the calibration. For the nadir target at 240K, there is a discernible variation at 3.7μm, but the magnitude is within acceptable levels of ±0.02K.

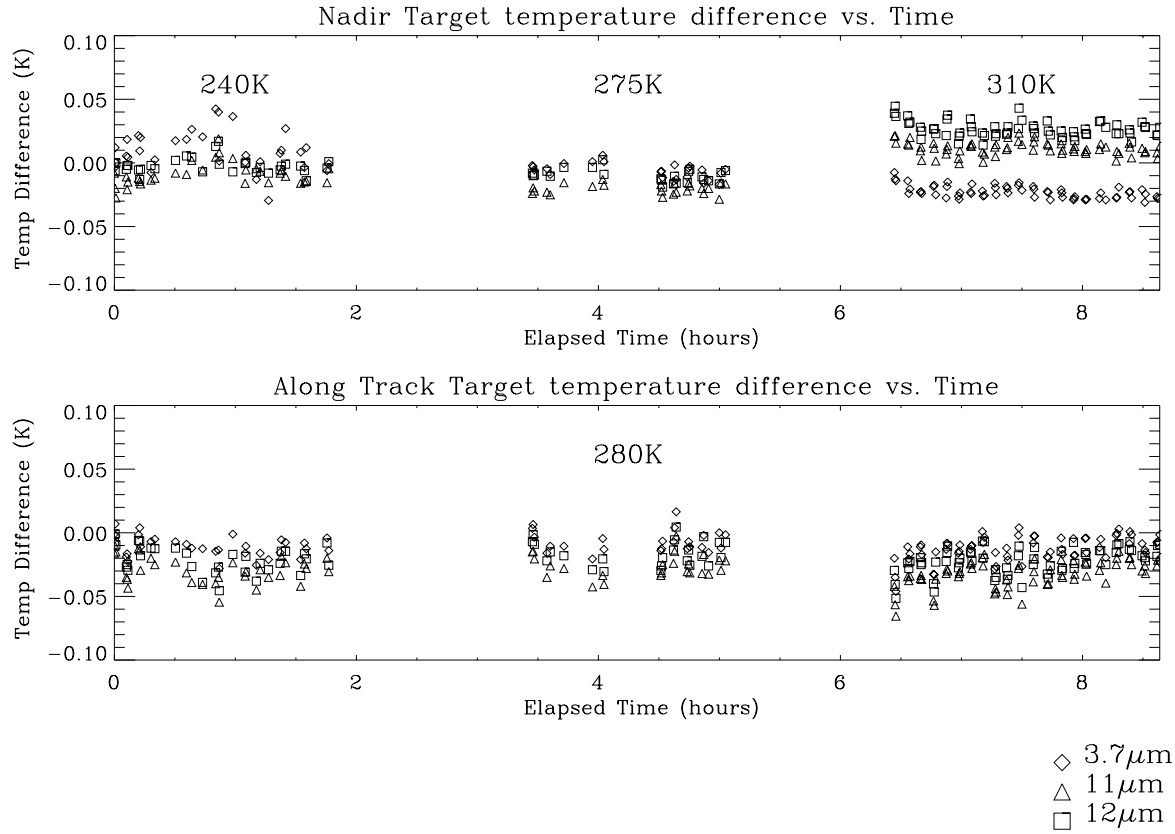

Figure 7.36: Differences between brightness temperature and actual target temperature vs. time for AATSR orbital simulation test.

The measured radiometric noise was within the nominal levels until the end of the final orbit when there was some breakthrough of vibration induced noise, Figure 7.37. This was accompanied by an increase in the vibration levels measured by the accelerometer and slight rise in the SMU body temperature. The noise levels do appear to recover and may have reached the background levels if the tests had continued. However, the decision was taken to conclude the tests as planned so that the instrument could be removed from RAL before Christmas 1998 as agreed.

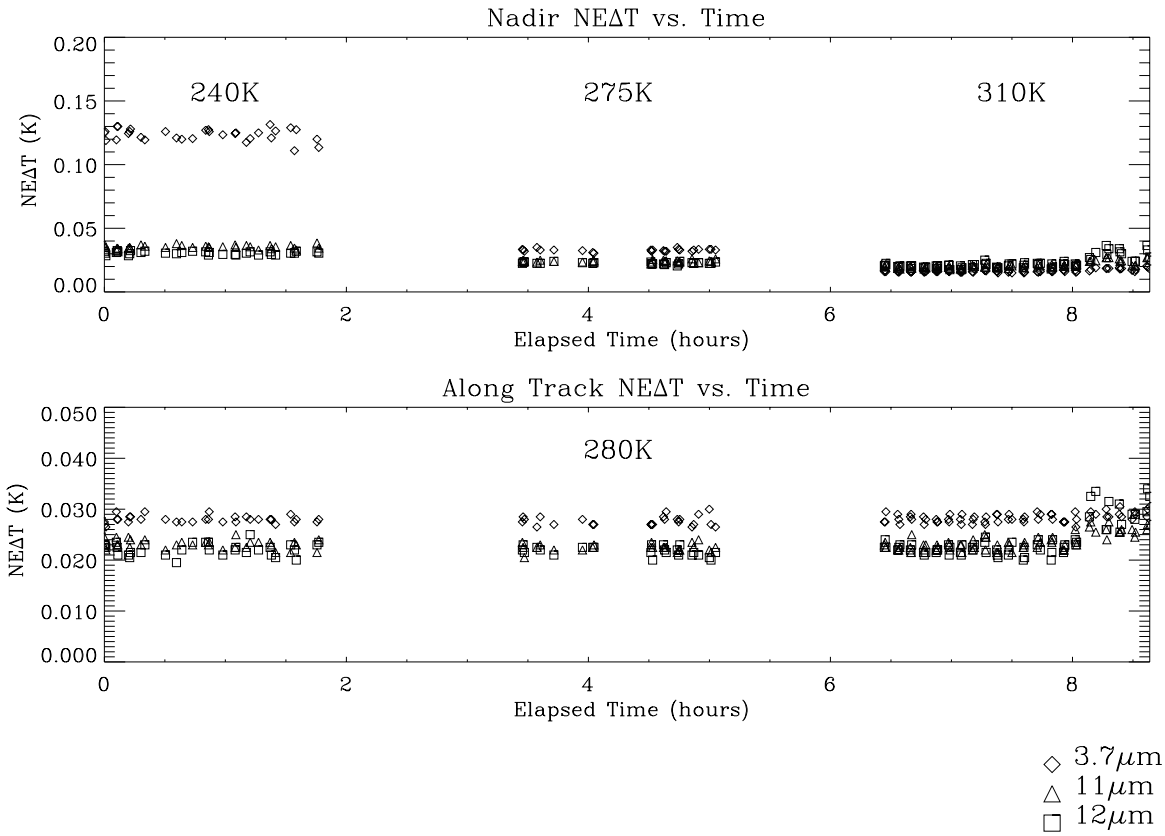

Figure 7.37: NEΔTs for nadir and along-track targets measured during orbital simulation. There is a clear increase in the radiometric noise during the last orbit resulting from increased vibration levels from the scan mechanism.

8 Summary and Conclusions

The calibration of the 3.7µm, 11µm and 12µm channels of the AATSR instrument has been verified against precision blackbody targets having an accuracy of ±0.037K, Table 8-1. The thermometer, resistance and emissivity calibrations of these targets can be traced to international standards, §5.2. In particular the rhodium-iron resistance thermometers have been calibrated against standards traceable to the International Temperature Scale of 1990 (ITS90).

	Nadir	**Along-Track**
Thermometer Calibration	±0.010K	±0.010K
Calibration Drift (Estimated)	±0.010K	±0.010K
Resistance Measurement	±0.010K	±0.010K
Baseplate Gradients	±0.015K	±0.015K
Stability	±0.020K	±0.020K
Emissivity	±0.021K	±0.021K
RMS error	**±0.037K**	**±0.037K**

Table 8-1: Summary of errors in the external blackbody temperatures.

The main radiometric calibration was performed with the instrument operating under beginning-of-life thermal balance conditions, for target temperatures between 210K to 315K, §7.2. The initial results showed that the detectors had non-linear responses similar to those observed on ATSR-2. These data were used to derive non-linearity corrections for the temperature to radiance conversions.

Measurements taken with the external blackbodies matched to the on-board target temperatures revealed an emissivity error at 3.7µm, §7.2.4. It was concluded that the true emissivities of the on-board blackbodies were best represented by calculated values based on reflectance measurements of witness samples.

After applying the corrections, the brightness temperatures at 270K were within 30mK of the of the target temperatures measured by the RIRTs. A summary of the main results is given in Table 8-2.

	3.7µm	**11µm**	**12µm**
T_λ-T_{RIRT}	-0.014K	-0.030K	-0.020K
NEΔT	0.037K	0.025K	0.025K

Table 8-2: The differences between the brightness temperatures measured by AATSR (T_λ) and the external target temperature (T_{RIRT}), and the NEΔT for a target temperature of 270K.

The radiometric noise of the instrument was found to be in specification with no observed breakthrough of microvibration noise, when the scan mechanism was running with nominal vibration levels. However, a signal at ~500Hz was observed in coincidence with increased levels of vibration from the scan mechanism, §7.3. The increase in vibration was probably caused by bearing cage hang-up, a consequence of running the SMU horizontally in 1g for extended periods. Subsequent tests on the mechanism had demonstrated that the vibration

levels did reduce after a short period of running vertically in 1g. It is hoped that the mechanism will run much more smoothly under 0g.

The calibration was also performed at all points around the nadir and along-track swaths, under different thermal environments and different on-board blackbody power settings, §7.5-§7.7. The results showed that there were no significant scan dependent effects or radiometric leaks.

The orbital simulation was the only test that did not finish by having data under the planned conditions. This was due to the poor response of the ESP to changes in the refrigerant temperature. However, the full sequence of orbits was carried out and the results show that the calibration was not affected by the transient thermal environment generated.

A number of outstanding issues need to be addressed:

- At the time of writing, the rhodium-iron resistance thermometers of the external targets have yet to be recalibrated. This will put an upper limit on the blackbody calibration errors due to thermometry drift. The recalibration will take place in mid May 1999.

- The single frequency 'noise' signal at ~500Hz requires further investigation, and in particular its impact on the cloud clearing algorithms, and correlation with scan-mirror telemetry.

- As with ATSR-1 and –2, the 3.7µm channel shows a non-linear radiometric response. Although theories have been proposed, the effect is still not fully explained. Further understanding of its origin would help in a physically meaningful correction to be made.

- The thermal response of the ESP should be investigated with the aim of improving the design of the system for future calibrations.

To conclude: the AATSR 3.7µm, 11µm and 12µm channel meet their performance requirements provided vibration levels from the scan mechanism are nominal. On the condition that this is met, RAL recommends that AATSR's performance is acceptable for flight.

Appendix A Test Plan Summary

Test No	Test Title	Description of Test
RAD01	Radiometric checkout	Set external targets to 280 K and rotate to ends of Nadir and Along track swath. Adjust scan synch offset until inside of instrument and edges of on-board targets are seen. Measure radiometric noise.
RAD02	Black-Body Alignment Test /Radiometric Strays	Keep both external targets constant at 280 K, and cycle the ESS temperature between 245K and 265K. Repeat this for ESS positions α = 0°, ±33° and ±46°. Repeat for target temperature of 240 K.
RAD03	Radiometric Calibration at Centre of Nadir View	Verify calibration in the centre of nadir view over the full external blackbody temperature range from 210 K to 315 K at 5 K intervals, and at the temperatures of the on-board targets. Set along-track target temperature to 280 K.
RAD04	Radiometric Calibration with detectors at 90K	Decrease cooling power of SCC and let FPA temperature rise to ~90 K. When temperatures stabilise, verify calibration in centre of nadir view using reduced set of blackbody temperatures between 240 K and 310 K at 10 K intervals, and at the temperatures of the on-board targets. Set along track-target temperature to 280 K.
RAD05	Calibration around Nadir View	Verify calibration using reduced set of blackbody temperatures between 240 K and 310 K at 20 K intervals around the nadir view (α = 0°, ±7.5°, ±15°, ±22.5°, ±30°, ±33°, ±40°, and ±46°). Along-track target at 280 K.
RAD06	Calibration around Along-Track View	Verify calibration using reduced set of black-body temperatures around the along-track view (α = 0°, ±7.5°, ±15°, ±22.5°, ±30° and ±33). Nadir target at 280 K.
RAD07	Calibration with -XBB at power level 2	Verify calibration in centre of nadir view using reduced set of black-body temperatures for -XBB at power level 2

Test No	Test Title	Description of Test
RAD08	Calibration with -XBB at power level 2	Set -XBB to power level 3. Compare cross over times of temperatures and signal counts. After temperatures have reached steady state, repeat the calibration in centre of nadir view at BOL conditions.
RAD09	Calibration with +XBB at power level 3	Verify calibration in centre of nadir view using reduced set of blackbody temperatures for +XBB at power level 3
RAD10	Calibration with +XBB at power level 1	Verify calibration in centre of nadir view using reduced set of blackbody temperatures for +XBB at power level 1
RAD11	Calibration at End of Life	Verify calibration at centre of nadir view using reduced set of blackbody temperatures for EOL environment.
RAD12	Repeat Calibration at Beginning of Life	Return thermal panels to BOL conditions and set +X blackbody to power level 2. After temperatures have reached steady state, verify calibration in centre of nadir view using reduced set of blackbody temperatures.
RAD13	Calibration with increased heat loading from shrouds	Increase heat loading from cold shrouds to TBD% BOL setting and verify the calibration using the reduced set of blackbody temperatures at the centre of nadir view.
RAD14	Calibration with increased heat loading from Earth Shine Simulator	Return cold shrouds to BOL setting and Increase heat loading from ESS to TBD% BOL setting and verify the calibration using the reduced set of blackbody temperatures at the centre of nadir view.
RAD15	Low Radiance Calibration	Cool the along-track blackbody with LN_2 and perform low radiance measurements. When completed refill target with refrigerant.
RAD16	Repeat Along-Track Calibration	Verify calibration in centre of along-track view using reduced set of target temperatures.
RAD17	SMU Backup Test	Perform calibration measurements with SMU in backup mode.
ORB	Orbital simulations	

Test No	Test Title	Description of Test
ORB01		Initial 'run-in' orbit with nadir target set to 240 K and along-track target at 280 K
ORB02	Orbit with target at 240 K	Cold BB orbit. Nadir target at 240 K, along-track target at 280 K
ORB03		BB transition orbit. Nadir target set to 275 K, along-track target at 280 K
ORB04	Orbit with target at 275 K	Medium BB orbit. Nadir target at 275 K, along-track target at 280 K
ORB05		BB transition orbit. Nadir target set to 310 K, along-track target at 280 K
ORB06	Orbit with target at 280 K	Hot BB orbit. Nadir target at 310 K, along-track target at 280 K

Appendix B Infra-Red Channel Spectral Responses

3.7μm Spectral Response

Wavelength μm	Response	Wavelength μm	Response	Wavelength μm	Response
3.004028	0.00022	3.329851	0.00173	3.655674	0.99113
3.010294	0.00021	3.336117	0.00174	3.661940	0.99874
3.016560	0.00020	3.342383	0.00196	3.668206	0.98786
3.022826	0.00021	3.348649	0.00208	3.674472	1.00000
3.029091	0.00020	3.354915	0.00253	3.680738	0.98504
3.035357	0.00021	3.361180	0.00279	3.687004	0.97957
3.041623	0.00022	3.367446	0.00306	3.693269	0.98273
3.047889	0.00021	3.373712	0.00348	3.699535	0.97102
3.054155	0.00020	3.379978	0.00410	3.705801	0.96079
3.060421	0.00022	3.386244	0.00449	3.712067	0.95627
3.066686	0.00021	3.392510	0.00550	3.718333	0.93970
3.072952	0.00021	3.398775	0.00610	3.724599	0.94372
3.079218	0.00020	3.405041	0.00722	3.730864	0.93264
3.085484	0.00021	3.411307	0.00842	3.737130	0.92721
3.091750	0.00020	3.417573	0.00973	3.743396	0.91509
3.098016	0.00021	3.423839	0.01140	3.749662	0.91689
3.104281	0.00021	3.430105	0.01326	3.755928	0.89270
3.110547	0.00021	3.436370	0.01546	3.762194	0.87921
3.116813	0.00022	3.442636	0.01793	3.768459	0.85699
3.123079	0.00021	3.448902	0.02064	3.774725	0.84625
3.129345	0.00021	3.455168	0.02382	3.780991	0.85507
3.135611	0.00021	3.461434	0.02771	3.787257	0.83950
3.141876	0.00019	3.467700	0.03191	3.793523	0.82917
3.148142	0.00020	3.473965	0.03656	3.799789	0.83680
3.154408	0.00019	3.480231	0.04290	3.806054	0.83610
3.160674	0.00020	3.486497	0.05061	3.812320	0.84533
3.166940	0.00019	3.492763	0.06062	3.818586	0.82603
3.173206	0.00019	3.499029	0.06983	3.824852	0.83561
3.179471	0.00019	3.505295	0.08275	3.831118	0.83913
3.185737	0.00020	3.511560	0.09862	3.837384	0.83636
3.192003	0.00020	3.517826	0.11670	3.843649	0.83433
3.198269	0.00018	3.524092	0.14003	3.849915	0.82677
3.204535	0.00019	3.530358	0.16720	3.856181	0.82148
3.210801	0.00019	3.536624	0.20011	3.862447	0.80807
3.217066	0.00018	3.542890	0.24276	3.868713	0.79154
3.223332	0.00021	3.549155	0.28381	3.874979	0.76898
3.229598	0.00019	3.555421	0.34668	3.881244	0.75075
3.235864	0.00019	3.561687	0.40636	3.887510	0.71812
3.242130	0.00022	3.567953	0.46877	3.893776	0.68368
3.248396	0.00024	3.574219	0.54005	3.900042	0.64247
3.254661	0.00033	3.580485	0.61101	3.906308	0.59829
3.260927	0.00040	3.586750	0.67248	3.912574	0.54253
3.267193	0.00044	3.593016	0.73196	3.918839	0.50487
3.273459	0.00047	3.599282	0.80359	3.925105	0.45169
3.279725	0.00045	3.605548	0.86288	3.931371	0.39117
3.285991	0.00057	3.611814	0.90212	3.937637	0.33781
3.292256	0.00079	3.618080	0.93979	3.943903	0.29397
3.298522	0.00106	3.624345	0.96513	3.950169	0.25279
3.304788	0.00129	3.630611	0.97725	3.956434	0.21634
3.311054	0.00134	3.636877	0.97404	3.962700	0.18002
3.317320	0.00143	3.643143	0.98577	3.968966	0.15161
3.323586	0.00152	3.649409	0.99517	3.975232	0.13114

Wavelength µm	Response
3.981498	0.11007
3.987763	0.09147
3.994029	0.07692
4.000295	0.06736
4.006561	0.05668
4.012827	0.04857
4.019093	0.04287
4.025358	0.03642
4.031624	0.03209
4.037890	0.02733
4.044156	0.02427
4.050422	0.02161
4.056688	0.01868
4.062953	0.01650
4.069219	0.01474
4.075485	0.01313
4.081751	0.01153
4.088017	0.01026
4.094283	0.00924
4.100548	0.00830
4.106814	0.00757
4.113080	0.00683
4.119346	0.00612
4.125612	0.00557
4.131878	0.00511
4.138143	0.00464
4.144409	0.00434
4.150675	0.00378
4.156941	0.00351
4.163207	0.00343
4.169473	0.00331
4.175738	0.00308
4.182004	0.00290
4.188270	0.00287
4.194536	0.00274
4.200802	0.00255
4.207068	0.00218
4.213333	0.00178
4.219599	0.00148
4.225865	0.00151
4.232131	0.00124
4.238397	0.00110
4.244663	0.00135
4.250928	0.00137
4.257194	0.00150
4.263460	0.00140
4.269726	0.00110
4.275992	0.00089
4.282257	0.00077
4.288523	0.00070
4.294789	0.00058
4.301055	0.00061
4.307321	0.00065
4.313587	0.00062
4.319852	0.00080
4.326118	0.00087
4.332384	0.00082
4.338650	0.00085
4.344916	0.00077
4.351182	0.00075
4.357447	0.00070
4.363713	0.00063
4.369979	0.00057
4.376245	0.00051
4.382511	0.00040
4.388777	0.00027
4.395042	0.00018
4.401308	0.00015
4.407574	0.00017
4.413840	0.00017
4.420106	0.00017
4.426372	0.00016
4.432637	0.00015
4.438903	0.00012
4.445169	0.00012
4.451435	0.00009
4.457701	0.00007
4.463967	0.00006
4.470232	0.00003
4.476498	0.00001
4.482764	0.00000
4.489030	0.00000
4.495296	0.00000
4.501562	0.00000
4.507827	0.00000
4.514093	0.00000
4.520359	0.00001
4.526625	0.00001
4.532891	0.00001
4.539157	0.00001
4.545422	0.00001
4.551688	0.00002
4.557954	0.00002
4.564220	0.00002
4.570486	0.00002
4.576751	0.00001
4.583017	0.00002
4.589283	0.00002
4.595549	0.00002

11μm Spectral Response

Wavelength μm	Response	Wavelength μm	Response	Wavelength μm	Response
9.820094	0.00000	10.338491	0.13601	10.856888	0.87220
9.829351	0.00003	10.347748	0.15133	10.866145	0.88004
9.838608	0.00007	10.357005	0.17092	10.875402	0.89280
9.847865	0.00001	10.366262	0.18723	10.884659	0.90071
9.857122	0.00009	10.375519	0.21139	10.893916	0.90773
9.866379	0.00010	10.384776	0.23325	10.903173	0.93778
9.875636	0.00010	10.394033	0.26187	10.912431	0.94001
9.884894	0.00014	10.403291	0.28796	10.921688	0.94587
9.894151	0.00017	10.412548	0.32007	10.930945	0.94865
9.903408	0.00016	10.421805	0.34471	10.940202	0.96415
9.912665	0.00023	10.431062	0.37121	10.949459	0.93905
9.921922	0.00027	10.440319	0.39455	10.958716	0.94999
9.931179	0.00027	10.449576	0.42635	10.967973	0.96369
9.940436	0.00031	10.458833	0.45801	10.977230	0.96648
9.949693	0.00036	10.468090	0.48507	10.986487	0.99133
9.958950	0.00042	10.477347	0.52265	10.995744	0.99808
9.968207	0.00053	10.486604	0.54747	11.005001	0.98830
9.977464	0.00062	10.495861	0.58349	11.014259	0.97380
9.986722	0.00073	10.505119	0.58947	11.023516	1.00000
9.995979	0.00082	10.514376	0.61330	11.032773	0.97816
10.005236	0.00089	10.523633	0.63098	11.042030	0.99398
10.014493	0.00104	10.532890	0.64208	11.051287	0.97267
10.023750	0.00127	10.542147	0.65732	11.060544	0.96696
10.033007	0.00142	10.551404	0.67813	11.069801	0.95023
10.042264	0.00167	10.560661	0.67675	11.079058	0.92800
10.051521	0.00195	10.569918	0.69213	11.088315	0.91838
10.060778	0.00221	10.579175	0.70338	11.097572	0.90960
10.070035	0.00260	10.588432	0.71467	11.106829	0.88030
10.079292	0.00296	10.597689	0.71886	11.116087	0.87993
10.088550	0.00346	10.606947	0.71532	11.125344	0.83430
10.097807	0.00404	10.616204	0.72179	11.134601	0.80510
10.107064	0.00468	10.625461	0.74028	11.143858	0.78137
10.116321	0.00535	10.634718	0.75550	11.153115	0.74665
10.125578	0.00610	10.643975	0.76027	11.162372	0.70124
10.134835	0.00724	10.653232	0.76256	11.171629	0.68094
10.144092	0.00818	10.662489	0.76078	11.180886	0.62875
10.153349	0.00932	10.671746	0.74976	11.190143	0.59834
10.162606	0.01071	10.681003	0.76073	11.199400	0.53718
10.171863	0.01207	10.690260	0.77329	11.208657	0.50567
10.181120	0.01396	10.699517	0.79395	11.217915	0.47863
10.190378	0.01606	10.708775	0.78467	11.227172	0.42706
10.199635	0.01873	10.718032	0.79392	11.236429	0.39081
10.208892	0.02166	10.727289	0.80661	11.245686	0.35871
10.218149	0.02456	10.736546	0.80700	11.254943	0.33286
10.227406	0.02796	10.745803	0.80241	11.264200	0.29806
10.236663	0.03255	10.755060	0.79070	11.273457	0.27472
10.245920	0.03693	10.764317	0.82593	11.282714	0.24682
10.255177	0.04201	10.773574	0.79317	11.291971	0.22329
10.264434	0.04786	10.782831	0.83245	11.301228	0.20708
10.273691	0.05474	10.792088	0.83683	11.310485	0.18628
10.282948	0.06281	10.801345	0.84147	11.319742	0.16944
10.292206	0.07164	10.810603	0.85634	11.329000	0.15244
10.301463	0.08190	10.819860	0.86205	11.338257	0.14110
10.310720	0.09230	10.829117	0.84793	11.347514	0.12614
10.319977	0.10418	10.838374	0.87298	11.356771	0.11695
10.329234	0.11973	10.847631	0.89096	11.366028	0.10202

Wavelength µm	Response	Wavelength µm	Response	Wavelength µm	Response
11.375285	0.09094	11.643741	0.00541	11.912196	0.00105
11.384542	0.08514	11.652998	0.00499	11.921453	0.00100
11.393799	0.07405	11.662255	0.00464	11.930710	0.00085
11.403056	0.07195	11.671512	0.00436	11.939968	0.00097
11.412313	0.06139	11.680769	0.00401	11.949225	0.00083
11.421570	0.05561	11.690026	0.00355	11.958482	0.00086
11.430828	0.04998	11.699283	0.00354	11.967739	0.00079
11.440085	0.04581	11.708540	0.00316	11.976996	0.00084
11.449342	0.04250	11.717797	0.00302	11.986253	0.00074
11.458599	0.03752	11.727054	0.00263	11.995510	0.00077
11.467856	0.03453	11.736312	0.00240	12.004767	0.00074
11.477113	0.03172	11.745569	0.00232	12.014024	0.00069
11.486370	0.02870	11.754826	0.00220	12.023281	0.00064
11.495627	0.02525	11.764083	0.00210	12.032538	0.00052
11.504884	0.02359	11.773340	0.00209	12.041796	0.00066
11.514141	0.02076	11.782597	0.00186	12.051053	0.00062
11.523398	0.01907	11.791854	0.00185	12.060310	0.00072
11.532656	0.01845	11.801111	0.00154	12.069567	0.00050
11.541913	0.01581	11.810368	0.00151	12.078824	0.00050
11.551170	0.01411	11.819625	0.00156	12.088081	0.00047
11.560427	0.01285	11.828882	0.00152	12.097338	0.00066
11.569684	0.01207	11.838140	0.00135	12.106595	0.00055
11.578941	0.01097	11.847397	0.00143	12.115852	0.00077
11.588198	0.00966	11.856654	0.00134	12.125109	0.00066
11.597455	0.00871	11.865911	0.00137	12.134366	0.00064
11.606712	0.00797	11.875168	0.00117	12.143624	0.00057
11.615969	0.00775	11.884425	0.00109	12.152881	0.00048
11.625226	0.00672	11.893682	0.00097	12.162138	0.00044
11.634484	0.00618	11.902939	0.00110	12.171395	0.00071

12μm Spectral Response

Wavelength μm	Response	Wavelength μm	Response	Wavelength μm	Response
11.023855	0.00000	11.546173	0.39727	12.068490	0.83927
11.033182	0.00005	11.555500	0.43552	12.077817	0.92570
11.042509	0.00010	11.564827	0.47296	12.087144	0.89569
11.051836	0.00013	11.574154	0.49639	12.096471	0.86865
11.061163	0.00015	11.583481	0.52745	12.105799	0.88067
11.070490	0.00011	11.592808	0.55012	12.115126	0.91540
11.079818	0.00023	11.602135	0.57532	12.124453	0.91474
11.089145	0.00044	11.611462	0.60537	12.133780	0.93118
11.098472	0.00058	11.620789	0.64470	12.143107	0.89670
11.107799	0.00083	11.630116	0.66433	12.152434	0.93849
11.117126	0.00117	11.639444	0.69644	12.161761	0.89968
11.126453	0.00157	11.648771	0.70706	12.171088	0.87399
11.135780	0.00218	11.658098	0.75627	12.180415	0.95690
11.145107	0.00306	11.667425	0.84552	12.189742	0.99941
11.154434	0.00383	11.676752	0.84775	12.199070	0.96435
11.163761	0.00479	11.686079	0.80343	12.208397	0.86423
11.173089	0.00604	11.695406	0.85302	12.217724	1.00000
11.182416	0.00772	11.704733	0.87390	12.227051	0.91557
11.191743	0.00936	11.714060	0.85701	12.236378	0.94900
11.201070	0.01167	11.723387	0.90228	12.245705	0.93172
11.210397	0.01421	11.732715	0.90525	12.255032	0.95291
11.219724	0.01616	11.742042	0.90884	12.264359	0.95388
11.229051	0.01929	11.751369	0.92916	12.273686	0.99468
11.238378	0.02317	11.760696	0.95661	12.283013	0.88151
11.247705	0.02571	11.770023	0.94340	12.292341	0.98603
11.257032	0.02977	11.779350	0.99863	12.301668	0.86244
11.266360	0.03359	11.788677	0.98577	12.310995	0.89999
11.275687	0.03703	11.798004	0.93741	12.320322	0.91813
11.285014	0.04212	11.807331	0.93180	12.329649	0.90372
11.294341	0.04783	11.816658	0.93541	12.338976	0.87760
11.303668	0.05337	11.825986	0.95493	12.348303	0.86870
11.312995	0.05817	11.835313	0.94366	12.357630	0.86445
11.322322	0.06324	11.844640	0.89969	12.366957	0.82220
11.331649	0.07084	11.853967	0.93047	12.376284	0.83785
11.340976	0.07690	11.863294	0.94853	12.385612	0.80269
11.350303	0.08341	11.872621	0.94952	12.394939	0.77462
11.359631	0.09132	11.881948	0.90322	12.404266	0.71862
11.368958	0.09981	11.891275	0.89247	12.413593	0.74697
11.378285	0.10808	11.900602	0.92398	12.422920	0.71044
11.387612	0.11901	11.909929	0.91428	12.432247	0.67130
11.396939	0.12728	11.919257	0.89727	12.441574	0.66259
11.406266	0.14115	11.928584	0.90053	12.450901	0.60768
11.415593	0.15177	11.937911	0.91938	12.460228	0.57584
11.424920	0.16208	11.947238	0.90899	12.469555	0.56037
11.434247	0.17395	11.956565	0.90738	12.478883	0.54150
11.443574	0.19186	11.965892	0.89388	12.488210	0.47689
11.452902	0.20483	11.975219	0.91193	12.497537	0.50569
11.462229	0.21745	11.984546	0.87766	12.506864	0.47015
11.471556	0.24027	11.993873	0.90069	12.516191	0.42380
11.480883	0.25940	12.003200	0.87824	12.525518	0.42528
11.490210	0.27394	12.012528	0.89732	12.534845	0.41850
11.499537	0.29087	12.021855	0.89851	12.544172	0.37703
11.508864	0.31268	12.031182	0.90728	12.553499	0.36005
11.518191	0.34010	12.040509	0.90034	12.562826	0.33102
11.527518	0.36351	12.049836	0.89415	12.572154	0.30819
11.536845	0.38524	12.059163	0.88452	12.581481	0.29893

Wavelength µm	Response
12.590808	0.29149
12.600135	0.24750
12.609462	0.26266
12.618789	0.23964
12.628116	0.22905
12.637443	0.22298
12.646770	0.19598
12.656097	0.18589
12.665425	0.17299
12.674752	0.16377
12.684079	0.15945
12.693406	0.15247
12.702733	0.14793
12.712060	0.13586
12.721387	0.13236
12.730714	0.11615
12.740041	0.10819
12.749368	0.10673
12.758696	0.09624
12.768023	0.09048
12.777350	0.08737
12.786677	0.08318
12.796004	0.07976
12.805331	0.07120
12.814658	0.06416
12.823985	0.06313
12.833312	0.06368
12.842639	0.05518
12.851967	0.05150

Wavelength µm	Response
12.861294	0.04984
12.870621	0.04434
12.879948	0.04511
12.889275	0.04292
12.898602	0.03744
12.907929	0.03677
12.917256	0.03506
12.926583	0.03157
12.935910	0.03167
12.945238	0.02877
12.954565	0.02596
12.963892	0.02618
12.973219	0.02283
12.982546	0.02232
12.991873	0.02276
13.001200	0.02058
13.010527	0.01894
13.019854	0.01776
13.029181	0.01723
13.038509	0.01651
13.047836	0.01634
13.057163	0.01596
13.066490	0.01457
13.075817	0.01461
13.085144	0.01461
13.094471	0.01323
13.103798	0.01157
13.113125	0.01198
13.122452	0.01199

Wavelength µm	Response
13.131780	0.01051
13.141107	0.00996
13.150434	0.01056
13.159761	0.01079
13.169088	0.00891
13.178415	0.00925
13.187742	0.00921
13.197069	0.00891
13.206396	0.00815
13.215723	0.00771
13.225051	0.00674
13.234378	0.00663
13.243705	0.00688
13.253032	0.00589
13.262359	0.00686
13.271686	0.00619
13.281013	0.00561
13.290340	0.00582
13.299667	0.00543
13.308994	0.00531
13.318322	0.00562
13.327649	0.00538
13.336976	0.00483
13.346303	0.00510
13.355630	0.00489
13.364957	0.00490
13.374284	0.00456
13.383611	0.00402
13.392938	0.00451

Appendix C Temperature to Radiance Lookup Tables

3.7μm Temperature/Radiance Lookup Table

Polynomial fall off coefficients:
z0 = 1.00020E+00
z1 = -4.90471E-02
z2 = 1.40402E-02

Temperature (K)	Radiance (W cm^{-2} sr^{-1}) Uncorrected	Corrected
77	2.907007E-21	2.907588E-21
78	5.358177E-21	5.359249E-21
79	9.729656E-21	9.731602E-21
80	1.741477E-20	1.741825E-20
81	3.073956E-20	3.074571E-20
82	5.353620E-20	5.354691E-20
83	9.203823E-20	9.205664E-20
84	1.562614E-19	1.562927E-19
85	2.621089E-19	2.621613E-19
86	4.345440E-19	4.346309E-19
87	7.123217E-19	7.124642E-19
88	1.154968E-18	1.155199E-18
89	1.852973E-18	1.853343E-18
90	2.942534E-18	2.943122E-18
91	4.626671E-18	4.627597E-18
92	7.205206E-18	7.206647E-18
93	1.111693E-17	1.111915E-17
94	1.699844E-17	1.700184E-17
95	2.576552E-17	2.577068E-17
96	3.872483E-17	3.873258E-17
97	5.772600E-17	5.773754E-17
98	8.536718E-17	8.538426E-17
99	1.252709E-16	1.252959E-16
100	1.824514E-16	1.824879E-16
101	2.638012E-16	2.638540E-16
102	3.787299E-16	3.788056E-16
103	5.399991E-16	5.401071E-16
104	7.648062E-16	7.649592E-16
105	1.076182E-15	1.076398E-15
106	1.504785E-15	1.505086E-15
107	2.091185E-15	2.091603E-15
108	2.888767E-15	2.889345E-15
109	3.967388E-15	3.968182E-15
110	5.417968E-15	5.419051E-15
111	7.358222E-15	7.359693E-15
112	9.939784E-15	9.941772E-15
113	1.335701E-14	1.335968E-14
114	1.785783E-14	1.786140E-14
115	2.375701E-14	2.376176E-14
116	3.145236E-14	3.145865E-14
117	4.144440E-14	4.145269E-14
118	5.436018E-14	5.437105E-14

Temperature (K)	Radiance (W cm^{-2} sr^{-1}) Uncorrected	Corrected
119	7.098194E-14	7.099614E-14
120	9.228149E-14	9.229994E-14
121	1.194613E-13	1.194852E-13
122	1.540036E-13	1.540344E-13
123	1.977283E-13	1.977679E-13
124	2.528617E-13	2.529123E-13
125	3.221175E-13	3.221819E-13
126	4.087916E-13	4.088733E-13
127	5.168734E-13	5.169767E-13
128	6.511755E-13	6.513057E-13
129	8.174845E-13	8.176479E-13
130	1.022736E-12	1.022940E-12
131	1.275215E-12	1.275470E-12
132	1.584792E-12	1.585109E-12
133	1.963189E-12	1.963582E-12
134	2.424284E-12	2.424769E-12
135	2.984464E-12	2.985061E-12
136	3.663026E-12	3.663759E-12
137	4.482627E-12	4.483524E-12
138	5.469802E-12	5.470896E-12
139	6.655547E-12	6.656878E-12
140	8.075973E-12	8.077588E-12
141	9.773052E-12	9.775006E-12
142	1.179544E-11	1.179780E-11
143	1.419943E-11	1.420227E-11
144	1.704996E-11	1.705337E-11
145	2.042180E-11	2.042588E-11
146	2.440084E-11	2.440572E-11
147	2.908555E-11	2.909136E-11
148	3.458853E-11	3.459544E-11
149	4.103831E-11	4.104651E-11
150	4.858129E-11	4.859101E-11
151	5.738391E-11	5.739539E-11
152	6.763499E-11	6.764851E-11
153	7.954831E-11	7.956421E-11
154	9.336554E-11	9.338420E-11
155	1.093593E-10	1.093811E-10
156	1.278365E-10	1.278620E-10
157	1.491422E-10	1.491720E-10
158	1.736637E-10	1.736984E-10
159	2.018347E-10	2.018750E-10
160	2.341402E-10	2.341869E-10

Temperature (K)	Radiance (W cm^{-2} sr^{-1}) Uncorrected	Corrected
161	2.711218E-10	2.711759E-10
162	3.133833E-10	3.134458E-10
163	3.615964E-10	3.616685E-10
164	4.165078E-10	4.165908E-10
165	4.789458E-10	4.790412E-10
166	5.498281E-10	5.499377E-10
167	6.301701E-10	6.302955E-10
168	7.210931E-10	7.212366E-10
169	8.238343E-10	8.239981E-10
170	9.397565E-10	9.399432E-10
171	1.070359E-09	1.070571E-09
172	1.217289E-09	1.217530E-09
173	1.382353E-09	1.382626E-09
174	1.567531E-09	1.567841E-09
175	1.774991E-09	1.775342E-09
176	2.007102E-09	2.007498E-09
177	2.266449E-09	2.266895E-09
178	2.555852E-09	2.556354E-09
179	2.878383E-09	2.878946E-09
180	3.237381E-09	3.238013E-09
181	3.636477E-09	3.637185E-09
182	4.079612E-09	4.080404E-09
183	4.571058E-09	4.571941E-09
184	5.115441E-09	5.116426E-09
185	5.717768E-09	5.718864E-09
186	6.383449E-09	6.384667E-09
187	7.118327E-09	7.119676E-09
188	7.928701E-09	7.930194E-09
189	8.821360E-09	8.823011E-09
190	9.803614E-09	9.805434E-09
191	1.088332E-08	1.088532E-08
192	1.206893E-08	1.207113E-08
193	1.336950E-08	1.337191E-08
194	1.479475E-08	1.479739E-08
195	1.635511E-08	1.635799E-08
196	1.806172E-08	1.806486E-08
197	1.992652E-08	1.992993E-08
198	2.196225E-08	2.196594E-08
199	2.418252E-08	2.418650E-08
200	2.660186E-08	2.660615E-08
201	2.923575E-08	2.924035E-08
202	3.210069E-08	3.210561E-08
203	3.521423E-08	3.521946E-08
204	3.859504E-08	3.860059E-08
205	4.226296E-08	4.226881E-08
206	4.623907E-08	4.624520E-08
207	5.054572E-08	5.055210E-08
208	5.520662E-08	5.521322E-08
209	6.024690E-08	6.025366E-08
210	6.569316E-08	6.570000E-08
211	7.157354E-08	7.158038E-08

Temperature (K)	Radiance (W cm^{-2} sr^{-1}) Uncorrected	Corrected
212	7.791780E-08	7.792453E-08
213	8.475740E-08	8.476387E-08
214	9.212555E-08	9.213159E-08
215	1.000573E-07	1.000627E-07
216	1.085896E-07	1.085941E-07
217	1.177614E-07	1.177647E-07
218	1.276137E-07	1.276155E-07
219	1.381898E-07	1.381896E-07
220	1.495350E-07	1.495323E-07
221	1.616971E-07	1.616913E-07
222	1.747263E-07	1.747168E-07
223	1.886753E-07	1.886612E-07
224	2.035994E-07	2.035798E-07
225	2.195567E-07	2.195304E-07
226	2.366079E-07	2.365736E-07
227	2.548167E-07	2.547731E-07
228	2.742499E-07	2.741952E-07
229	2.949773E-07	2.949096E-07
230	3.170719E-07	3.169890E-07
231	3.406102E-07	3.405095E-07
232	3.656719E-07	3.655505E-07
233	3.923404E-07	3.921949E-07
234	4.207027E-07	4.205294E-07
235	4.508496E-07	4.506442E-07
236	4.828757E-07	4.826333E-07
237	5.168798E-07	5.165949E-07
238	5.529647E-07	5.526310E-07
239	5.912374E-07	5.908479E-07
240	6.318094E-07	6.313561E-07
241	6.747967E-07	6.742707E-07
242	7.203199E-07	7.197112E-07
243	7.685044E-07	7.678016E-07
244	8.194805E-07	8.186708E-07
245	8.733833E-07	8.724527E-07
246	9.303535E-07	9.292860E-07
247	9.905368E-07	9.893146E-07
248	1.054084E-06	1.052688E-06
249	1.121153E-06	1.119560E-06
250	1.191905E-06	1.190090E-06
251	1.266509E-06	1.264446E-06
252	1.345139E-06	1.342797E-06
253	1.427976E-06	1.425321E-06
254	1.515206E-06	1.512201E-06
255	1.607023E-06	1.603626E-06
256	1.703627E-06	1.699792E-06
257	1.805223E-06	1.800900E-06
258	1.912026E-06	1.907158E-06
259	2.024255E-06	2.018781E-06
260	2.142139E-06	2.135990E-06
261	2.265911E-06	2.259014E-06
262	2.395816E-06	2.388086E-06

Temperature	Radiance (W cm^{-2} sr^{-1})	
(K)	Uncorrected	Corrected
263	2.532101E-06	2.523450E-06
264	2.675026E-06	2.665353E-06
265	2.824856E-06	2.814052E-06
266	2.981865E-06	2.969811E-06
267	3.146334E-06	3.132899E-06
268	3.318554E-06	3.303596E-06
269	3.498825E-06	3.482186E-06
270	3.687453E-06	3.668964E-06
271	3.884755E-06	3.864230E-06
272	4.091057E-06	4.068293E-06
273	4.306693E-06	4.281471E-06
274	4.532007E-06	4.504087E-06
275	4.767353E-06	4.736475E-06
276	5.013094E-06	4.978976E-06
277	5.269602E-06	5.231938E-06
278	5.537261E-06	5.495719E-06
279	5.816462E-06	5.770684E-06
280	6.107610E-06	6.057208E-06
281	6.411117E-06	6.355673E-06
282	6.727408E-06	6.666470E-06
283	7.056917E-06	6.989998E-06
284	7.400090E-06	7.326666E-06
285	7.757383E-06	7.676890E-06
286	8.129263E-06	8.041096E-06
287	8.516211E-06	8.419719E-06
288	8.918715E-06	8.813200E-06
289	9.337278E-06	9.221994E-06
290	9.772414E-06	9.646559E-06
291	1.022465E-05	1.008737E-05
292	1.069452E-05	1.054490E-05
293	1.118257E-05	1.101964E-05
294	1.168937E-05	1.151210E-05
295	1.221549E-05	1.202277E-05
296	1.276152E-05	1.255217E-05
297	1.332805E-05	1.310084E-05
298	1.391571E-05	1.366931E-05
299	1.452511E-05	1.425813E-05
300	1.515689E-05	1.486786E-05
301	1.581171E-05	1.549906E-05
302	1.649023E-05	1.615232E-05
303	1.719312E-05	1.682824E-05
304	1.792108E-05	1.752740E-05
305	1.867482E-05	1.825044E-05
306	1.945506E-05	1.899799E-05

Temperature	Radiance (W cm^{-2} sr^{-1})	
(K)	Uncorrected	Corrected
307	2.026252E-05	1.977068E-05
308	2.109796E-05	2.056917E-05
309	2.196213E-05	2.139415E-05
310	2.285582E-05	2.224629E-05
311	2.377981E-05	2.312631E-05
312	2.473491E-05	2.403493E-05
313	2.572194E-05	2.497289E-05
314	2.674173E-05	2.594097E-05
315	2.779513E-05	2.693994E-05
316	2.888300E-05	2.797063E-05
317	3.000623E-05	2.903386E-05
318	3.116570E-05	3.013050E-05
319	3.236233E-05	3.126145E-05
320	3.359704E-05	3.242763E-05
321	3.487077E-05	3.363002E-05
322	3.618448E-05	3.486959E-05
323	3.753913E-05	3.614742E-05
324	3.893572E-05	3.746457E-05
325	4.037523E-05	3.882218E-05
326	4.185870E-05	4.022146E-05
327	4.338716E-05	4.166363E-05
328	4.496165E-05	4.315003E-05
329	4.658325E-05	4.468202E-05
330	4.825302E-05	4.626107E-05
331	4.997208E-05	4.788871E-05
332	5.174153E-05	4.956656E-05
333	5.356250E-05	5.129636E-05
334	5.543614E-05	5.307992E-05
335	5.736362E-05	5.491919E-05
336	5.934610E-05	5.681624E-05
337	6.138479E-05	5.877326E-05
338	6.348091E-05	6.079261E-05
339	6.563566E-05	6.287679E-05
340	6.785031E-05	6.502848E-05
341	7.012612E-05	6.725055E-05
342	7.246435E-05	6.954606E-05
343	7.486631E-05	7.191832E-05
344	7.733330E-05	7.437083E-05
345	7.986666E-05	7.690740E-05
346	8.246773E-05	7.953207E-05
347	8.513787E-05	8.224922E-05
348	8.787846E-05	8.506354E-05
349	9.069089E-05	8.798006E-05
350	9.357658E-05	9.100420E-05

11µm Temperature/Radiance Lookup Table

Polynomial fall off coefficients:
z0 = 1.00110E+00
z1 = -3.42823E-02
z2 = -8.17089E-03

Temperature (K)	Radiance (W cm^{-2} sr^{-1}) Uncorrected	Corrected
77	1.907970E-09	1.910069E-09
78	2.375848E-09	2.378462E-09
79	2.942154E-09	2.945390E-09
80	3.624108E-09	3.628094E-09
81	4.441312E-09	4.446196E-09
82	5.415976E-09	5.421933E-09
83	6.573170E-09	6.580399E-09
84	7.941071E-09	7.949804E-09
85	9.551235E-09	9.561738E-09
86	1.143887E-08	1.145145E-08
87	1.364311E-08	1.365811E-08
88	1.620733E-08	1.622515E-08
89	1.917942E-08	1.920050E-08
90	2.261210E-08	2.263695E-08
91	2.656323E-08	2.659242E-08
92	3.109614E-08	3.113031E-08
93	3.627991E-08	3.631976E-08
94	4.218972E-08	4.223606E-08
95	4.890717E-08	4.896088E-08
96	5.652058E-08	5.658263E-08
97	6.512534E-08	6.519681E-08
98	7.482418E-08	7.490628E-08
99	8.572755E-08	8.582157E-08
100	9.795385E-08	9.806123E-08
101	1.116298E-07	1.117521E-07
102	1.268907E-07	1.270297E-07
103	1.438808E-07	1.440382E-07
104	1.627533E-07	1.629313E-07
105	1.836711E-07	1.838719E-07
106	2.068067E-07	2.070325E-07
107	2.323424E-07	2.325959E-07
108	2.604709E-07	2.607548E-07
109	2.913951E-07	2.917124E-07
110	3.253287E-07	3.256825E-07
111	3.624962E-07	3.628898E-07
112	4.031329E-07	4.035701E-07
113	4.474855E-07	4.479700E-07
114	4.958120E-07	4.963479E-07
115	5.483818E-07	5.489734E-07
116	6.054758E-07	6.061277E-07
117	6.673868E-07	6.681037E-07
118	7.344193E-07	7.352063E-07
119	8.068896E-07	8.077521E-07

Temperature (K)	Radiance (W cm^{-2} sr^{-1}) Uncorrected	Corrected
120	8.851261E-07	8.860695E-07
121	9.694689E-07	9.704991E-07
122	1.060270E-06	1.061393E-06
123	1.157895E-06	1.159117E-06
124	1.262718E-06	1.264046E-06
125	1.375129E-06	1.376569E-06
126	1.495527E-06	1.497086E-06
127	1.624325E-06	1.626010E-06
128	1.761946E-06	1.763764E-06
129	1.908826E-06	1.910785E-06
130	2.065411E-06	2.067519E-06
131	2.232162E-06	2.234425E-06
132	2.409547E-06	2.411974E-06
133	2.598049E-06	2.600646E-06
134	2.798159E-06	2.800935E-06
135	3.010381E-06	3.013343E-06
136	3.235229E-06	3.238384E-06
137	3.473227E-06	3.476582E-06
138	3.724912E-06	3.728473E-06
139	3.990827E-06	3.994602E-06
140	4.271527E-06	4.275522E-06
141	4.567579E-06	4.571798E-06
142	4.879555E-06	4.884003E-06
143	5.208040E-06	5.212721E-06
144	5.553625E-06	5.558543E-06
145	5.916912E-06	5.922068E-06
146	6.298510E-06	6.303906E-06
147	6.699037E-06	6.704672E-06
148	7.119118E-06	7.124991E-06
149	7.559387E-06	7.565494E-06
150	8.020483E-06	8.026819E-06
151	8.503054E-06	8.509613E-06
152	9.007754E-06	9.014526E-06
153	9.535243E-06	9.542217E-06
154	1.008619E-05	1.009335E-05
155	1.066126E-05	1.066859E-05
156	1.126114E-05	1.126862E-05
157	1.188651E-05	1.189412E-05
158	1.253805E-05	1.254576E-05
159	1.321646E-05	1.322424E-05
160	1.392243E-05	1.393025E-05
161	1.465667E-05	1.466448E-05
162	1.541988E-05	1.542764E-05

Temperature	Radiance (W cm^{-2} sr^{-1})	
(K)	Uncorrected	Corrected
163	1.621276E-05	1.622042E-05
164	1.703603E-05	1.704353E-05
165	1.789040E-05	1.789768E-05
166	1.877658E-05	1.878357E-05
167	1.969529E-05	1.970192E-05
168	2.064724E-05	2.065343E-05
169	2.163317E-05	2.163882E-05
170	2.265379E-05	2.265880E-05
171	2.370981E-05	2.371408E-05
172	2.480198E-05	2.480538E-05
173	2.593100E-05	2.593341E-05
174	2.709760E-05	2.709888E-05
175	2.830250E-05	2.830251E-05
176	2.954643E-05	2.954500E-05
177	3.083010E-05	3.082706E-05
178	3.215424E-05	3.214940E-05
179	3.351956E-05	3.351272E-05
180	3.492679E-05	3.491773E-05
181	3.637663E-05	3.636512E-05
182	3.786981E-05	3.785560E-05
183	3.940702E-05	3.938985E-05
184	4.098898E-05	4.096857E-05
185	4.261640E-05	4.259244E-05
186	4.428997E-05	4.426215E-05
187	4.601040E-05	4.597837E-05
188	4.777838E-05	4.774178E-05
189	4.959460E-05	4.955305E-05
190	5.145975E-05	5.141284E-05
191	5.337452E-05	5.332181E-05
192	5.533958E-05	5.528061E-05
193	5.735561E-05	5.728990E-05
194	5.942328E-05	5.935031E-05
195	6.154325E-05	6.146249E-05
196	6.371619E-05	6.362706E-05
197	6.594276E-05	6.584465E-05
198	6.822359E-05	6.811587E-05
199	7.055934E-05	7.044135E-05
200	7.295065E-05	7.282167E-05
201	7.539815E-05	7.525744E-05
202	7.790247E-05	7.774926E-05
203	8.046422E-05	8.029769E-05
204	8.308404E-05	8.290332E-05
205	8.576251E-05	8.556671E-05
206	8.850026E-05	8.828842E-05
207	9.129787E-05	9.106901E-05
208	9.415593E-05	9.390902E-05
209	9.707504E-05	9.680898E-05
210	1.000558E-04	9.976943E-05
211	1.030987E-04	1.027909E-04
212	1.062043E-04	1.058738E-04
213	1.093733E-04	1.090188E-04

Temperature	Radiance (W cm^{-2} sr^{-1})	
(K)	Uncorrected	Corrected
214	1.126061E-04	1.122262E-04
215	1.159033E-04	1.154967E-04
216	1.192654E-04	1.188306E-04
217	1.226930E-04	1.222284E-04
218	1.261866E-04	1.256906E-04
219	1.297467E-04	1.292177E-04
220	1.333737E-04	1.328100E-04
221	1.370683E-04	1.364680E-04
222	1.408308E-04	1.401921E-04
223	1.446619E-04	1.439827E-04
224	1.485618E-04	1.478403E-04
225	1.525312E-04	1.517652E-04
226	1.565705E-04	1.557577E-04
227	1.606800E-04	1.598183E-04
228	1.648604E-04	1.639474E-04
229	1.691119E-04	1.681452E-04
230	1.734351E-04	1.724121E-04
231	1.778304E-04	1.767484E-04
232	1.822981E-04	1.811546E-04
233	1.868388E-04	1.856307E-04
234	1.914527E-04	1.901773E-04
235	1.961402E-04	1.947945E-04
236	2.009019E-04	1.994827E-04
237	2.057380E-04	2.042420E-04
238	2.106488E-04	2.090729E-04
239	2.156349E-04	2.139754E-04
240	2.206965E-04	2.189499E-04
241	2.258339E-04	2.239966E-04
242	2.310476E-04	2.291157E-04
243	2.363378E-04	2.343074E-04
244	2.417048E-04	2.395719E-04
245	2.471490E-04	2.449094E-04
246	2.526708E-04	2.503201E-04
247	2.582703E-04	2.558041E-04
248	2.639478E-04	2.613616E-04
249	2.697038E-04	2.669928E-04
250	2.755384E-04	2.726977E-04
251	2.814520E-04	2.784765E-04
252	2.874447E-04	2.843293E-04
253	2.935168E-04	2.902562E-04
254	2.996687E-04	2.962573E-04
255	3.059005E-04	3.023328E-04
256	3.122125E-04	3.084826E-04
257	3.186049E-04	3.147068E-04
258	3.250779E-04	3.210055E-04
259	3.316318E-04	3.273787E-04
260	3.382668E-04	3.338264E-04
261	3.449830E-04	3.403488E-04
262	3.517806E-04	3.469457E-04
263	3.586600E-04	3.536172E-04
264	3.656211E-04	3.603633E-04

Temperature (K)	Radiance (W cm^{-2} sr^{-1}) Uncorrected	Corrected
265	3.726643E-04	3.671839E-04
266	3.797896E-04	3.740790E-04
267	3.869973E-04	3.810487E-04
268	3.942874E-04	3.880927E-04
269	4.016603E-04	3.952112E-04
270	4.091159E-04	4.024039E-04
271	4.166544E-04	4.096708E-04
272	4.242761E-04	4.170119E-04
273	4.319809E-04	4.244270E-04
274	4.397690E-04	4.319160E-04
275	4.476406E-04	4.394788E-04
276	4.555957E-04	4.471153E-04
277	4.636344E-04	4.548253E-04
278	4.717569E-04	4.626086E-04
279	4.799632E-04	4.704652E-04
280	4.882535E-04	4.783948E-04
281	4.966277E-04	4.863972E-04
282	5.050860E-04	4.944723E-04
283	5.136285E-04	5.026198E-04
284	5.222551E-04	5.108396E-04
285	5.309661E-04	5.191314E-04
286	5.397613E-04	5.274950E-04
287	5.486410E-04	5.359302E-04
288	5.576050E-04	5.444367E-04
289	5.666535E-04	5.530142E-04
290	5.757865E-04	5.616624E-04
291	5.850040E-04	5.703812E-04
292	5.943060E-04	5.791701E-04
293	6.036926E-04	5.880290E-04
294	6.131638E-04	5.969574E-04
295	6.227195E-04	6.059551E-04
296	6.323599E-04	6.150218E-04
297	6.420848E-04	6.241571E-04
298	6.518944E-04	6.333606E-04
299	6.617885E-04	6.426320E-04
300	6.717672E-04	6.519709E-04
301	6.818304E-04	6.613770E-04
302	6.919782E-04	6.708499E-04
303	7.022105E-04	6.803891E-04
304	7.125272E-04	6.899943E-04
305	7.229284E-04	6.996650E-04
306	7.334140E-04	7.094009E-04
307	7.439840E-04	7.192015E-04

Temperature (K)	Radiance (W cm^{-2} sr^{-1}) Uncorrected	Corrected
308	7.546383E-04	7.290663E-04
309	7.653769E-04	7.389949E-04
310	7.761998E-04	7.489869E-04
311	7.871068E-04	7.590417E-04
312	7.980979E-04	7.691589E-04
313	8.091730E-04	7.793380E-04
314	8.203321E-04	7.895785E-04
315	8.315752E-04	7.998799E-04
316	8.429021E-04	8.102416E-04
317	8.543128E-04	8.206632E-04
318	8.658071E-04	8.311441E-04
319	8.773851E-04	8.416838E-04
320	8.890465E-04	8.522816E-04
321	9.007914E-04	8.629371E-04
322	9.126197E-04	8.736497E-04
323	9.245312E-04	8.844187E-04
324	9.365258E-04	8.952437E-04
325	9.486035E-04	9.061239E-04
326	9.607641E-04	9.170588E-04
327	9.730075E-04	9.280478E-04
328	9.853337E-04	9.390902E-04
329	9.977425E-04	9.501854E-04
330	1.010234E-03	9.613328E-04
331	1.022808E-03	9.725317E-04
332	1.035463E-03	9.837813E-04
333	1.048202E-03	9.950812E-04
334	1.061022E-03	1.006431E-03
335	1.073924E-03	1.017829E-03
336	1.086908E-03	1.029275E-03
337	1.099973E-03	1.040768E-03
338	1.113120E-03	1.052309E-03
339	1.126348E-03	1.063895E-03
340	1.139658E-03	1.075526E-03
341	1.153048E-03	1.087202E-03
342	1.166520E-03	1.098921E-03
343	1.180072E-03	1.110684E-03
344	1.193705E-03	1.122488E-03
345	1.207419E-03	1.134334E-03
346	1.221213E-03	1.146220E-03
347	1.235087E-03	1.158147E-03
348	1.249041E-03	1.170112E-03
349	1.263075E-03	1.182115E-03
350	1.277189E-03	1.194156E-03

12µm Temperature/Radiance Lookup Table

Polynomial fall off coefficients:
z0 = 1.00327E+00
z1 = -8.43871E-02
z2 = 7.10950E-04

Temperature (K)	Radiance (W cm^{-2} sr^{-1}) Uncorrected	Corrected
77	8.271123E-09	8.298164E-09
78	1.007586E-08	1.010880E-08
79	1.221356E-08	1.225348E-08
80	1.473415E-08	1.478232E-08
81	1.769325E-08	1.775108E-08
82	2.115252E-08	2.122166E-08
83	2.518015E-08	2.526244E-08
84	2.985121E-08	2.994876E-08
85	3.524813E-08	3.536329E-08
86	4.146108E-08	4.159652E-08
87	4.858843E-08	4.874713E-08
88	5.673716E-08	5.692243E-08
89	6.602325E-08	6.623880E-08
90	7.657213E-08	7.682206E-08
91	8.851909E-08	8.880792E-08
92	1.020096E-07	1.023424E-07
93	1.171998E-07	1.175820E-07
94	1.342568E-07	1.346944E-07
95	1.533591E-07	1.538587E-07
96	1.746967E-07	1.752656E-07
97	1.984719E-07	1.991178E-07
98	2.248991E-07	2.256305E-07
99	2.542054E-07	2.550315E-07
100	2.866307E-07	2.875615E-07
101	3.224281E-07	3.234742E-07
102	3.618641E-07	3.630370E-07
103	4.052186E-07	4.065307E-07
104	4.527854E-07	4.542498E-07
105	5.048721E-07	5.065028E-07
106	5.618002E-07	5.636123E-07
107	6.239057E-07	6.259150E-07
108	6.915384E-07	6.937619E-07
109	7.650627E-07	7.675182E-07
110	8.448573E-07	8.475634E-07
111	9.313150E-07	9.342917E-07
112	1.024843E-06	1.028111E-06
113	1.125863E-06	1.129445E-06
114	1.234811E-06	1.238728E-06
115	1.352137E-06	1.356414E-06
116	1.478305E-06	1.482966E-06
117	1.613793E-06	1.618864E-06
118	1.759092E-06	1.764600E-06
119	1.914709E-06	1.920680E-06

Temperature (K)	Radiance (W cm^{-2} sr^{-1}) Uncorrected	Corrected
120	2.081162E-06	2.087624E-06
121	2.258982E-06	2.265965E-06
122	2.448716E-06	2.456249E-06
123	2.650921E-06	2.659033E-06
124	2.866168E-06	2.874890E-06
125	3.095039E-06	3.104401E-06
126	3.338129E-06	3.348162E-06
127	3.596044E-06	3.606779E-06
128	3.869402E-06	3.880869E-06
129	4.158831E-06	4.171062E-06
130	4.464972E-06	4.477994E-06
131	4.788474E-06	4.802317E-06
132	5.129996E-06	5.144687E-06
133	5.490207E-06	5.505774E-06
134	5.869787E-06	5.886254E-06
135	6.269423E-06	6.286812E-06
136	6.689810E-06	6.708142E-06
137	7.131652E-06	7.150946E-06
138	7.595661E-06	7.615932E-06
139	8.082556E-06	8.103814E-06
140	8.593062E-06	8.615316E-06
141	9.127911E-06	9.151164E-06
142	9.687842E-06	9.712091E-06
143	1.027360E-05	1.029884E-05
144	1.088593E-05	1.091214E-05
145	1.152558E-05	1.155276E-05
146	1.219333E-05	1.222143E-05
147	1.288992E-05	1.291891E-05
148	1.361612E-05	1.364597E-05
149	1.437270E-05	1.440335E-05
150	1.516044E-05	1.519182E-05
151	1.598010E-05	1.601214E-05
152	1.683247E-05	1.686508E-05
153	1.771831E-05	1.775140E-05
154	1.863841E-05	1.867186E-05
155	1.959354E-05	1.962723E-05
156	2.058449E-05	2.061827E-05
157	2.161204E-05	2.164574E-05
158	2.267696E-05	2.271041E-05
159	2.378002E-05	2.381303E-05
160	2.492202E-05	2.495435E-05
161	2.610372E-05	2.613514E-05
162	2.732589E-05	2.735615E-05

Temperature (K)	Radiance (W cm^{-2} sr^{-1}) Uncorrected	Corrected
163	2.858932E-05	2.861811E-05
164	2.989476E-05	2.992178E-05
165	3.124299E-05	3.126790E-05
166	3.263476E-05	3.265719E-05
167	3.407085E-05	3.409038E-05
168	3.555199E-05	3.556821E-05
169	3.707895E-05	3.709139E-05
170	3.865248E-05	3.866063E-05
171	4.027331E-05	4.027664E-05
172	4.194219E-05	4.194012E-05
173	4.365985E-05	4.365176E-05
174	4.542702E-05	4.541225E-05
175	4.724441E-05	4.722227E-05
176	4.911276E-05	4.908248E-05
177	5.103277E-05	5.099355E-05
178	5.300514E-05	5.295614E-05
179	5.503057E-05	5.497088E-05
180	5.710976E-05	5.703843E-05
181	5.924340E-05	5.915939E-05
182	6.143215E-05	6.133441E-05
183	6.367669E-05	6.356407E-05
184	6.597768E-05	6.584899E-05
185	6.833579E-05	6.818976E-05
186	7.075166E-05	7.058694E-05
187	7.322592E-05	7.304112E-05
188	7.575923E-05	7.555286E-05
189	7.835219E-05	7.812269E-05
190	8.100543E-05	8.075117E-05
191	8.371956E-05	8.343881E-05
192	8.649518E-05	8.618614E-05
193	8.933287E-05	8.899366E-05
194	9.223323E-05	9.186186E-05
195	9.519683E-05	9.479122E-05
196	9.822424E-05	9.778223E-05
197	1.013160E-04	1.008353E-04
198	1.044727E-04	1.039510E-04
199	1.076948E-04	1.071296E-04
200	1.109830E-04	1.103716E-04
201	1.143376E-04	1.136775E-04
202	1.177592E-04	1.170475E-04
203	1.212484E-04	1.204822E-04
204	1.248056E-04	1.239818E-04
205	1.284313E-04	1.275468E-04
206	1.321260E-04	1.311775E-04
207	1.358902E-04	1.348742E-04
208	1.397242E-04	1.386373E-04
209	1.436287E-04	1.424670E-04
210	1.476039E-04	1.463638E-04
211	1.516503E-04	1.503278E-04
212	1.557685E-04	1.543593E-04
213	1.599586E-04	1.584587E-04

Temperature (K)	Radiance (W cm^{-2} sr^{-1}) Uncorrected	Corrected
214	1.642213E-04	1.626261E-04
215	1.685568E-04	1.668618E-04
216	1.729656E-04	1.711660E-04
217	1.774481E-04	1.755390E-04
218	1.820045E-04	1.799810E-04
219	1.866353E-04	1.844920E-04
220	1.913408E-04	1.890724E-04
221	1.961213E-04	1.937223E-04
222	2.009772E-04	1.984418E-04
223	2.059089E-04	2.032311E-04
224	2.109165E-04	2.080903E-04
225	2.160005E-04	2.130196E-04
226	2.211612E-04	2.180189E-04
227	2.263987E-04	2.230885E-04
228	2.317134E-04	2.282284E-04
229	2.371057E-04	2.334387E-04
230	2.425756E-04	2.387194E-04
231	2.481235E-04	2.440705E-04
232	2.537497E-04	2.494922E-04
233	2.594543E-04	2.549845E-04
234	2.652377E-04	2.605472E-04
235	2.710999E-04	2.661805E-04
236	2.770414E-04	2.718844E-04
237	2.830621E-04	2.776588E-04
238	2.891624E-04	2.835036E-04
239	2.953425E-04	2.894189E-04
240	3.016024E-04	2.954045E-04
241	3.079425E-04	3.014605E-04
242	3.143628E-04	3.075867E-04
243	3.208636E-04	3.137830E-04
244	3.274449E-04	3.200494E-04
245	3.341070E-04	3.263857E-04
246	3.408499E-04	3.327918E-04
247	3.476738E-04	3.392676E-04
248	3.545789E-04	3.458129E-04
249	3.615651E-04	3.524276E-04
250	3.686328E-04	3.591116E-04
251	3.757818E-04	3.658646E-04
252	3.830125E-04	3.726864E-04
253	3.903247E-04	3.795770E-04
254	3.977187E-04	3.865360E-04
255	4.051945E-04	3.935633E-04
256	4.127521E-04	4.006587E-04
257	4.203917E-04	4.078218E-04
258	4.281133E-04	4.150526E-04
259	4.359169E-04	4.223507E-04
260	4.438026E-04	4.297159E-04
261	4.517705E-04	4.371479E-04
262	4.598205E-04	4.446464E-04
263	4.679527E-04	4.522112E-04
264	4.761672E-04	4.598419E-04

Temperature (K)	Radiance (W cm^{-2} sr^{-1}) Uncorrected	Corrected
265	4.844638E-04	4.675384E-04
266	4.928427E-04	4.753002E-04
267	5.013039E-04	4.831270E-04
268	5.098473E-04	4.910185E-04
269	5.184730E-04	4.989745E-04
270	5.271809E-04	5.069945E-04
271	5.359710E-04	5.150782E-04
272	5.448434E-04	5.232253E-04
273	5.537979E-04	5.314353E-04
274	5.628346E-04	5.397080E-04
275	5.719534E-04	5.480429E-04
276	5.811542E-04	5.564397E-04
277	5.904371E-04	5.648979E-04
278	5.998020E-04	5.734172E-04
279	6.092489E-04	5.819972E-04
280	6.187776E-04	5.906375E-04
281	6.283881E-04	5.993375E-04
282	6.380803E-04	6.080970E-04
283	6.478543E-04	6.169155E-04
284	6.577098E-04	6.257925E-04
285	6.676469E-04	6.347276E-04
286	6.776654E-04	6.437204E-04
287	6.877653E-04	6.527704E-04
288	6.979464E-04	6.618771E-04
289	7.082087E-04	6.710401E-04
290	7.185521E-04	6.802589E-04
291	7.289765E-04	6.895330E-04
292	7.394818E-04	6.988620E-04
293	7.500678E-04	7.082453E-04
294	7.607345E-04	7.176825E-04
295	7.714817E-04	7.271730E-04
296	7.823093E-04	7.367165E-04
297	7.932172E-04	7.463122E-04
298	8.042054E-04	7.559599E-04
299	8.152735E-04	7.656588E-04
300	8.264216E-04	7.754086E-04
301	8.376495E-04	7.852086E-04
302	8.489570E-04	7.950584E-04
303	8.603441E-04	8.049574E-04
304	8.718105E-04	8.149051E-04
305	8.833562E-04	8.249009E-04
306	8.949809E-04	8.349444E-04
307	9.066846E-04	8.450348E-04

Temperature (K)	Radiance (W cm^{-2} sr^{-1}) Uncorrected	Corrected
308	9.184671E-04	8.551718E-04
309	9.303282E-04	8.653546E-04
310	9.422677E-04	8.755829E-04
311	9.542856E-04	8.858560E-04
312	9.663816E-04	8.961732E-04
313	9.785557E-04	9.065342E-04
314	9.908075E-04	9.169383E-04
315	1.003137E-03	9.273848E-04
316	1.015544E-03	9.378733E-04
317	1.028028E-03	9.484032E-04
318	1.040590E-03	9.589738E-04
319	1.053228E-03	9.695846E-04
320	1.065943E-03	9.802350E-04
321	1.078735E-03	9.909244E-04
322	1.091604E-03	1.001652E-03
323	1.104548E-03	1.012418E-03
324	1.117569E-03	1.023221E-03
325	1.130665E-03	1.034060E-03
326	1.143837E-03	1.044935E-03
327	1.157085E-03	1.055846E-03
328	1.170408E-03	1.066792E-03
329	1.183806E-03	1.077771E-03
330	1.197279E-03	1.088785E-03
331	1.210827E-03	1.099831E-03
332	1.224449E-03	1.110909E-03
333	1.238146E-03	1.122019E-03
334	1.251917E-03	1.133161E-03
335	1.265761E-03	1.144332E-03
336	1.279680E-03	1.155534E-03
337	1.293672E-03	1.166765E-03
338	1.307737E-03	1.178024E-03
339	1.321876E-03	1.189311E-03
340	1.336087E-03	1.200626E-03
341	1.350371E-03	1.211967E-03
342	1.364728E-03	1.223335E-03
343	1.379157E-03	1.234727E-03
344	1.393658E-03	1.246145E-03
345	1.408231E-03	1.257587E-03
346	1.422876E-03	1.269052E-03
347	1.437592E-03	1.280540E-03
348	1.452379E-03	1.292051E-03
349	1.467238E-03	1.303583E-03
350	1.482167E-03	1.315136E-03

Appendix D Test Data Files

Test	Description	Condition	Level1 File	Level 2 File	Raw Data File
RAD02	Radiometric Strays	BOL	RAD02$01-FEB-1998.LEV1	RAD02$01-FEB-1998.LEV2	RAD02$01-FEB-1998.PKT
			RAD02$02-FEB-1998.LEV1	RAD02$02-FEB-1998.LEV2	RAD02$02-FEB-1998.PKT
		Repeat	RAD02$14-NOV-1998.LEV1	RAD02$14-NOV-1998.LEV2	RAD02$14-NOV-1998.PKT
		Repeat	RAD02$15-NOV-1998.LEV1	RAD02$15-NOV-1998.LEV2	RAD02$15-NOV-1998.PKT
		Repeat	RAD02$16-NOV-1998.LEV1	RAD02$16-NOV-1998.LEV2	RAD02$16-NOV-1998.PKT
RAD03	Calibration at Centre of Nadir View	BOL	RAD03$03-FEB-1998.LEV1	RAD03$03-FEB-1998.LEV2	RAD03$03-FEB-1998.PKT
			RAD03$04-FEB-1998.LEV1	RAD03$04-FEB-1998.LEV2	RAD03$04-FEB-1998.PKT
			RAD03$05-FEB-1998.LEV1	RAD03$05-FEB-1998.LEV2	RAD03$05-FEB-1998.PKT
			RAD03$06-FEB-1998.LEV1	RAD03$06-FEB-1998.LEV2	RAD03$06-FEB-1998.PKT
		Repeat	RAD03$16-NOV-1998.LEV1	RAD03$16-NOV-1998.LEV2	RAD03$16-NOV-1998.PKT
		Repeat	RAD03$17-NOV-1998.LEV1	RAD03$17-NOV-1998.LEV2	RAD03$17-NOV-1998.PKT
		Repeat	RAD03$18-NOV-1998.LEV1	RAD03$18-NOV-1998.LEV2	RAD03$18-NOV-1998.PKT
		Repeat	RAD03$19-NOV-1998.LEV1	RAD03$19-NOV-1998.LEV2	RAD03$19-NOV-1998.PKT
RAD04	Calibration with detectors at 90K	BOL	RAD04$06-FEB-1998.LEV1	RAD04$06-FEB-1998.LEV2	RAD04$06-FEB-1998.PKT
		Repeat	RAD04$19-NOV-1998.LEV1	RAD04$19-NOV-1998.LEV2	RAD04$19-NOV-1998.PKT
		Repeat	RAD04$20-NOV-1998.LEV1	RAD04$20-NOV-1998.LEV2	RAD04$20-NOV-1998.PKT
RAD05	Calibration Around Nadir Swath	BOL	RAD05A$07-FEB-1998.LEV1	RAD05A$07-FEB-1998.LEV2	RAD05A$07-FEB-1998.PKT
			RAD05$07-FEB-1998.LEV1	RAD05$07-FEB-1998.LEV2	RAD05$07-FEB-1998.PKT
			RAD05$08-FEB-1998.LEV1	RAD05$08-FEB-1998.LEV2	RAD05$08-FEB-1998.PKT
			RAD05$09-FEB-1998.LEV1	RAD05$09-FEB-1998.LEV2	RAD05$09-FEB-1998.PKT
		Repeat	RAD05$20-NOV-1998.LEV1	RAD05$20-NOV-1998.LEV2	RAD05$20-NOV-1998.PKT
		Repeat	RAD05$21-NOV-1998.LEV1	RAD05$21-NOV-1998.LEV2	RAD05$21-NOV-1998.PKT
RAD06	Calibration Around Along-Track Swath	BOL	RAD06$09-FEB-1998.LEV1	RAD06$09-FEB-1998.LEV2	RAD06$09-FEB-1998.PKT
		Repeat	RAD06$21-NOV-1998.LEV1	RAD06$21-NOV-1998.LEV2	RAD06$21-NOV-1998.PKT
		Repeat	RAD06$22-NOV-1998.LEV1	RAD06$22-NOV-1998.LEV2	RAD06$22-NOV-1998.PKT
RAD07	Calibration with -XBB at power level 2	BOL	RAD07$24-NOV-1998.LEV1	RAD07$24-NOV-1998.LEV2	RAD07$24-NOV-1998.PKT
			RAD07$25-NOV-1998.LEV1	RAD07$25-NOV-1998.LEV2	RAD07$25-NOV-1998.PKT
RAD08	Calibration with -XBB at power level 3	BOL	RAD08$25-NOV-1998.LEV1	RAD08$25-NOV-1998.LEV2	RAD08$25-NOV-1998.PKT
			RAD08$26-NOV-1998.LEV1	RAD08$26-NOV-1998.LEV2	RAD08$26-NOV-1998.PKT

Test	Description	Condition	Level1 File	Level 2 File	Raw Data File
RAD09	Calibration with +XBB at power level 3	BOL	RAD09$27-NOV-1998.LEV1	RAD09$27-NOV-1998.LEV2	RAD09$27-NOV-1998.PKT
			RAD09$28-NOV-1998.LEV1	RAD09$28-NOV-1998.LEV2	RAD09$28-NOV-1998.PKT
RAD10	Calibration with +XBB at power level 1	BOL	RAD10$29-NOV-1998.LEV1	RAD10$29-NOV-1998.LEV2	RAD10$29-NOV-1998.PKT
			RAD10$30-NOV-1998.LEV1	RAD10$30-NOV-1998.LEV2	RAD10$30-NOV-1998.PKT
RAD11	Calibration at EOL Conditions	EOL	RAD11$02-DEC-1998.LEV1	RAD11$02-DEC-1998.LEV2	RAD11$02-DEC-1998.PKT
			RAD11$03-DEC-1998.LEV1	RAD11$03-DEC-1998.LEV2	RAD11$03-DEC-1998.PKT
RAD12	Repeat Calibration at BOL Conditions	BOL	RAD12$05-DEC-1998.LEV1	RAD12$05-DEC-1998.LEV2	RAD12$05-DEC-1998.PKT
			RAD12$07-DEC-1998.LEV1	RAD12$07-DEC-1998.LEV2	RAD12$07-DEC-1998.PKT
			RAD12$08-DEC-1998.LEV1	RAD12$08-DEC-1998.LEV2	RAD12$08-DEC-1998.PKT
RAD13	Calibration with increased ESS temperatur	BOL	RAD13$09-DEC-1998.LEV1	RAD13$09-DEC-1998.LEV2	RAD13$09-DEC-1998.PKT
			RAD13$10-DEC-1998.LEV1	RAD13$10-DEC-1998.LEV2	RAD13$10-DEC-1998.PKT
RAD14	Calibration with increased shroud tempera	BOL	RAD14$11-DEC-1998.LEV1	RAD14$11-DEC-1998.LEV2	RAD14$11-DEC-1998.PKT
			RAD14$12-DEC-1998.LEV1	RAD14$12-DEC-1998.LEV2	RAD14$12-DEC-1998.PKT
RAD15	Low Radiance Calibration	BOL	RAD15$13-DEC-1998.LEV1	RAD15$13-DEC-1998.LEV2	RAD15$13-DEC-1998.PKT
			RAD15$14-DEC-1998.LEV1	RAD15$14-DEC-1998.LEV2	RAD15$14-DEC-1998.PKT
RAD16	Repeat calibration at centre of along-trac	BOL	RAD16$14-DEC-1998.LEV1	RAD16$14-DEC-1998.LEV2	RAD16$14-DEC-1998.PKT
			RAD16$15-DEC-1998.LEV1	RAD16$15-DEC-1998.LEV2	RAD16$15-DEC-1998.PKT
RAD17	SMU running in backup mode	BOL	RAD17$15-DEC-1998.LEV1		RAD17$15-DEC-1998.PKT
ORB	Orbital Simulations		ORB01$19-DEC-1998.LEV1	ORB01$19-DEC-1998.LEV2	ORB01$19-DEC-1998.PKT